



國立台灣大學理學院物理學研究所  
碩士論文

Department of Physics  
College of Science  
National Taiwan University  
Master Thesis

B 介子衰變至  $\eta K^+ \pi^-$  之 Dalitz 分析  
Dalitz Analysis of Three-body Charmless Hadronic  
decay  $B^0 \rightarrow \eta K^+ \pi^-$

盧沛成  
Pei-Cheng Lu

指導教授: 王名儒 博士  
Advisor: Min-Zu Wang, Ph.D

中華民國 103 年 6 月  
June 2014





## 摘要

我們使用了日本筑波 KEK 之  $B$  工廠於 1998 至 2010 年間收集之 771.581 百萬  $B\bar{B}$  介子對實驗數據。我們量測了  $B^0$  衰變至  $\eta K^+\pi^-$  三體末態的  $CP$  對稱破壞以及各中間態之衰變分支比，藉由 Dalitz 分析，能夠更清楚完整地瞭解此衰變的結構。此量測不考慮魅夸克中間態，只聚焦於底夸克至奇夸克的轉換，亦即稀有衰變的部分。至於  $\eta$  的衰變末態，我們只考慮了  $\eta \rightarrow \gamma\gamma$  和  $\eta \rightarrow \pi^+\pi^-\pi^0$ 。

考慮所有中間態，在  $\eta \rightarrow \gamma\gamma$  此分支中，我們量測到的  $CP$  對稱破壞為  $-0.049^{+0.053}_{-0.052} \pm 0.046$ ，在  $\eta \rightarrow \pi^+\pi^-\pi^0$  分支則為  $0.220^{+0.088}_{-0.084} \pm 0.040$ ，第一個誤差為統計誤差，第二個則是系統誤差。各中間態的衰變分支比量測結果可在 Table.8.3 見到。





# Abstract

We are going to determine the CP asymmetries and to measure branching fractions by Dalitz analysis for the three-body charmless hadronic  $B$  decay:  $B^0 \rightarrow \eta K^+ \pi^-$ ; the branches  $\eta \rightarrow \gamma\gamma$  and  $\eta \rightarrow \pi^+ \pi^- \pi^0$  are considered. This work is based on a data sample of 771.581 million  $B\bar{B}$  pairs collected at the  $\Upsilon(4S)$  resonance with the Belle detector at the KEKB asymmetric energy electron-positron collider.

The measured branching fraction for all intermediate states are reported (see Table.8.3), we also measured  $\mathcal{A}_{CP}$  of inclusive charmless decay ( $B^0 \rightarrow \eta_{\gamma\gamma} K^+ \pi^-$ )  $= -0.049_{-0.052}^{+0.053} \pm 0.046$  and that of ( $B^0 \rightarrow \eta_{\pi^+ \pi^- \pi^0} K^+ \pi^-$ )  $= 0.220_{-0.084}^{+0.088} \pm 0.040$ , the first error is statistical error and the second one is systematic error.





# Contents

<b>1</b>	<b>Introduction</b>	<b>1</b>
1.1	Motivation . . . . .	1
1.2	Standard Model . . . . .	2
1.2.1	Mesons . . . . .	4
1.2.2	Exotic Mesons . . . . .	5
1.2.3	$B$ Physics . . . . .	6
1.2.4	The Cabibbo-Kobayashi-Maskawa Matrix . . . . .	8
1.2.5	$CP$ violation . . . . .	9
1.3	Dalitz plot analysis . . . . .	11
<b>2</b>	<b>Belle Experiment</b>	<b>13</b>
2.1	KEKB B-Factory . . . . .	14
2.2	BELLE Detector . . . . .	15
2.2.1	Beam-line Magnets near the IP and Beam Pipe . . . . .	17
2.2.2	Extreme Forward Calorimeter (EFC) . . . . .	21
2.2.3	Silicon Vertex Detector (SVD) . . . . .	22
2.2.4	Central Drift Chamber (CDC) . . . . .	24
2.2.5	Aerogel Čerenkov Counter System (ACC) . . . . .	25
2.2.6	Time-of-Flight Counters (TOF) . . . . .	28
2.2.7	Electromagnetic Calorimeter (ECL) . . . . .	29
2.2.8	Particle Identification of Electrons and Charged Kaons, EID and KID . . . . .	31
2.2.9	$K_L$ and Muon Detection System (KLM) . . . . .	32
<b>3</b>	<b><math>B</math> Reconstruction and Event Selection</b>	<b>35</b>
3.1	Charged Particle Selection . . . . .	35



3.2	$\eta$ Reconstruction . . . . .	37
3.3	Best Candidate Selection . . . . .	38
3.4	The Modified $M_{bc}$ . . . . .	39
3.5	Selections Summary . . . . .	40
<b>4</b>	<b>Background Study</b>	<b>45</b>
4.1	Overview of Backgrounds Study . . . . .	45
4.2	Continuum Background . . . . .	45
4.2.1	$\Delta Z$ . . . . .	45
4.2.2	$\cos\theta_B$ . . . . .	46
4.2.3	Kakuno Super Fox-Wolfram(KSFW) . . . . .	46
4.2.4	Fisher Discriminant . . . . .	48
4.2.5	Likelihood Ratio(LR) . . . . .	50
4.2.6	Optimization of LR cut . . . . .	50
4.3	Generic $B$ Background . . . . .	52
4.4	Rare $B$ Background . . . . .	52
4.5	Feedacross Background . . . . .	54
<b>5</b>	<b>Control Sample Study</b>	<b>57</b>
5.1	Introduction . . . . .	57
5.2	Fitting . . . . .	61
5.3	Calibration Factor Results . . . . .	61
5.4	$\eta$ Selection Check . . . . .	65
<b>6</b>	<b>Amplitude Analysis on Dalitz Plot</b>	<b>69</b>
6.1	Introduction . . . . .	69
6.2	Three-Body Signal Yields . . . . .	69
6.3	Signal Amplitude Formalism . . . . .	75
6.3.1	LASS Parametrization . . . . .	77
6.4	Efficiency over Dalitz Plot and Smearing . . . . .	78
6.5	Sideband Background Modeling . . . . .	81
6.6	Dalitz Plot Boundary . . . . .	83
6.7	Fitting and Goodness-of-Fit . . . . .	84
6.8	Fit Strategy . . . . .	86



CONTENTS



<b>7</b>	<b>Systematics and Efficiency Correction</b>	<b>87</b>
7.1	Tracking uncertainty . . . . .	87
7.2	PID Identification Uncertainty . . . . .	87
7.3	Number of $B\bar{B}$ pairs uncertainty . . . . .	89
7.4	Signal PDF( $\Delta E, M_{bc}$ ) uncertainty . . . . .	89
7.5	Rare B PDF uncertainty . . . . .	89
7.6	MC efficiency uncertainty . . . . .	90
7.7	$\eta$ efficiency correction and systematics . . . . .	90
7.8	$\pi^0$ efficiency and systematic error . . . . .	90
7.9	$\mathcal{LR}$ cut uncertainty . . . . .	91
7.10	Reconstruction Efficiency . . . . .	91
<b>8</b>	<b>Summary and Conclusion</b>	<b>95</b>
8.1	Fitting Results . . . . .	95
8.2	Floating Background . . . . .	106
8.3	Conclusion . . . . .	106
<b>A</b>	<b>Bias of 2D (<math>\Delta E, M_{bc}</math>) fit</b>	<b>109</b>
<b>B</b>	<b>Bias of Dalitz fitter</b>	<b>111</b>
<b>C</b>	<b>Figures of Dalitz Plot Sideband Modeling</b>	<b>121</b>
<b>D</b>	<b>Dalitz analysis Backup</b>	<b>127</b>
<b>E</b>	<b>Results of Inclusive Decay</b>	<b>133</b>



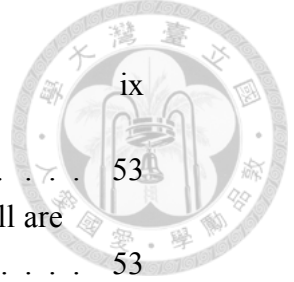


# List of Figures

1.1	Standard model of elementary particles: 12 fundamental fermions and 5 fundamental bosons. [1]. . . . .	3
1.2	Summary of interactions between particles described by the Standard Model. [2]. . . . .	3
1.3	Total $e^+e^-$ cross section measured by CLEO and CUSB showing the masses of $\Upsilon$ resonances. [3]. . . . .	7
1.4	The two leading contributions to the amplitude of $K^0-\bar{K}^0$ oscillation. [4]. . . . .	10
2.1	Bird's eye view of KEKB. . . . .	13
2.2	Schematic layout of KEKB. The Belle detector is located in the interaction point in Tsukuba hall on the northeast side of the KEKB rings. . . . .	15
2.3	Beam rotation by crab cavities. . . . .	17
2.4	Side view of Belle detector [5]. . . . .	19
2.5	The cross-section of the beryllium beam pipe at interaction point [5].	20
2.6	The arrangement of the beam pipe and horizontal masks [5]. . . . .	20
2.7	An isometric view of the BGO crystals of the forward and backward EFC detectors [5]. . . . .	22
2.8	Detector configuration of SVD1 [5]. . . . .	23
2.9	End view comparison of SVD1 and SVD2 [6]. . . . .	24
2.10	Overview of the CDC structure. The lengths in the figure are in units of mm [5]. . . . .	25
2.11	Truncated mean of $dE/dx$ versus momentum observed in collision data. The expected results for $K$ , $\pi$ , proton and $e$ are shown by solid red curves. Unit of the momentum is GeV/c. . . . .	26

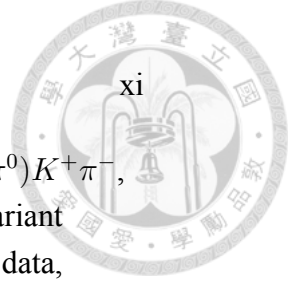
2.12	Cell structure and the cathode sector configuration of CDC [5]. . . . .	26
2.13	The arrangement of ACC at the central part of the Belle detector. [5]. . . . .	27
2.14	Schematic drawing of a typical ACC counter module: (a) barrel and (b) end-cap ACC. [5]. . . . .	28
2.15	Dimensions of a TOF/TSC module. [5]. . . . .	29
2.16	Mass distribution from TOF measurements for particle momenta below 1.2 GeV/c. [5]. . . . .	30
2.17	Overall configuration of ECL. [5]. . . . .	31
2.18	Schematic diagram of the internal spacer arrangement in the KLM detector. [5]. . . . .	34
3.1	Invariant $\eta$ mass distribution in data sample. . . . .	37
3.2	Invariant $\eta$ mass distribution after all selections of $\eta \rightarrow \gamma\gamma$ with three-body phase space decay in signal MC. . . . .	38
3.3	Invariant $\eta$ mass distribution after all selections of $\eta \rightarrow \pi^+ \pi^- \pi^0$ with three-body phase space decay in signal MC. . . . .	38
3.4	Invariant $\pi^0$ mass distribution (a) in data sample (b) in signal MC without true event selection (c) in signal MC with true event se- lection. . . . .	39
3.5	$\Delta E$ and $M_{bc}$ scatter plot in $B \rightarrow K\pi\eta, \eta \rightarrow \gamma\gamma$ . . . . .	40
3.6	$\Delta E$ and $M_{bc}$ scatter plot in $B \rightarrow K\pi\eta, \eta \rightarrow \pi^+\pi^-\pi^0$ . . . . .	41
3.7	Modified $M_{bc}$ and typical $M_{bc}$ , the red line is modified $M_{bc}$ and blue one is typical $M_{bc}$ . Modified $M_{bc}$ has better resolution. . . . .	41
4.1	The distribution of $MM^2$ and Fisher discriminant in each $MM^2$ region. The red line stands for signal MC and the blue line stands for $q\bar{q}$ MC. . . . .	48
4.2	$\Delta Z$ distribution for each mode. The red line stands for signal MC, and the blue line stands for $q\bar{q}$ MC. . . . .	49
4.3	$\cos\theta_B$ distribution for each mode. The red line stands for signal MC, and the blue line stands for $q\bar{q}$ MC. . . . .	49
4.4	$LR$ distribution for each mode. The red line stands for signal MC, and the blue line stands for $q\bar{q}$ MC. . . . .	50
4.5	$q \times q_B \times r$ distribution for $B \rightarrow \eta K\pi$ mode. The red line stands for signal MC, and the blue line stands for $q\bar{q}$ MC. . . . .	51

LIST OF FIGURES



4.6	The 2D histogram lego plot of generic B background in MC. . . . .	53
4.7	The 2D histogram lego plot of rare B background in MC. All are 50 times data. . . . .	53
4.8	The $\Delta E$ projection plot of feedacross from $\eta\pi^+\pi^-$ in MC for $\eta K^+\pi^-$ study. . . . .	55
5.1	The $\Delta E$ (top) and $M_{bc}$ (bottom) projection plot in signal MC with true event selection of $B^0 \rightarrow K\pi\pi^0$ mode. . . . .	62
5.2	The $\Delta E$ (left) and $M_{bc}$ (right) projection plot of data fitting of $B^0 \rightarrow K\pi\pi^0$ mode. . . . .	63
5.3	The $\Delta E$ and $M_{bc}$ projection plot in signal MC with true event selection of $B^0 \rightarrow D^-(K_{S(\pi^+\pi^-)}\pi)\rho^+$ mode. . . . .	63
5.4	The $\Delta E$ and $M_{bc}$ projection plot of data fitting of $B^0 \rightarrow D^-(K_{S(\pi^+\pi^-)}\pi)\rho^+$ mode. . . . .	64
5.5	The $\Delta E$ and $M_{bc}$ projection plot in signal MC with true event selection of $B^+ \rightarrow \eta(\gamma\gamma)\pi^+$ mode. . . . .	65
5.6	The $\Delta E$ and $M_{bc}$ projection plot of data fitting of $B^+ \rightarrow \eta(\gamma\gamma)\pi^+$ mode. . . . .	66
5.7	The $\Delta E$ and $M_{bc}$ projection plot in signal MC with true event selection of $B^+ \rightarrow \eta(\pi^+\pi^-\pi^0)\pi^+$ mode. . . . .	66
5.8	The $\Delta E$ and $M_{bc}$ projection plot of data fitting of $B^+ \rightarrow \eta(\pi^+\pi^-\pi^0)\pi^+$ mode. . . . .	67
6.1	Signal box(rectangular region) and sideband(enclosing region) on $\Delta E - M_{bc}$ scatter plot in data sample for each decay mode. . . . .	71
6.2	Signal shape of $\Delta E$ (left) and $M_{bc}$ (right) in signal MC for $\eta(\gamma\gamma)K\pi$ . . . . .	72
6.3	Signal shape of $\Delta E$ (left) and $M_{bc}$ (right) in signal MC for $\eta(\pi^+\pi^-\pi^0)K\pi$ . . . . .	72
6.4	The $\Delta E$ (left) and $M_{bc}$ (right) projection plot of data fitting for $\eta(\gamma\gamma)K\pi$ . . . . .	73
6.5	The $\Delta E$ (left) and $M_{bc}$ (right) projection plot of data fitting for $\eta(\pi^+\pi^-\pi^0)K\pi$ . . . . .	74
6.6	Reconstruction efficiency distribution over Dalitz plot. . . . .	78
6.7	Dalitz plot in sideband region after all selection requirements in data sample. . . . .	81
8.1	Dalitz plot in signal region after all selection requirements in data sample. . . . .	95

- 8.2 Dalitz analysis result in data  $\Delta E - M_{bc}$  signal box of  $\eta(\gamma\gamma)K^+\pi^-$ , first five plots show invariant mass of  $K^+\pi^-$  in  $M_{\eta\pi^-}$  slices, the bottom right one is the whole plot. Points with error bars are data, histograms are fit result, hatched histograms are background. . . . 97
- 8.3 Dalitz analysis result in data  $\Delta E - M_{bc}$  signal box of  $\eta(\gamma\gamma)K^+\pi^-$ , first five plots show invariant mass of  $\eta\pi^-$  in  $M_{K^+\pi^-}$  slices, the bottom right one is the whole plot. Points with error bars are data, histograms are fit result, hatched histograms are background. . . . 98
- 8.4 Dalitz analysis result in data  $\Delta E - M_{bc}$  signal box of  $\eta(\gamma\gamma)K^+\pi^-$ , first five plots show invariant mass of  $K^+\eta$  in  $M_{K^+\pi^-}$  slices, the bottom right one is the whole plot. Points with error bars are data, histograms are fit result, hatched histograms are background. . . . 99
- 8.5 Dalitz analysis result in data  $\Delta E - M_{bc}$  signal box of  $\eta(\gamma\gamma)K^+\pi^-$ , the left plot is invariant mass of  $K^+\pi^-$ , the right plot is invariant mass of  $\eta\pi^-$  in  $M_{K\pi} < 1.8 \text{ GeV}/c^2$ . Points with error bars are data, histograms are fit result, hatched histograms are background, red line is  $K^*(892)^0$ , blue line is  $K_0^*(1430)^0$  by LASS, green line is  $K_2^*(1430)^0$ . The effect of interference between each component is not shown in these plots. . . . . 100
- 8.6 Dalitz analysis result in data  $\Delta E - M_{bc}$  signal box of  $\eta(\pi^+\pi^-\pi^0)K^+\pi^-$ , first five plots show invariant mass of  $K^+\pi^-$  in  $M_{\eta\pi^-}$  slices, the bottom right one is the whole plot. Points with error bars are data, histograms are fit result, hatched histograms are background. . . . 101
- 8.7 Dalitz analysis result in data  $\Delta E - M_{bc}$  signal box of  $\eta(\pi^+\pi^-\pi^0)K^+\pi^-$ , first five plots show invariant mass of  $\eta\pi^-$  in  $M_{K^+\pi^-}$  slices, the bottom right one is the whole plot. Points with error bars are data, histograms are fit result, hatched histograms are background. . . . 102
- 8.8 Dalitz analysis result in data  $\Delta E - M_{bc}$  signal box of  $\eta(\pi^+\pi^-\pi^0)K^+\pi^-$ , first five plots show invariant mass of  $K^+\eta$  in  $M_{K^+\pi^-}$  slices, the bottom right one is the whole plot. Points with error bars are data, histograms are fit result, hatched histograms are background. . . . 103



LIST OF FIGURES

8.9 Dalitz analysis result in data  $\Delta E - M_{bc}$  signal box of  $\eta(\pi^+\pi^-\pi^0)K^+\pi^-$ , the left plot is invariant mass of  $K^+\pi^-$ , the right plot is invariant mass of  $\eta\pi^-$  in  $M_{K\pi} < 1.8 \text{ GeV}/c^2$ . Points with error bars are data, histograms are fit result, hatched histograms are background, red line is  $K^*(892)^0$ , blue line is  $K_0^*(1430)^0$  by LASS, green line is  $K_2^*(1430)^0$ . The effect of interference between each component is not shown in these plots. . . . . 104

A.1 Bias, error and pull result of ensemble test for  $B^0 \rightarrow \eta(\gamma\gamma)K^+\pi^-$ . 110

A.2 Bias, error and pull result of ensemble test for  $B^0 \rightarrow \eta(\pi^+\pi^-\pi^0)K^+\pi^-$ . 110

B.1 Bias, error and pull result of ensemble test for the parameter  $A_{K_0^*}$ . 114

B.2 Bias, error and pull result of ensemble test for the parameter  $\phi_{K_0^*}$ . 114

B.3 Bias, error and pull result of ensemble test for the parameter  $A_{K_2^*}$ . 115

B.4 Bias, error and pull result of ensemble test for the parameter  $\phi_{K_2^*}$ . 115

B.5 Bias, error and pull result of ensemble test for the parameter  $A_{a_0}$ . . 116

B.6 Bias, error and pull result of ensemble test for the parameter  $\phi_{a_0}$ . . 116

B.7 Bias, error and pull result of ensemble test for the parameter  $\Gamma_{a_0}$ . . 117

B.8 Bias, error and pull result of ensemble test for the parameter  $A_{a_2}$ . . 117

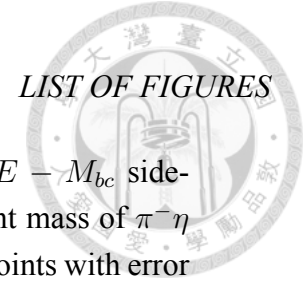
B.9 Bias, error and pull result of ensemble test for the parameter  $\phi_{a_2}$ . . 118

B.10 Bias, error and pull result of ensemble test for the parameter  $A_{nr}$ . . 118

B.11 Bias, error and pull result of ensemble test for the parameter  $\phi_{nr}$ . . 119

C.1 Result of unbinned maximum likelihood fit of parametrization in data  $\Delta E - M_{bc}$  sideband, the left two plots show the invariant mass of  $K^+\pi^-$ , the right two show the invariant mass of  $\pi^-\eta$ . Points with error bars are data, histograms are fit result. . . . . 122

C.2 Result of combined modeling method in data  $\Delta E - M_{bc}$  sideband of  $\eta(\gamma\gamma)K^+\pi^-$ , top four plots show invariant mass of  $K^+\pi^-$  in  $M_{\pi^-\eta}$  regions, the last one is the whole plot. Points with error bars are data, histograms are fit result. Right plots are close view in uniform resonance region. . . . . 123



- C.3 Result of combined modeling method in data  $\Delta E - M_{bc}$  sideband of  $\eta(\gamma\gamma)K^+\pi^-$ , top four plots show invariant mass of  $\pi^-\eta$  in  $M_{K^+\pi^-}$  regions, the last one is the whole plot. Points with error bars are data, histograms are fit result. Right plots are close view in uniform resonance region. . . . . 124
- C.4 Result of combined modeling method in data  $\Delta E - M_{bc}$  sideband of  $\eta(\pi^+\pi^-\pi^0)K^+\pi^-$ , top four plots show invariant mass of  $K^+\pi^-$  in  $M_{\pi^-\eta}$  regions, the last one is the whole plot. Points with error bars are data, histograms are fit result. Right plots are close view in uniform resonance region. . . . . 125
- C.5 Result of combined modeling method in data  $\Delta E - M_{bc}$  sideband of  $\eta(\pi^+\pi^-\pi^0)K^+\pi^-$ , top four plots show invariant mass of  $\pi^-\eta$  in  $M_{K^+\pi^-}$  regions, the last one is the whole plot. Points with error bars are data, histograms are fit result. Right plots are close view in uniform resonance region. . . . . 126
- D.1 Close look of Dalitz analysis result in data  $\Delta E - M_{bc}$  signal box of  $\eta(\gamma\gamma)K^+\pi^-$ , first five plots show invariant mass of  $K^+\pi^-$  in  $M_{\eta\pi^-}$  slices, the bottom right one is the whole plot. Points with error bars are data, histograms are fit result, hatched histograms are background. . . . . 128
- D.2 Close look of Dalitz analysis result in data  $\Delta E - M_{bc}$  signal box of  $\eta(\gamma\gamma)K^+\pi^-$ , first five plots show invariant mass of  $\eta\pi^-$  in  $M_{K^+\pi^-}$  slices, the bottom right one is the whole plot. Points with error bars are data, histograms are fit result, hatched histograms are background. . . . . 129
- D.3 Close look of Dalitz analysis result in data  $\Delta E - M_{bc}$  signal box of  $\eta(\pi^+\pi^-\pi^0)K^+\pi^-$ , first five plots show invariant mass of  $K^+\pi^-$  in  $M_{\eta\pi^-}$  slices, the bottom right one is the whole plot. Points with error bars are data, histograms are fit result, hatched histograms are background. . . . . 130





*LIST OF FIGURES*

D.4 Close look of Dalitz analysis result in data  $\Delta E - M_{bc}$  signal box of  $\eta(\pi^+\pi^-\pi^0)K^+\pi^-$ , first five plots show invariant mass of  $\eta\pi^-$  in  $M_{K^+\pi^-}$  slices, the bottom right one is the whole plot. Points with error bars are data, histograms are fit result, hatched histograms are background. . . . . 131

E.1 The  $\Delta E$ (left) and  $M_{bc}$ (right) projection plot of data fitting for  $\eta(\gamma\gamma)K^+\pi^-$  and  $\eta(\gamma\gamma)K^-\pi^+$ , every component is the same as Fig.?? . . . . . 133

E.2 The  $\Delta E$ (left) and  $M_{bc}$ (right) projection plot of data fitting for  $\eta(\pi^+\pi^-\pi^0)K^+\pi^-$  and  $\eta(\pi^+\pi^-\pi^0)K^-\pi^+$ , every component is the same as Fig.?? . . . 134





# List of Tables

1.1	Quantum numbers for the three generations of the quarks. . . . .	2
1.2	Suggested $q\bar{q}$ quark-model assignments for some of the observed light mesons. The wave functions $f$ and $f'$ are given in the text. . . . .	5
1.3	Properties of $B$ mesons [7]. . . . .	7
2.1	Parameters of KEKB accelerator [8]. . . . .	16
2.2	Performance parameters for the Belle detector. There were two configuration of inner detectors used to collect two data sets. DS-I and DS-II, corresponding to a 3-layer SVD1 and a 4-layer SVD2 with a smaller beam pipe, respectively. [5] . . . . .	18
2.3	Geometrical parameters of ECL. [5]. . . . .	31
3.1	The branching ratio in $B \rightarrow \eta K^*(892)^0$ is $15.9 \pm 1.0$ in PDG. . . . .	36
3.2	The branching ratio in $B \rightarrow \eta K_0^*(1430)^0$ is $11.0 \pm 2.2$ in PDG. . . . .	36
3.3	The branching ratio in $B \rightarrow \eta K_2^*(1430)^0$ is $9.6 \pm 2.1$ in PDG. . . . .	36
3.4	The branching ratio in $\eta$ decay in PDG. . . . .	36
3.5	Width values of modified $M_{bc}$ and typical $M_{bc}$ (MeV/ $c^2$ ), and correlation coefficients ( $\times 10^{-2}$ ) between $\Delta E$ and $M_{bc}$ shown in the bottom of the table. . . . .	42
3.6	Summary of particle selection criteria. . . . .	43
4.1	The $MM^2$ regions of KSFW . . . . .	47
4.2	The fisher distance for each $MM^2$ region. . . . .	48
4.3	$\mathcal{LR}$ cut in each $(q \times q_B \times r)$ bin. . . . .	52
5.1	Summary of $B^0 \rightarrow K^+ \pi^- \pi^0$ selection criteria. . . . .	58
5.2	Summary of $B^0 \rightarrow D^-(K_{S(\pi^+\pi^-)}\pi) \rho^+$ selection criteria. . . . .	59

5.3	Summary of $B^+ \rightarrow \eta\pi^+$ selection criteria. . . . .	60
5.4	Fudge factors result of $B^0 \rightarrow K\pi\pi^0$ between data and MC. . . . .	62
5.5	Mean value difference of $B^0 \rightarrow K\pi\pi^0$ between data and MC. . . . .	64
5.6	Fudge factors result of $D^-(K_{S(\pi^+\pi^-)}\pi)\rho^+$ between data and MC. . . . .	64
5.7	Mean value difference of $D^-(K_{S(\pi^+\pi^-)}\pi)\rho^+$ between data and MC. . . . .	64
5.8	Summary table of branching fractions and other details for each mode. . . . .	65
6.1	Signal box region for each decay mode. . . . .	70
6.2	Number of events of pure three-body signal final state and corresponding efficiency for different decay modes in signal MC. All selection requirements are applied. . . . .	70
6.3	Number of events and ratio between self-cross-feed and signal in signal MC after applying all selection requirements in entire $\Delta E - M_{bc}$ signal yield fitting region. The ratio values are fixed in $\Delta E - M_{bc}$ signal yield fitting. . . . .	71
6.4	Blatt-Weisskopf barrier factors. $q_0$ is the momentum of either daughter particle in the resonance frame. $q$ is the momentum of either daughter particle in the resonance candidate frame. $d$ is impact parameter (resonance radius). Form factors are normalized to give $F_r = 1$ for $q^2 d^2 = q_0^2 d^2$ when $m_{ab} = m_r$ . . . . .	77
6.5	$\chi^2$ comparison of parametrization and combined method modeling. $(\chi^2)_1$ is defined as Eq.(??), $(\chi^2)_2$ is defined as Eq.(??). . . . .	83
7.1	The KID efficiency (%) and fake rate for $\eta(\gamma\gamma)K^\pm\pi^\mp$ . Ratio = (Data/MC). . . . .	88
7.2	The KID efficiency (%) and fake rate for $\eta(\pi^+\pi^-\pi^0)K^\pm\pi^\mp$ . Ratio = (Data/MC). . . . .	88
7.3	Parameters and the corresponding systematic error in signal PDF systematics study (%). . . . .	89
7.4	The $\eta$ selection efficiency(%) for data and MC. Ratio = (Data/MC). . . . .	90
7.5	The $\mathcal{LR}$ cut efficiency(%) for data and MC. Ratio = (Data/MC). . . . .	91
7.6	Signal efficiencies and efficiency corrections for each mode. . . . .	93
7.7	Systematic error for branching fraction (unit in %). . . . .	94



LIST OF TABLES

8.1 Results of Dalitz analysis in  $B^0 \rightarrow \eta K^+ \pi^-$  in signal box without considering  $CP$  violation. . . . . 105

8.2 Comparison between  $\Delta E - M_{bc}$  fit and Dalitz analysis in LMR and HMR. . . . . 106

8.3 Branching fraction and significance for each mode, the first error term is statistical error and the second term is systematic error. . . . 108

A.1 The input number and fitting value of ensemble test. . . . . 109

B.1 Number of events in each sample while ensemble test. . . . . 111

B.2 Given values and fit values for each parameter in ensemble test. . . 112

B.3 Bias, error and pull for each parameter in ensemble test. . . . . 113

D.1 Fixed parameters of Dalitz analysis in  $B^0 \rightarrow \eta K^+ \pi^-$ . . . . . 127

E.1 Signal yields( $N_s$ ), reconstruction efficiencies( $\epsilon_{recon}$ ), branching fraction( $\mathcal{B}$ ) from 2D Maximum likelihood unbinned  $\Delta E - M_{bc}$  fits for inclusive decays. . . . . 133



# Chapter 1

## Introduction

### 1.1 Motivation

Measurements of charmless hadronic  $B$  decays play an important role in understanding  $CP$  violation in  $B$  meson system. Observation of large branching fractions  $B$  mesons decaying to three-body charmless hadronic system have been reported by Belle and BaBar [9] [10] [11]. Charmless  $B$  decays with  $b \rightarrow s$  transition are expected to be dominated by penguin diagrams. The branching fraction for  $B \rightarrow \eta K^*$  is expected to be larger than most similar decays. Previous studies have confirmed that [10] [11]. The previous  $B \rightarrow \eta K^*$  studies were based on the data sample contains  $449 \times 10^6 B\bar{B}$  pairs collected by Belle and  $344 \times 10^6$  collected by BaBar.

This analysis of charmless hadronic  $B^0$  decaying to three light mesons:  $\eta$ ,  $K^+$  and  $\pi^-$ , is based on a higher integrated luminosity data sample of  $772 \times 10^6 B\bar{B}$  pairs collected by Belle detector. It can provide an improved measurement compared to the previous studies. With such data sample, we would also get an improved understanding of the structures of intermediate states (including  $(K\pi)_0^{*0}$  s-wave and non-resonant amplitude) on Dalitz plot.

Besides, there may exist an interesting intermediate state:  $a_0^-(980)K^+$  where  $a_0^-(980)$  is perceived primarily as a four-quark bound state. In practice, it's hard to make a theoretical prediction based on four-quark picture, thus prediction is made in 2-quark model. We can compare the result of measurement with theoretical prediction. It's an opportunity to understand the nature of  $a_0^-(980)$ .



## 1.2 Standard Model

Particle physicists study the fundamental constituents of matter and their interactions. The standard model (SM) of particle physics is a theory concerning the properties and interactions of three distinct types of particles: two spin- $\frac{1}{2}$  families of fermions called quarks (down:  $d$ , up:  $u$ , strange:  $s$ , charm:  $c$ , bottom:  $b$ , top:  $t$ ) and leptons (electron:  $e$ , muon:  $\mu$ , tau:  $\tau$  and the corresponding neutrinos:  $\nu_e, \nu_\mu, \nu_\tau$ ); one family of spin-1 bosons called gauge bosons (photon, gluon,  $W^\pm, Z^0$ ), and spin-0 particle called Higgs boson. Three types interaction between matters are concerned: electromagnetic, weak, and strong interactions [12] [13].

Quarks and leptons can be classified into three generations; each quark carries a fractional electric charge while each lepton carries integer electric charge. Table. 1.1 shows quantum numbers for each quark. Fig. 1.1 shows quarks, leptons, bosons and their corresponding properties.

Table 1.1: Quantum numbers for the three generations of the quarks.

Quantum Number	$d$	$u$	$s$	$c$	$b$	$t$
Isospin: I	$\frac{1}{2}$	$\frac{1}{2}$	0	0	0	0
Isospin $z$ component: $I_z$	$-\frac{1}{2}$	$+\frac{1}{2}$	0	0	0	0
Strangeness: S	0	0	-1	0	0	0
Charm: C	0	0	0	+1	0	0
Bottomness: B	0	0	0	0	-1	0
Topness: T	0	0	0	0	0	+1

Quarks cannot be directly observed, and always clump together to form a group, called hadron. Quarks cannot be isolated from their parent hadron; this phenomenon is called color confinement. Hadrons include both mesons( $q\bar{q}$ ) and baryons ( $qqq$ ).

Gauge bosons carry fundamental interactions: photons carry the electromagnetic interaction; gluons carry the strong interaction,  $W^\pm$  and  $Z^0$  carry the weak interaction. Fig.1.2 shows the interactions between elementary particles described in standard model.

Higgs boson is in charge of the Higgs mechanism which explains the process that gives masses to elementary particles. A Higgs-like boson with mass  $\sim$

1.2. STANDARD MODEL

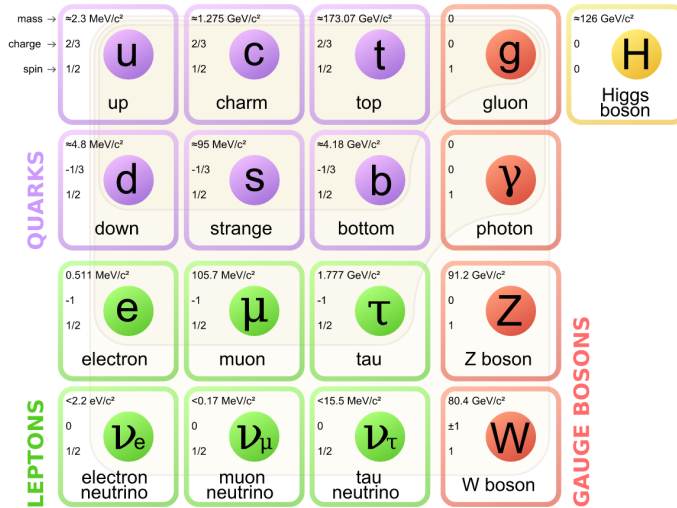


Figure 1.1: Standard model of elementary particles: 12 fundamental fermions and 5 fundamental bosons. [1].

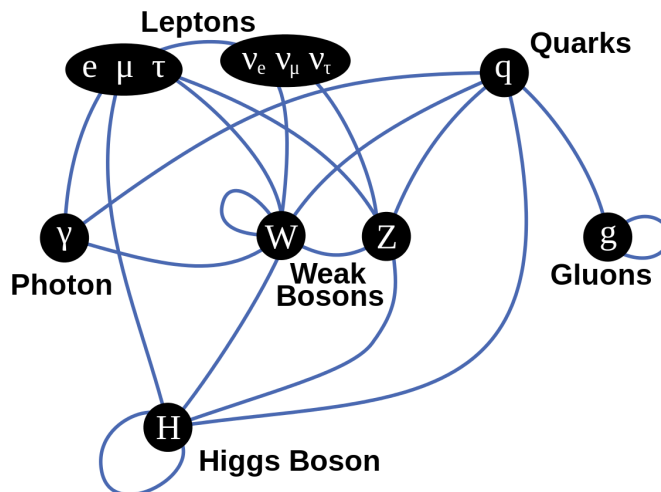


Figure 1.2: Summary of interactions between particles described by the Standard Model. [2].



126GeV/c<sup>2</sup> is first discovered by two groups at LHC in CERN: ATLAS and CMS. By March 2013, this particle had been proven to behave, interact and decay in the expected ways predicted by the standard model. On the 8th of October 2013, it was announced that Peter Higgs and Francois Englert would share the 2013 Nobel Prize in Physics for the theoretical establishment of the Higgs mechanism [14].

### 1.2.1 Mesons

The properties of mesons are important for the study of QCD. Mesons have baryon number  $\beta = 0$ . In the quark model mesons are  $q\bar{q}'$  bound states. The flavors of  $q$  and  $q'$  may be different. The parity  $P$  of meson is  $(-1)^{l+1}$ , where  $l$  is the orbital angular momentum of  $q\bar{q}'$  state. The meson spin  $J$  is given by the relation  $|l - s| < J < |l + s|$ , where  $s$  is 0 (antiparallel quark spins) or 1 (parallel quark spins). The charge conjugation, or  $C$ -parity  $C = (-1)^{l+s}$ , is defined only for the  $q\bar{q}$  states made of quarks and their own antiquarks. The  $C$ -parity can be generalized to the  $G$ -parity  $G = (-1)^{J+l+s}$  for mesons made of quarks and their own antiquarks (isospin  $I_z = 0$ ), and for the charged  $u\bar{d}$  and  $d\bar{u}$  states (isospin  $I = 1$ ).

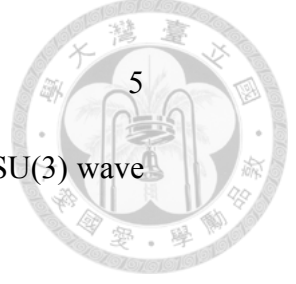
The mesons are classified in  $J^{PC}$  multiplets. The  $l = 0$  states are the pseudoscalars ( $0^{-+}$ ) and the vectors ( $1^{--}$ ). The orbital excitations  $l = 1$  are the scalars ( $0^{++}$ ), the axial vectors ( $1^{++}$ ) and ( $1^{+-}$ ), and the tensors ( $2^{++}$ ). Assignments for many of the known mesons are given in Table.1.2.

States in the natural spin-parity series  $P = (-1)^J$  must, according to the above, have  $s = 1$  and hence,  $CP = +1$ . Thus, mesons with natural spin-parity and  $CP = -1$  ( $0^{+-}$ ,  $1^{-+}$ ,  $2^{+-}$ ,  $3^{-+}$ , etc.) are forbidden in the  $q\bar{q}'$  model. The  $J^{PC} = 0^{--}$  state is forbidden as well. Mesons with such exotic quantum numbers may exist, but would lie outside the  $q\bar{q}$  model (see section below on exotic mesons).

Following SU(3), the nine possible  $q\bar{q}'$  combinations containing the light  $u$ ,  $d$ , and  $s$  quarks are grouped into an octet and a singlet of light quark mesons:

$$3 \otimes \bar{3} = 8 \oplus 1 \quad (1.1)$$

Isoscalar states with the same  $J^{PC}$  will mix, but mixing between the two light quark isoscalar mesons, and the much heavier charmonium or bottomonium states, are generally assumed to be negligible. In the following, we shall use the generic names  $a$  for the  $I = 1$ ,  $K$  for the  $I = 1/2$ , and  $f$  and  $f'$  for the  $I = 0$  members of the



## 1.2. STANDARD MODEL

light quark nonets. Thus, the physical isoscalars are mixtures of the SU(3) wave function  $\psi_8$  and  $\psi_1$ :

$$f' = \psi_8 \cos \theta - \psi_1 \sin \theta \quad (1.2)$$

$$f = \psi_8 \sin \theta + \psi_1 \cos \theta \quad (1.3)$$

where  $\theta$  is the nonet mixing angle and

$$\psi_8 = \frac{1}{\sqrt{6}}(u\bar{u} + d\bar{d} - 2s\bar{s}) \quad (1.4)$$

$$\psi_1 = \frac{1}{\sqrt{3}}(u\bar{u} + d\bar{d} + s\bar{s}) \quad (1.5)$$

The mixing angle has to be determined experimentally.

Table 1.2: Suggested  $q\bar{q}$  quark-model assignments for some of the observed light mesons. The wave functions  $f$  and  $f'$  are given in the text.

$n^{2s+1}l_J$	$J^{PC}$	I = 1	I = $\frac{1}{2}$	I = 0	I = 0
		$u\bar{d}, \bar{u}d, \frac{1}{\sqrt{2}}(d\bar{d}-u\bar{u})$	$u\bar{s}, d\bar{s}, \bar{d}s, -\bar{u}s$	$f'$	$f$
$1^1S_0$	$0^{-+}$	$\pi$	$K$	$\eta$	$\eta'(958)$
$1^3S_1$	$1^{--}$	$\rho(770)$	$K^*(892)$	$\phi(1020)$	$\omega(782)$
$1^1P_1$	$1^{+-}$	$b_1(1235)$	$K_{1B}^\dagger$	$h_1(1380)$	$h_1(1170)$
$1^3P_0$	$0^{++}$	$a_0(1450)$	$K^*_0(1430)$	$f_0(1710)$	$f_0(1370)$
$1^3P_1$	$1^{++}$	$a_1(1260)$	$K_{1A}^\dagger$	$f_1(1420)$	$f_1(1285)$
$1^3P_2$	$2^{++}$	$a_2(1320)$	$K^*_2(1430)$	$f'_2(1525)$	$f_2(1270)$

The light scalars  $a_0(980)$ ,  $f_0(980)$  and  $f_0(600)$  are often considered as meson-meson resonances or four quark states and are therefore not included in this table.

<sup>†</sup>  $K_{1A}$  and  $K_{1B}$  are nearly equal ( $45^\circ$ ) mixtures of the  $K_1(1270)$  and  $K_1(1400)$ .

### 1.2.2 Exotic Mesons

The existence of a light nonet composed of four quarks with masses below 1 GeV was suggested a long time ago [15]. Coupling two triplets of light quarks

$u$ ,  $d$ , and  $s$ , one obtains nine states, of which the six symmetric ( $uu$ ,  $dd$ ,  $ss$ ,  $ud + du$ ,  $us + su$ ,  $ds + sd$ ) form the six dimensional representation 6, while the three antisymmetric ( $ud - du$ ,  $us - su$ ,  $ds - sd$ ) form the three dimensional representation  $\bar{3}$  of SU(3):

$$3 \otimes \bar{3} = 6 \oplus 3 \quad (1.6)$$

Combining with spin and color and requiring antisymmetry, one finds that the most deeply bound diquark (and hence the lightest) is the one in the  $\bar{3}$  and spin singlet state. The combination of the diquark with an antiquark in the 3 representation then gives a light nonet of four-quark scalar states. Letting the number of strange quarks determine the mass splitting, one obtains a mass inverted spectrum with a light isosinglet ( $ud\bar{u}d$ ), a medium heavy isodoublet (e.g.,  $ud\bar{s}d$ ) and a heavy isotriplet (e.g.,  $ds\bar{u}s$ ) + isosinglet (e.g.,  $us\bar{u}s$ ). It is then tempting to identify the lightest state with the  $f_0(600)$ , and the heaviest states with the  $a_0(980)$ , and  $f_0(980)$ . Then the meson with strangeness  $\kappa(800)$  would lie in between.

### 1.2.3 $B$ Physics

In 1977, CFS E288 headed by Leon Lederman at Fermilab discovered a dimuon resonance at 9.5 GeV [16], which now recognized as  $\Upsilon(1S)$ .  $\Upsilon$  is a flavorless meson formed by a  $b$  quark and an anti- $b$  quark. Fig.1.3 shows the cross section of particle production as a function of energy measured by CUSB and CLEO detector in CESR at Cornell University [17]. Various  $\Upsilon$  states can be seen on it.

$B$  mesons are the particles composed of an anti- $b$  quark and either a  $u$  quark or a  $d$  quark, which are charged  $B$  meson ( $B^+$ ) or neutral  $B$  meson ( $B^0$ ), respectively. To expand this, an anti- $b$  quark and either a  $s$  quark or a  $c$  quark form strange  $B$  meson ( $B_s^0$ ) or charmed  $B$  meson ( $B_c^+$ ). Table.1.3 shows  $B$  mesons and their properties.

To study the physics related to the  $B$  mesons, physicists use the  $\Upsilon(4S)$  resonance to produce  $B$  mesons in a large quantity.  $\Upsilon(4S)$  has mass  $(10.5794 \pm 0.0012)$  GeV, which is only 20 MeV above  $B\bar{B}$  threshold, and the branching fraction of  $\Upsilon(4S)$  decays to  $B\bar{B}$  pairs is larger than 96%. Experimentally, we produce  $B$  mesons by the  $e^+e^-$  collisions at a center-of-mass energy on  $\Upsilon(4S)$  resonance and  $\Upsilon(4S)$  almost immediately decays to  $B\bar{B}$  pairs (including  $B^+B^-$  and  $B^+\bar{B}^0$ ).

## 1.2. STANDARD MODEL



Most of the hadronic  $B$  decays involve  $b \rightarrow c$  transition at the quark level, resulting in a charmed hadron or charmonium in the final state. For  $B$ -meson decays do not occur through the  $b \rightarrow c$  transition are usually called rare  $B$  decays, which include both semileptonic and hadronic  $b \rightarrow u$  decays that are suppressed at leading order by the small CKM matrix element  $V_{ub}$ , as well as higher-order  $b \rightarrow s(d)$  processes such as electroweak and gluonic penguin decays.

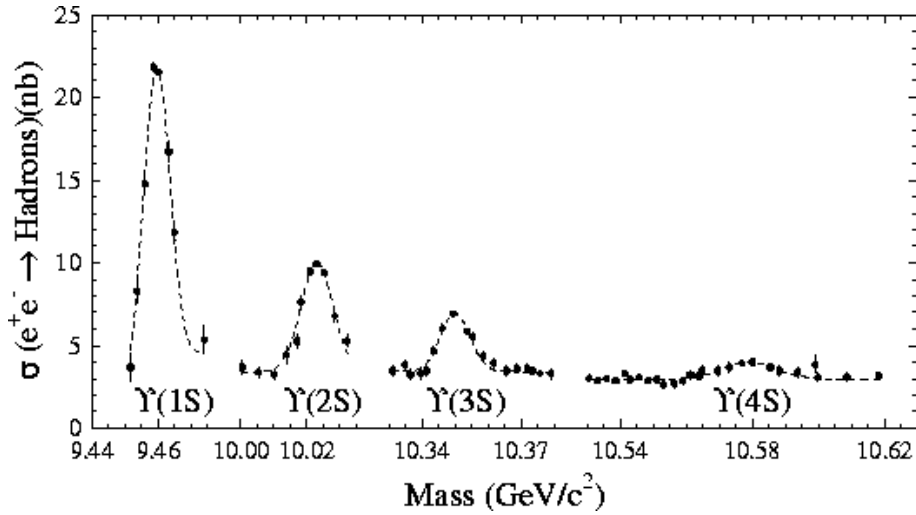


Figure 1.3: Total  $e^+e^-$  cross section measured by CLEO and CUSB showing the masses of  $\Upsilon$  resonances. [3].

Table 1.3: Properties of  $B$  mesons [7].

Type	Quark content	$I(J^P)$	Rest mass ( $\text{MeV}/c^2$ )	Mean lifetime (ps)
$B^+$	$u\bar{d}$	$\frac{1}{2}(0^-)$	$5279.17 \pm 0.29$	$1.641 \pm 0.008$
$B^0$	$d\bar{d}$	$\frac{1}{2}(0^-)$	$5279.50 \pm 0.30$	$1.519 \pm 0.007$
$B_s^0$	$s\bar{d}$	$0(0^-)$	$5366.3 \pm 0.6$	$1.425 \pm 0.041$
$B_c^+$	$c\bar{d}$	$0(0^-)$	$6277 \pm 6$	$0.453 \pm 0.041$



### 1.2.4 The Cabibbo-Kobayashi-Maskawa Matrix

In standard model, the quark can change their flavor to another generation in the weak interaction. For example, the  $d$ ,  $s$  and  $b$  quark are not pure mass eigenstates with regard to weak interactions, but are their own mixtures [18]. The quark mixing concept with three quark generations was proposed by Kobayashi and Maskawa in 1973 [19], where three real mixing components plus a phase were assumed. This work was a generalization of the two generation mixing model with a single parameter, the Cabibbo angle [18]. By convention, the mixing is often expressed in terms of a  $3 \times 3$  unitary matrix  $V$  operating on the charge  $-e/3$  quark mass eigenstates ( $d$ ,  $s$  and  $b$ ):

$$\begin{pmatrix} d' \\ s' \\ b' \end{pmatrix} = \begin{pmatrix} V_{ud} & V_{us} & V_{ub} \\ V_{cd} & V_{cs} & V_{cb} \\ V_{td} & V_{ts} & V_{tb} \end{pmatrix} \begin{pmatrix} d \\ s \\ b \end{pmatrix} \quad (1.7)$$

There are several parameterizations of the Cabibbo-Kobayashi-Maskawa (CKM) matrix. Kobayashi and Maskawa [19] originally chose a parameterization involving the four angles:  $\theta_1$ ,  $\theta_2$ ,  $\theta_3$  and  $\delta$ :

$$\begin{pmatrix} d' \\ s' \\ b' \end{pmatrix} = \begin{pmatrix} c_1 & -s_1 c_3 & -s_1 s_3 \\ s_1 c_2 & c_1 c_2 c_3 - s_2 s_3 e^{i\delta} & c_1 c_2 s_3 + s_2 c_3 e^{i\delta} \\ s_1 s_2 & c_1 s_2 c_3 + c_2 s_3 e^{i\delta} & c_1 s_2 s_3 - c_2 c_3 e^{i\delta} \end{pmatrix} \begin{pmatrix} d \\ s \\ b \end{pmatrix} \quad (1.8)$$

where  $c_i = \cos \theta_i$  and  $s_i = \sin \theta_i$  for  $i = 1, 2, 3$ . In the limit  $\theta_2 = \theta_3 = 0$ , this reduces to the usual Cabibbo mixing with  $\theta_1$  identified (up to a sign) with the Cabibbo angle [18]. Note that in this case  $V_{ub}$  and  $V_{td}$  are real and  $V_{cb}$  complex, illustrating a different placement of the phase than in the standard parameterization.

The "standard" parameterization [20] of  $V$  that utilizes angles  $\theta_{12}$ ,  $\theta_{23}$ ,  $\theta_{13}$  and a  $CP$ -violation phase  $\delta$ :

$$V = \begin{pmatrix} c_{12}c_{13} & s_{12}c_{13} & s_{13}e^{-i\delta} \\ -s_{12}c_{23} - c_{12}s_{23}s_{13}e^{i\delta} & c_{12}c_{23} - s_{12}s_{23}s_{13}e^{i\delta} & s_{23}c_{13} \\ s_{12}s_{23} - c_{12}c_{23}s_{13}e^{i\delta} & -c_{12}s_{23} - s_{12}c_{23}s_{13}e^{i\delta} & c_{23}c_{13} \end{pmatrix} \quad (1.9)$$

with  $c_{ij} = \cos \theta_{ij}$  and  $s_{ij} = \sin \theta_{ij}$  for the "generation" labels  $i, j = 1, 2, 3$ .

## 1.2. STANDARD MODEL

An approximation to the standard parameterization proposed by Lincoln Wolfenstein [21] emphasizes the hierarchy in the size of the angles,  $s_{12} \gg s_{23} \gg s_{13}$ . Setting  $\lambda \equiv s_{12} = \sin \theta_c$ , the sine of the Cabibbo angle, one expresses the other elements in terms of powers of  $\lambda$ :

$$V = \begin{pmatrix} 1 - \lambda^2/2 & \lambda & A\lambda^3(\rho - i\eta) \\ -\lambda & 1 - \lambda^2/2 & A\lambda^2 \\ A\lambda^3(1 - \rho - i\eta) & -A\lambda^2 & 1 \end{pmatrix} + O(\lambda^4) \quad (1.10)$$

with  $A$ ,  $\rho$  and  $\eta$  real numbers that were intended to be of order unity. This approximate form is widely used for  $B$  physics.

The experimental determination by using all available measurements of the four real quantities in the Wolfenstein parameterization are:

$$\begin{aligned} \lambda &= 0.22535 \pm 0.00065, \\ A &= 0.811^{+0.022}_{-0.012}, \\ \rho &= 0.131^{+0.026}_{-0.013}, \\ \eta &= 0.345^{+0.013}_{-0.014} \end{aligned} \quad (1.11)$$

therefor the magnitude of  $V_{CKM}$ :

$$V_{CKM} \equiv \begin{pmatrix} |V_{ud}| & |V_{us}| & |V_{ub}| \\ |V_{cd}| & |V_{cs}| & |V_{cb}| \\ |V_{td}| & |V_{ts}| & |V_{tb}| \end{pmatrix} \quad (1.12)$$

with the best determination is:

$$V_{CKM} = \begin{pmatrix} 0.97427 \pm 0.00015 & 0.22534 \pm 0.00065 & 0.00351^{+0.00015}_{-0.00014} \\ 0.22520 \pm 0.00065 & 0.97344 \pm 0.00016 & 0.0412^{+0.0011}_{-0.0005} \\ 0.00867^{+0.00029}_{-0.00031} & 0.0404^{+0.0011}_{-0.0005} & 0.999146^{+0.000021}_{-0.000046} \end{pmatrix} \quad (1.13)$$

### 1.2.5 $CP$ violation

In particle physics,  $CP$  violation ( $CP$  standing for Charge Parity) is a violation of the postulated  $CP$ -symmetry (or Charge conjugation Parity symmetry).

$CP$  violation occurs in the weak interaction and was observed in many decays of mesons.

The discovery of  $CP$  violation in 1964 in the decays of neutral kaons [22] resulted in the Nobel Prize in Physics in 1980 for its discoverers James Cronin and Val Fitch. They observed that neutral kaons can transform into their antiparticles (in which each quark is replaced with the other's antiquark) and vice versa, but such transformation does not occur with exactly the same probability in both directions. The leading contributions to the amplitude of  $K^0-\bar{K}^0$  oscillation are shown in Fig. 1.4.

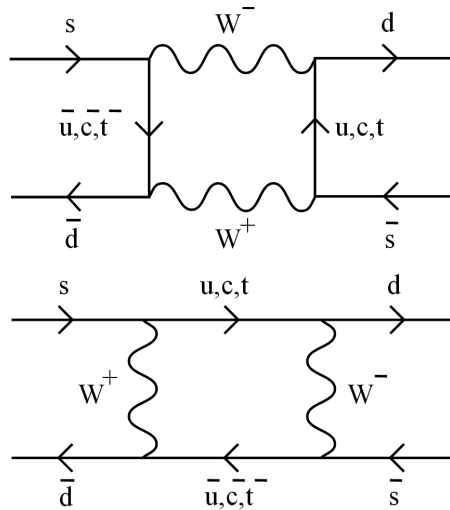


Figure 1.4: The two leading contributions to the amplitude of  $K^0-\bar{K}^0$  oscillation. [4].

In 1980, Carter and Sanda suggested the possibility of large  $CP$  violation in  $B$  meson decays [23]. In 2001, the "B-factories", including the BaBar Experiment at the Stanford Linear Accelerator Center (SLAC) and the Belle Experiment at the High Energy Accelerator Research Organization (KEK) in Japan, observed time-dependent  $CP$  violation in decays of the  $B$  mesons system [24]. The time-dependent  $CP$  violation is mainly due to the mixing of the neutral  $B$  mesons via the box diagram as that in the kaon system.

On the other hand, direct  $CP$  violation in standard model is due to interference between weak ( $\phi$ ) and strong ( $\delta$ ) amplitude. The amplitude of particle decay  $\mathcal{A}$  and of anti-particle  $\bar{\mathcal{A}}$  can be described by:



$$\begin{aligned}\mathcal{A} &= |T|e^{i(\delta_T - \phi_T)} + |P|e^{i(\delta_P - \phi_P)} \\ \bar{\mathcal{A}} &= |T|e^{i(\delta_T + \phi_T)} + |P|e^{i(\delta_P + \phi_P)}\end{aligned}\quad (1.14)$$

where  $T$  is the sum of amplitudes from tree diagrams while  $P$  from penguin diagrams. The  $CP$  asymmetry can be written as:

$$\mathcal{A}_{CP} = \frac{|\bar{\mathcal{A}}|^2 - |\mathcal{A}|^2}{|\bar{\mathcal{A}}|^2 + |\mathcal{A}|^2} = \frac{2|T||P| \sin(\delta_T - \delta_P) \sin(\phi_T - \phi_P)}{|T|^2 + |P|^2 + 2|T||P| \cos(\delta_T - \delta_P) \cos(\phi_T - \phi_P)} \quad (1.15)$$

### 1.3 Dalitz plot analysis

We can completely describe the kinematics of three-body  $B$  decays by using two variables. In general, the variables chosen are the squares of the invariant masses of two pairs of the decay products. For example, considering a decay  $B \rightarrow 1, 2, 3$ , we could plot  $M_{12}^2$  on y axis and  $M_{23}^2$  on x axis.

Dalitz plot utilizes the above mentioned two variables and is named after its inventor, Richard Dalitz, who introduced this technique in studying the decays of  $K$  mesons ( $K$  mesons were called as  $\tau$  meson at that time). By using this technique, physicists also have gotten fruitful results on decays of  $D$  mesons.

While a particle decays into three-body final state, it can be modeled through two-body decay with one of the two-body decay product immediately decaying into another two final state particles. There could be any physical non-uniform distributions on Dalitz plot, thus Dalitz analysis is an excellent tool to study the dynamics of three-body decays.







## Chapter 2

# Belle Experiment

The Belle experiment is designed to study the physics of CP-violation. It is conducted by the Belle Collaboration, an international collaboration of more than 400 physicists and engineers investigating, which located at the High Energy Accelerator Research Organisation (KEK) in Tsukuba, Ibaraki Prefecture, Japan. The Belle experiment includes two major facilities: the KEKB accelerator which is a  $e^+e^-$  asymmetric-energy collider, and the Belle detector which is a multilayer particle detector.

Fig.2.1 shows the bird's eye view of the organization.

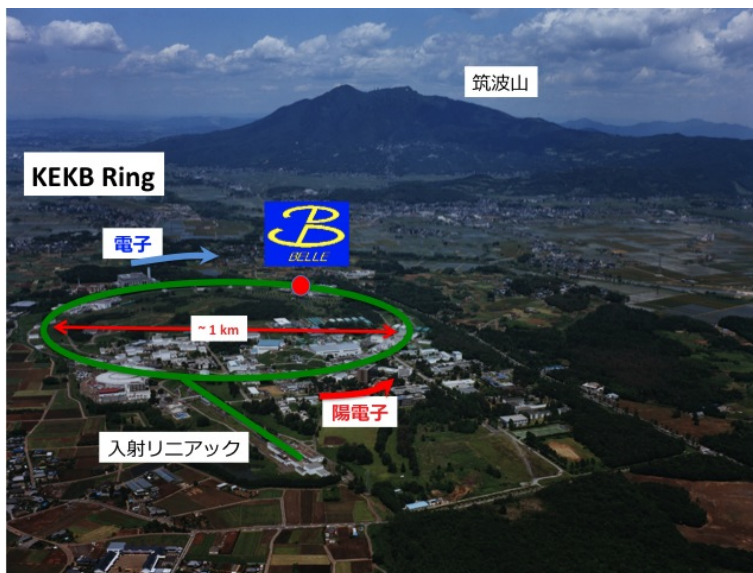


Figure 2.1: Bird's eye view of KEKB.



## 2.1 KEKB B-Factory

KEK B-factory (KEKB) is an asymmetric, two-ring,  $e^+e^-$  collider. 3.5 GeV  $e^+$  ring (LER) and 8 GeV  $e^-$  ring (HER) are placed side by side in the TRISTAN tunnel of about 3 km circumference. Fig.2.2 shows the layout of the two rings. There are straight sections in the circular tunnel named Fuji, Nikko, Tsukuba and Oho. A cross-over design in the Fuji area is used to insure exactly the same circumference for the two rings. The Belle detector is located in the interaction point in Tsukuba hall. The two rings cross at two points, but collide at only one point with only the Belle detector. The designed peak luminosity is at the order of  $10^{34} \text{cm}^{-2} \text{sec}^{-1}$ , corresponding to  $10^8$   $B\bar{B}$  pairs per year. The asymmetric  $e^+e^-$  collider is running at the energy of center-of-mass (CM) 10.58 GeV, which corresponds to the  $\Upsilon(4S)$  resonance just above the  $B\bar{B}$  production threshold. At this energy, the  $\Upsilon(4S) \rightarrow B\bar{B}$  reaction has a cross section of 1.05 nb and  $e^+e^- \rightarrow q\bar{q}$  ( $q = u, d, s, c$ ) process has a cross section of 3.7 nb. The objective of the Belle experiment is to perform definitive tests of the KM model prediction for CP violation in the decays of  $B$  mesons. CP violation effects are observed by measuring CP asymmetry in  $B^0$  decays into CP eigenstates. By measuring the distance between two vertices of  $B$  meson and  $\bar{B}$  meson with flavor identification enables us to measure CP asymmetry. The parameters of the KEKB accelerator are listed in Table.2.1. One of the most important features of KEKB is the finite angle crossing of  $\pm 11$  mrad.

The KEKB with the finite angle crossing scheme of  $\pm 11$  mrad has the following advantages.

- No parasitic collisions occur near the interaction point (IP).
- No bending magnet for beam separation is required. As a result the background due to synchrotron light is significantly reduced and a circular beam pipe instead of a racetrack one can be adopted.
- A room for superconducting solenoid magnet for compensation of the fringe field of the detector solenoid magnet.

In case the synchrotron-Betatron Resonance due to finite angle crossing becomes uncontrollable, we avoid it by rotating bunches by "crab cavities" which are placed close to IP and to have head-on collision of beams. The beam rotation by "crab cavities" is shown in Fig.2.3.

## 2.2. BELLE DETECTOR

The operation of KEKB was started in December, 1998 and turned off on 30 June, 2010. The instantaneous luminosity of  $1052 \text{ fb}^{-1}$  was accumulated by Belle detector. For a further investigating the KEKB accelerator and the Belle detector are now upgrading to SuperKEKB and Belle II, the luminosity is increased by a factor of 40.

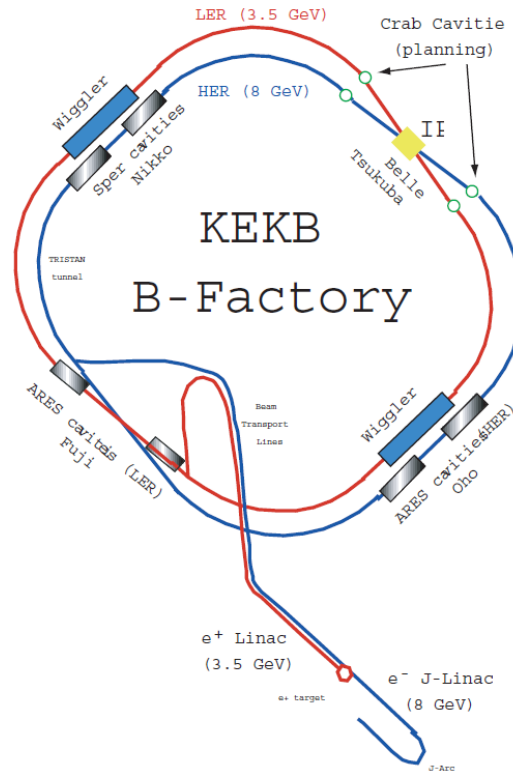


Figure 2.2: Schematic layout of KEKB. The Belle detector is located in the interaction point in Tsukuba hall on the northeast side of the KEKB rings.

## 2.2 BELLE Detector

The Belle collaboration was organized to study the physics of a high-luminosity, asymmetric  $e^+e^-$  collider operating at  $\Upsilon(4S)$  resonance. The objective of Belle experiments is to test the Kobayashi-Maskawa mechanism for CP-violation [25]. Fig.2.4 shows the configuration of the Belle detector. The detector is configured around a 1.5 T superconducting solenoid and iron structure surrounding the KEKB



Table 2.1: Parameters of KEKB accelerator [8].

Ring		LER	HER	Unit
Luminosity	L	$1 \times 10^{34}$		$\text{cm}^{-2}\text{sec}^{-1}$
Beam energy	E	3.5	8.0	GeV
Beam currents	I	2.6	1.1	A
Beta function at IP (H/V)	$\beta_x^*/\beta_y^*$	0.33/0.01		m
Circumference	C	3016.26		m
Horizontal crossing angle	$\theta_x$	$\pm 11$		mrad
Beam-beam parameters (H/V)	$\xi_x/\xi_y$	0.039/0.052		
Natural bunch length	$\sigma_z$	0.4		cm
Energy spread	$\sigma_\varepsilon$	$7.1 \times 10^{-4}$	$6.7 \times 10^{-4}$	
Bunch spacing	$s_b$	0.59		m
Particle/bunch	N	$3.3 \times 10^{10}$	$1.4 \times 10^{10}$	
Emittance	$\varepsilon_x/\varepsilon_y$	$1.8 \times 10^{-8}/3.6 \times 10^{-10}$		
Synchrotron	$\nu_s$	0.01 ~ 0.02		
Betatron tune	$\nu_x/\nu_y$	45.52/45.08	47.50/43.08	
Momentum compaction factor	$\alpha_p$	$1 \times 10^{-4} \sim 2 \times 10^{-4}$		
Energy loss/turn	$U_0$	0.81 <sup>†</sup> /1.5 <sup>††</sup>	3.5	MeV
RF voltage	$V_c$	5 ~ 10	10 ~ 20	MV
RF frequency	$f_{RF}$	508.887		MHz
Harmonic number	h	5120		
Longitudinal damping time	$\tau_\varepsilon$	43 <sup>†</sup> /23 <sup>††</sup>	23	ms
Total beam power	$P_b$	2.7 <sup>†</sup> /4.5 <sup>††</sup>	4.0	MW
Radiation power	$P_{SR}$	2.1 <sup>†</sup> /4.0 <sup>††</sup>	3.8	MW
HOM power	$P_{HOM}$	0.57	0.15	MW
Bending radius	$\rho$	16.3	104.5	m
Length of bending magnet	$l_B$	0.915	5.86	m

†: without wigglers, ††: with wigglers

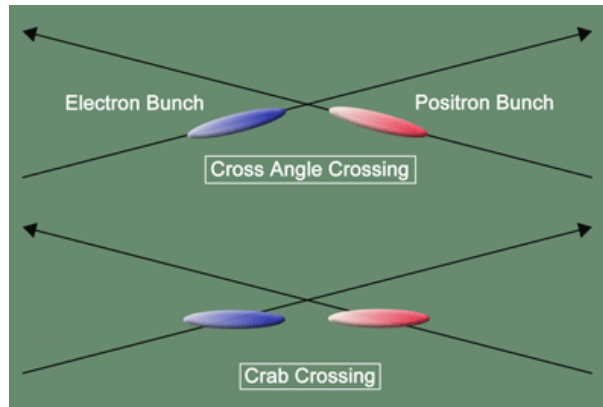


Figure 2.3: Beam rotation by crab cavities.

beam at the Tsukuba interaction region [26].  $B$ -meson decay vertices are measured by a silicon vertex detector (SVD) situated just outside of a cylindrical beryllium beampipe. Charged particle tracking is provided by a  $dE/dx$  measurements in a wire drift chamber (CDC). Particle identification is provided with the information measured in CDC, an array of aerogel Čerenkov counters (ACC) and a barrel-like arrangement of time-of-flight scintillation counters (TOF) situated radially outside of CDC. Electromagnetic showers are detected in an array of CsI( $Tl$ ) crystal calorimeter (ECL) located inside the solenoid coil. Muon and  $K_L$  mesons are identified by arrays of resistive plate counters interspersed in the iron flux-return which is located outside of the coil. The detector covers the  $\theta$  region extending from  $17^\circ$  to  $150^\circ$ . A part of the uncovered small-angle region is instrumented with a pair of BGO crystal arrays (EFC) placed on the surfaces of the QCS cryostat in the forward and backward directions. The performance of the detectors are summarized in Table.2.2. Descriptions of each sub-detector are included in the following sections.

### 2.2.1 Beam-line Magnets near the IP and Beam Pipe

The final-focus quadrupole magnets (QCS) are located inside the field volume of the detector solenoid and are common to both beams. In order to facilitate the high gradient and tunability, these magnets are superconducting at the expense of a large size. In order to minimize backgrounds from QCS generated synchrotron radiation, their axes are aligned with the incoming  $e^+$  and  $e^-$  beams. This re-

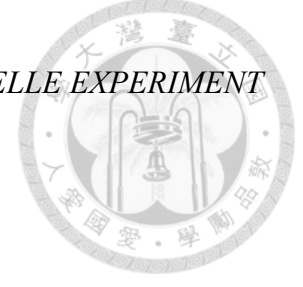


Table 2.2: Performance parameters for the Belle detector. There were two configuration of inner detectors used to collect two data sets. DS-I and DS-II, corresponding to a 3-layer SVD1 and a 4-layer SVD2 with a smaller beam pipe, respectively. [5]

Detector	Type	Configuration	Readout	Performance
Beam pipe for DS-I	Beryllium double wall	Cylindrical, $r = 20\text{mm}$ , $0.5/2.5/0.5(\text{mm}) = \text{Be/He/Be}$ w/He gas cooled		
Beam pipe for DS-II	Beryllium double wall	Cylindrical, $r = 15\text{mm}$ , $0.5/2.5/0.5(\text{mm}) = \text{Be/PF200/Be}$		
EFC	BGO	Photodiode readout Segmentation: 32 in $\phi$ ; 5 in $\theta$	$160 \times 2$	Rms energy resolution: 7.3% at 8 GeV 5.8% at 2.5 GeV
SVD1	Double-sided Si strip	3-layers: 8/10/14 ladders Strip pitch: $25(\text{p})/50(\text{n})\mu\text{m}$	$\phi$ : 40.96k $z$ : 40.96k	$\sigma(z_{CP}) \sim 78.0\mu\text{m}$ for $B \rightarrow \phi K_s^0$
SVD2	Double-sided Si strip	4-layers: 6/12/18/18 ladders Strip pitch: $75(\text{p})/50(\text{n})\mu\text{m}$ (layer 1-3) $73(\text{p})/65(\text{n})\mu\text{m}$ (layer 4)	$\phi$ : 55.29k $z$ : 55.296k	$\sigma(z_{CP}) \sim 78.9\mu\text{m}$ for $B \rightarrow \phi K_s^0$
CDC	Small cell drift chamber	Anode: 50 layers Cathode: 3 layers $r = 8.3 - 86.3 \text{ cm}$ $-77 \leq z \leq 160 \text{ cm}$	Anode: 8.4k Cathod: 1.8k	$\sigma_{r\phi} = 130\mu\text{m}$ $\sigma_z = 200 \sim 1400\mu\text{m}$ $\sigma_{Pt}/Pt = 0.3\% \sqrt{p_t^2 + 1}$ $\sigma_{dE/dx} = 0.6\%$
ACC	Silica aerogel	960 barrel/228 end-cap FM-PMT readout		$N_{p.e.} \geq 6$ $K/\pi$ separation: $1.2 < p < 3.5 \text{ GeV}/c$
TOF	Scintillator	128 $\phi$ segmentation $r = 120 \text{ cm}$ , 3-cm long	$128 \times 2$	$\sigma_t = 100 \text{ ps}$ $K/\pi$ separation: up to 1.2 GeV/c
TSC		64 $\phi$ segmentation	64	
ECL	CsI Towered-structure	Barrel: $r = 125 - 162 \text{ cm}$ End-cap: $z = -102 \text{ cm}$ and $+196 \text{ cm}$	6624 1152(F) 960(B)	$\sigma_E/E = 1.3\%/\sqrt{E}$ $\sigma_{pos} = 0.5 \text{ cm}\%/\sqrt{E}$ (E in GeV)
KLM	Resistive plate counters	14 layers (5 cm Fe + 4 cm gap) 2 RPCs in each gap	$\theta$ : 16k $\phi$ : 16k	$\Delta\phi = \Delta\theta = 30 \text{ mrad}$ for $K_L$ $\sim 1\%$ hadron fake
Magnet	Supercon.	Inner radius = 170 cm		$B = 1.5\text{T}$

## 2.2. BELLE DETECTOR

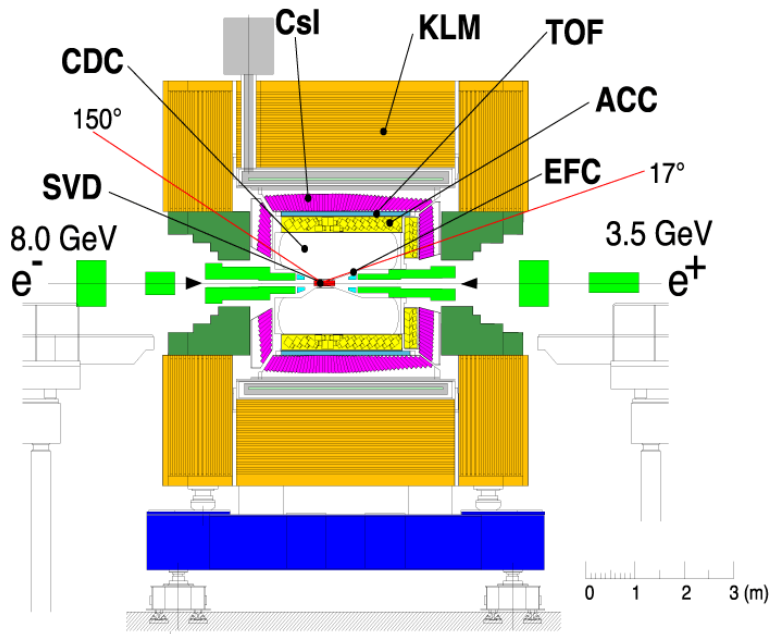


Figure 2.4: Side view of Belle detector [5].

quires the radius of the backward-angle region cryostat to be larger than that of the one in the forward-angle region. The QC1 magnets are located outside the QCS cryostats and help provide the vertical focus for the high energy beam only. Although these are normal conductor magnets with an iron return yoke, a special design is necessary because of the small beamseparation this region. The one in the forward region is a half-quadrupole with iron septum. In order to reduce the synchrotron radiation background from the incoming beam, the backward region QC1 is a full-quadrupole [8].

The precise determination of decay vertices is an essential feature of the Belle experiment. Multiple coulomb scattering in the beam-pipe wall and the first layer of the silicon detector are the limiting factors on the  $z$ -vertex position resolution, making the minimization of the beam-pipe thickness a necessity. Fig.2.5 shows the cross-section of the beryllium beam pipe at interaction point. The central part ( $-4.6 \text{ cm} \leq z \leq 10.1 \text{ cm}$ ) of the beam pipe is a double-wall beryllium cylinder with an inner diameter of 40 mm. A 2.5 mm gap between the inner and outer walls of the cylinder provides a helium gas channel for cooling. The machine vacuum is supported by the 0.5 mm thick inner wall. The outer wall is also 0.5 mm thick.



The beryllium central section is brazed to aluminum pipes that extend outside of the collision region as shown in Fig.2.6. The conical shape of the aluminum beam pipe allows the synchrotron X-ray generated in the QCS and QC1 magnets to pass through the detector region without hitting the beam pipe wall. The helium-gas cooling is adopted instead of water in order to minimize the material in the beam pipe.

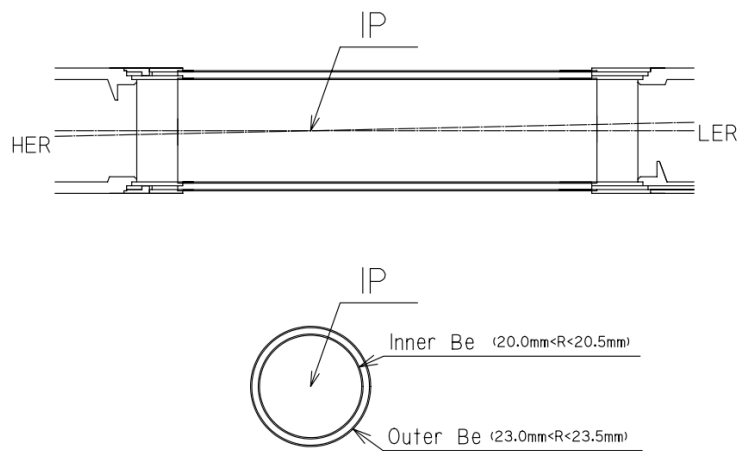


Figure 2.5: The cross-section of the beryllium beam pipe at interaction point [5].

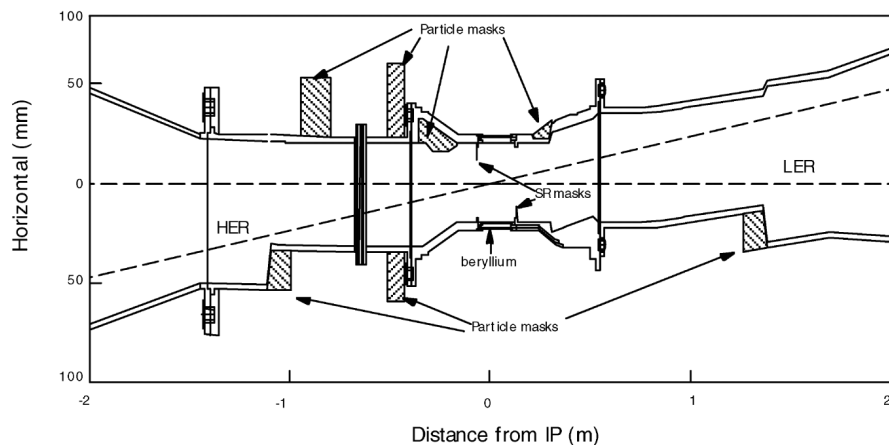


Figure 2.6: The arrangement of the beam pipe and horizontal masks [5].



## 2.2. BELLE DETECTOR

### 2.2.2 Extreme Forward Calorimeter (EFC)

The extreme forward calorimeter, EFC, further extend the polar angle coverage by ECL,  $17^\circ < \theta < 150^\circ$ . EFC covers the angular range from  $6.4^\circ$  to  $11.5^\circ$  in the forward direction (the  $e^-$  direction) and  $163.3^\circ$  to  $171.2^\circ$  in the backward direction (the  $e^+$  direction). The EFC detector is attached to the front faces of the cryostats of the compensation solenoid magnets of the KEKB accelerator, surrounding the beam pipe [27] [28]. EFC is also required to function as a beam mask to reduce backgrounds for CDC. In addition, EFC is used for a beam monitor for the KEKB control and a luminosity monitor for the Belle experiment. It can also be used as a tagging device for two-photon physics.

Since EFC is placed in the very high radiation level area around the beam pipe near the interaction point, due to the long-term exposure to high radiation level, it is required to be radiation-hard. we choose the BGO (Bismuth Germanate,  $\text{Bi}_4\text{Ge}_3\text{O}_{12}$ ) crystal calorimeter because it costs less in terms of money and manpower and gives better energy resolution [29]. BGO has very desirable characteristics for electromagnetic calorimeters:

- radiation hardness at megarad level,
- excellent  $e/\gamma$  energy resolution of  $(0.3 - 1)\%/\sqrt{E(\text{GeV})}$ ,
- high density of  $7.1 \text{ gm/cm}^3$ ,
- short radiation length of  $1.12 \text{ cm}$ ,
- large refractive index of  $2.15$ ,
- suitable scintillating properties with the fast decay time of about  $300 \text{ ns}$  and peak scintillation at about  $480 \text{ nm}$ ,
- non-hygroscopic nature.

Pure BGO crystals with silicon photodiodes were proven to be capable of detecting minimumionizing particles (MIPs) with a large S/N ratio [30]. In the same experiment the nuclear counter effect (NCE) was also clearly observed.

The finer lateral segmentation can provide the better position resolution. The segmentation, however, is limited by front-end electronics. The detector is segmented into 32 in  $\phi$  and 5 in  $\theta$  for both the forward and backward cones. A three dimensional view of the crystal arrangement is shown in Fig.2.7.

The energy sum spectra for Bhabha events show a correlation between the forward and backward EFC detectors. A clear peak at  $8 \text{ GeV}$  with an RMS resolution

of 7.3 % is seen for the forward EFC, while a clear peak at 3.5 GeV with an RMS resolution of 5.8 % is seen in the backward EFC. These results are compatible with the beam test results [31] and are slightly worse than those obtained by a GEANT Monte Carlo simulation. The discrepancies are due to dead channels and crystal-to-crystal non-uniformity. An expected counting rate for Bhabha events is a few kHz at an ultimate luminosity of  $10^{34}\text{cm}^{-2}\text{sec}^{-1}$

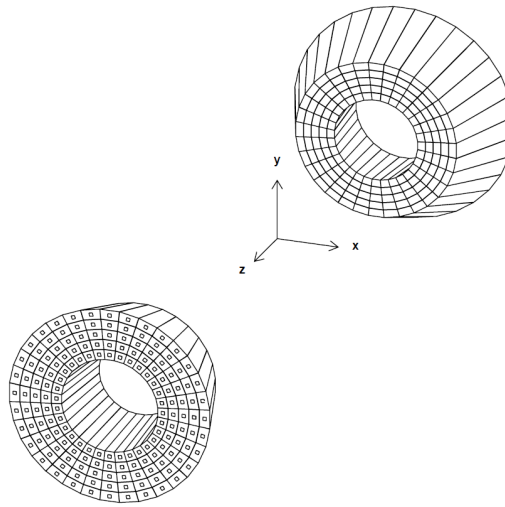


Figure 2.7: An isometric view of the BGO crystals of the forward and backward EFC detectors [5].

### 2.2.3 Silicon Vertex Detector (SVD)

A primary goal of the Belle experiment is to observe time-dependent CP asymmetries in the decays of B mesons. Doing so requires the measurement of the difference in z-vertex positions for B meson pairs with a precision of  $\sim 100 \mu\text{m}$ . The Belle Silicon vertex Detector, SVD improve the tracking of charged particles and therefore allow the determination of the *B* decay vertices.

The initial version of SVD (SVD1) had been working since 1999. Due to the gain decrease resulting from accumulated radiation damage, the original SVD (SVD 1.0) was partial replaced several times. All SVD1 version has similar geometrical and electrical configuration, except for the improvement in radiation hardness made in the silicon sensors and in the front-end electronics. SVD1 consists of three concentric cylindrical layers of double-sided silicon strip detector

## 2.2. BELLE DETECTOR

(DSSD) containing 8/10/14 ladders in each along  $\phi$  in layer 1/2/3, respectively. It covers the angle range  $23^\circ < \theta < 139^\circ$  where  $\theta$  is the angle from the beam axis, which corresponds to 86% of the full solid angle. Each ladder is made of two joined half-ladders, and each half-ladder contains one or two DSSDs which are supported by boron-nitride (BN) ribs sandwiched with carbon-fiber reinforced plastic (CFRP). Each module consists of a detector unit and a hybrid unit, as shown in Fig.2.8, it also shows the end and side views of SVD.

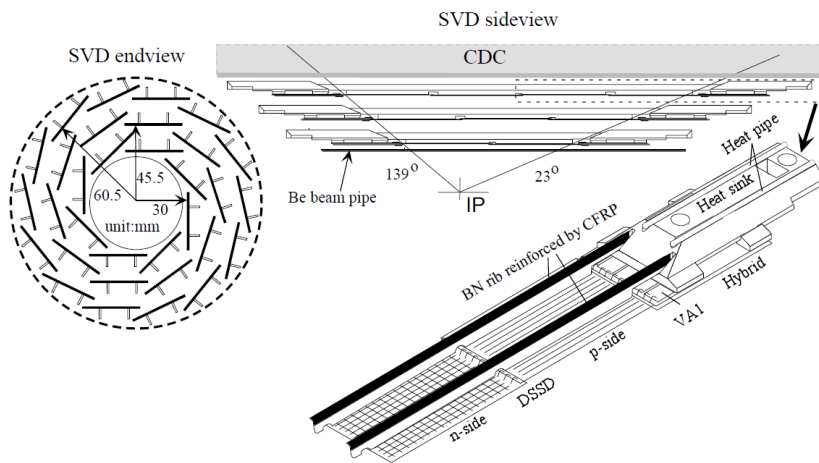


Figure 2.8: Detector configuration of SVD1 [5].

New SVD (SVD2) had been installed in the summer of 2003 [32] [33], it contains four detector layers, the radii are 20.0, 43.5, 70.0 and 88.0 mm, respectively. This enables us to reconstruct charged tracks using only the SVD hit information. The angular acceptance is expanded to  $17^\circ < \theta < 150^\circ$  which is the same as the outer tracker (Central Drift Chamber). The radius of the beam pipe is reduced from 20 to 15 mm so that we can place the sensor closer to the interaction point and achieve a better vertex resolution. A simulation study shows that the impact parameter resolution improves by 20 - 25 % in the low-momentum region. We use DSSD fabricated by Hamamatsu Photonics. DSSDs are connected to form a ladder structure. In layer 1/2/3/4, we have 2/3/5/6 DSSDs along the  $z$  direction in a ladder, and 6/12/18/18 ladders to cover all the  $\phi$  region, respectively. SVD2 successfully performs a better resolution and a higher radiation hardness than SVD1. Fig.2.9 shows the end view comparison of SVD1 and SVD2.

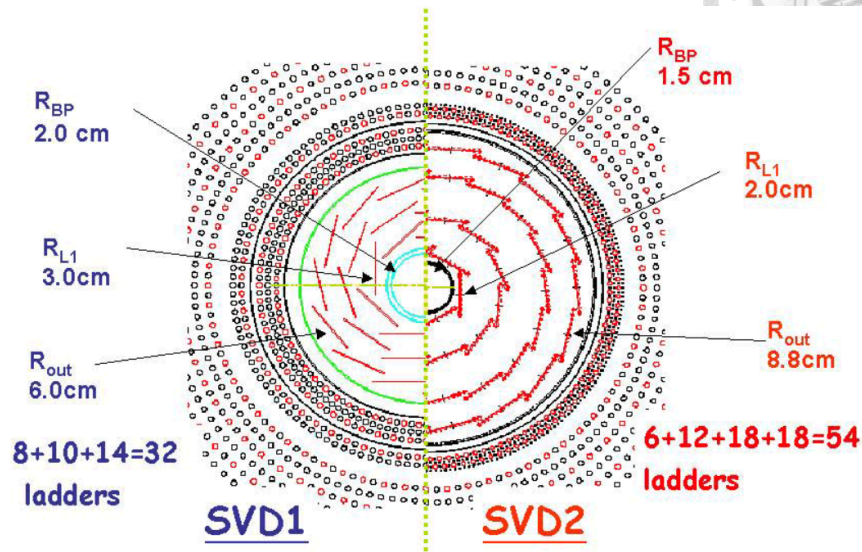


Figure 2.9: End view comparison of SVD1 and SVD2 [6].

#### 2.2.4 Central Drift Chamber (CDC)

The Belle central drift chamber, CDC, was designed and constructed to satisfy the requirements for the central tracking system [34] [35]. Since the majority of the decay particles of a  $B$  meson have momentum lower than 1 GeV/c, the minimization of multiple scattering is important for improving the momentum resolution. Therefore, the use of a low- $Z$  (atomic number) gas is helpful to reduce multiple coulomb scattering contribution and improve the momentum resolution.

The structure of CDC is shown in Fig.2.10. It is asymmetric in the  $z$  direction in order to provide an angular coverage of  $17^\circ < \theta < 150^\circ$ . The longest wires are 2400 mm long. The inner radius is extended down to 103.5 mm without any walls in order to obtain good tracking efficiency for low- $p_t$  tracks by minimizing the material thickness. The outer radius is 874 mm. The chamber has 50 cylindrical layers, each containing between three and six either axial or small-angle-stereo layers, and three cathode strip layers. Fig.2.12 shows the cell arrangement of drift cells and the structure near cathode part. CDC has a total of 8400 drift cells. We have selected a 50 % helium (He) - 50% ethane ( $C_2H_6$ ) gas mixture. This mixture has long radiation length about (640 m) and a drift velocity that saturates at 4 cm/ $\mu$ s at a relatively low electric field [36] [37]. The large portion ethane is

## 2.2. BELLE DETECTOR

chosen because it provide a good  $dE/dx$  resolution.

The truncates-mean method was employed to estimate the most probable energy loss, it is a useful variable for particle identification, especially for the separation of  $K^\pm$  and  $\pi^\pm$  in the momentum region below 0.5 GeV/c. The largest 20 % of measured  $dE/dx$  values for each track were discarded and the remaining data were averaged in order to minimize occasional large fluctuations in the Landau tail of the  $dE/dx$  distribution. A scatter plot of measured  $\langle dE/dx \rangle$  distribution and particle momentum is shown in Fig.2.11, together with the expected mean energy losses for different particle species.

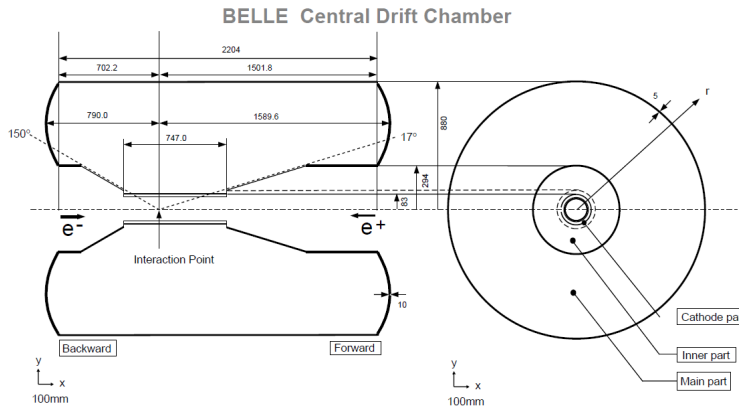


Figure 2.10: Overview of the CDC structure. The lengths in the figure are in units of mm [5].

### 2.2.5 Aerogel Čerenkov Counter System (ACC)

An array of silica aerogel threshold Čerenkov counters is part of the Belle particle identification system, specifically to distinguish  $\pi/K$ . It extend the momentum coverage beyond the reach of  $dE/dx$  measurements by CDC and TOF. Fig.2.13 show the configuration of the aerogel Čerenkov Counter System (ACC) in a central part of the Belle detector. The ACC consists of 960 counter modules segmented into 60 cells in the  $\phi$  direction for the barrel part and 228 modules arranged in a 5 concentric layers for the forward end-cap part of the detector.

In order to detect the Čerenkov light effectively, one or two fine mesh-type photomultiplier tubes (FM-PMTs), which operate in a magnetic field of 1.5 T. Two FM-PMTs are installed for the barrel ACC modules and one for the end-cap ACC

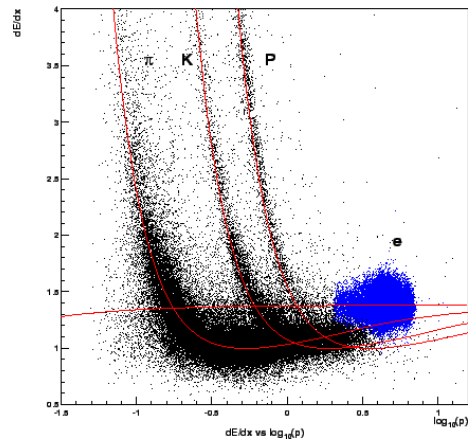
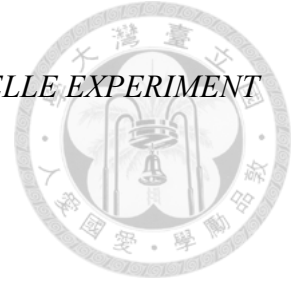


Figure 2.11: Truncated mean of  $dE/dx$  versus momentum observed in collision data. The expected results for  $K$ ,  $\pi$ , proton and  $e$  are shown by solid red curves. Unit of the momentum is GeV/c.

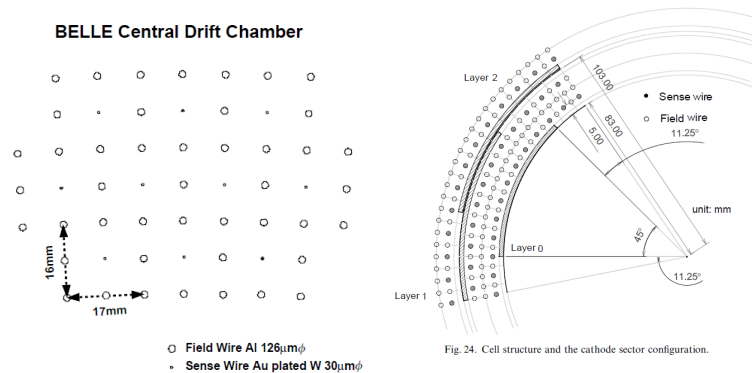


Figure 2.12: Cell structure and the cathode sector configuration of CDC [5].

## 2.2. BELLE DETECTOR

modules, as shown in Fig.2.14. We adopted the two-step method for the preparation of alcogels, in which we used a methylalkoxide oligomer as the precursor [38]. This oligomer is hydrolyzed and polymerized in a basic catalyst ( $\text{NH}_4\text{OH}$ ) in a solution of methanol ( $\text{CH}_4\text{O}$ ) or ethanol ( $\text{C}_2\text{H}_6\text{O}$ ). Silica ( $\text{SiO}_2$ ) aerogels have been used in several experiments, however, their transparencies become worse with in a few years of use. This phenomenon may be attributed to the hydrophilic property of the silica aerogels. In order to prevent such effects, we have made our silica aerogels highly hydrophobic by changing the surface hydroxyl groups into trimethylsilyl groups. This modification is applied before the drying. As a result of this treatment, our silica aerogels are still as transparent as they were when they were produced about two years ago. In the barrel ACC each row has on average 60 boxes and the row number is given from left to right in Fig.2.13. The layer number of the end-cap ACC is given from the inner to the outer side. The light yield for the  $\mu$  tracks depends on the refractive index of aerogel radiators, size and number of FM-PMTs attached on the counter module, and geometry of the counter module box. The light yield ranges from 10 to 20 for the barrel ACC and from 25 to 30 for the end-cap ACC, high enough to provide useful  $\pi/K$  separation.

The performance of ACC modules has been tested at the  $\pi 2$  beam line at KEK.  $\pi^\pm$  and  $p^\pm$  are clearly separated by more than three standard deviations. A clear separation between  $e^\pm$  and  $K^\pm$  is also observed using Bhabha and hadronic events. Careful calibration for the pulse height of each signal were performed for  $e^+e^- \rightarrow \mu^+\mu^-$  events. The light yields for the muon tracks are depend on the index of refraction of each aerogel tile, the geometry of each ACC module, and the installed PMTs.

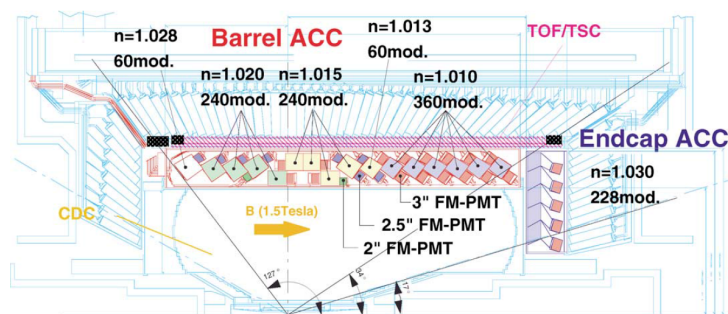


Figure 2.13: The arrangement of ACC at the central part of the Belle detector. [5].



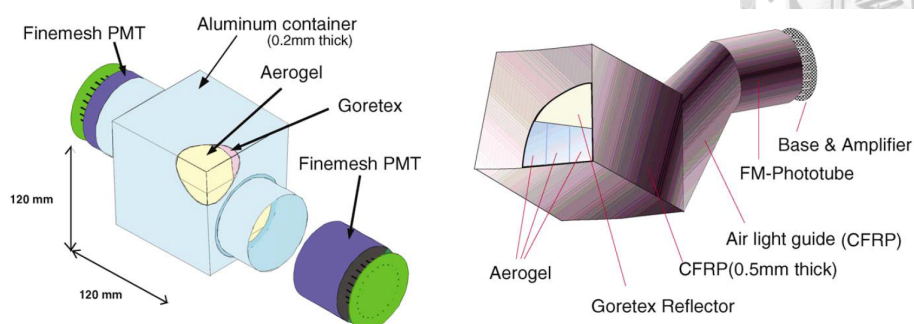


Figure 2.14: Schematic drawing of a typical ACC counter module: (a) barrel and (b) end-cap ACC. [5].

## 2.2.6 Time-of-Flight Counters (TOF)

A time-of-flight (TOF) detector system using plastic counters is very powerful for particle identification in  $e^+e^-$  collider detectors. For a 1.2 m flight path, the TOF system with 100 ps time resolution is effective for particle momentum below about 1.2 GeV/c, which encompasses 90 % of the particles produced in  $\Upsilon(4S)$  decays. It can provide clean and efficient  $b$ -flavor tagging.

In addition to particle identification, the TOF counters provide fast timing signals for the trigger system to generate gate signals for ADCs and stop signals for TDCs. To avoid pile-up in the trigger queue, the rate of the TOF trigger signal must be kept below 70 kHz. The gate and stop timing for the CsI calorimeter and CDC sets a time jitter requirement of less than  $\pm 10$  ns. Simulation studies indicate that to keep the fast trigger rate below 70 kHz in any beam background conditions the TOF counters should be augmented by thin trigger scintillation counters (TSC) [39].

To achieve the 100 ps design goal, the following strategies were adopted:

- (1) use of a fast scintillator with an attenuation length longer than 2.5 m,
- (2) elimination of light guides to minimize the time dispersion of scintillation photons propagating in the counter,
- (3) use of photo-tubes with largearea photo-cathodes to maximize photon collection.

These considerations led us to a configuration with fine-mesh-dynode photo-multiplier tubes (FM-PMT) mounted directly on the TOF and TSC scintillation

## 2.2. BELLE DETECTOR

counters and placed in a magnetic field of 1.5 T.

The design of one TOF module (the entire system comprises 64 modules) is shown in Fig.2.15. Each module consists of two TOF counters with readout at both ends, and one thin trigger scintillation counters (TSC) with the backward readout only. The acceptance is  $34^\circ - 120^\circ$  in polar angle, and the minimum transverse momentum to reach a TOF counter is 0.28 GeV/c.

The resolution for the weighted average time is about 100 ps with small  $z$  dependence. Fig.2.16 shows the mass distribution for each track in hadron events, calculated from Eq.(2.1):

$$M^2 = \left(\frac{1}{\beta^2} - 1\right)P^2 = \left(\left(\frac{cT_{obs}^{twc}}{L_{path}}\right)^2 - 1\right)P^2 \quad (2.1)$$

where  $\beta$  is the speed relative to light;  $T_{obs}^{twc}$  is the observed time of flight; the particle momentum  $P$  and path length  $L_{path}$  to the TOF counter are from the CDC track fit assuming a muon mass;  $c$  is the light velocity.

Fig.2.16 shows clear  $\pi^\pm$ ,  $K^\pm$  and proton peaks. The data points (spot point) are in good agreement with the MC prediction (histogram), assuming  $\sigma_{TOF} = 100$  ps.

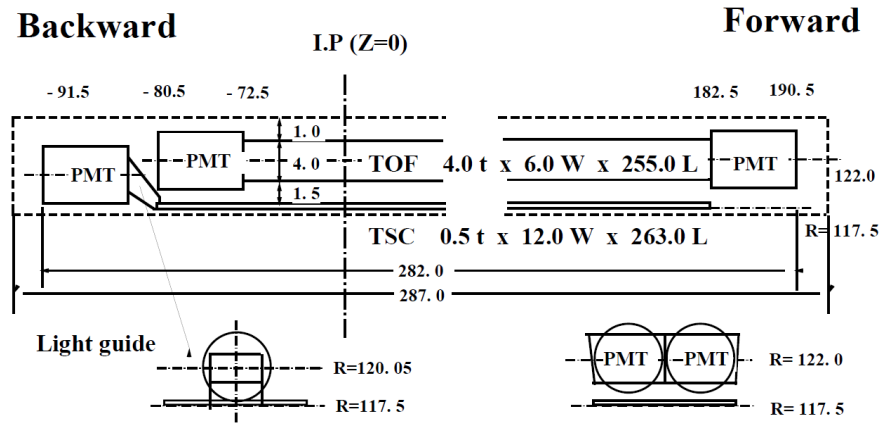


Figure 2.15: Dimensions of a TOF/TSC module. [5].

### 2.2.7 Electromagnetic Calorimeter (ECL)

The main purpose of the ECL is to detect the photons from  $B$  decays with high efficiency and good resolution in energy and position. Electromagnetic identifica-

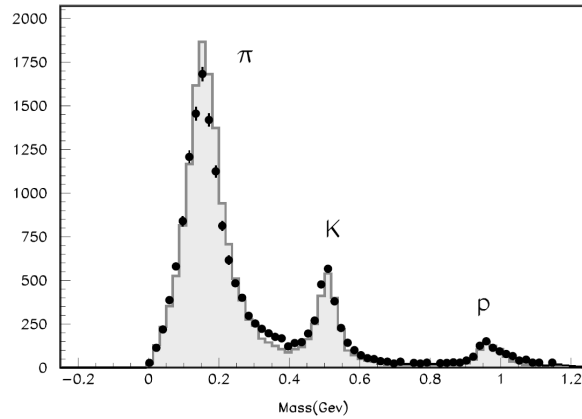
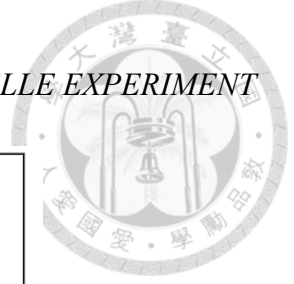


Figure 2.16: Mass distribution from TOF measurements for particle momenta below 1.2 GeV/c. [5].

tion also relies on the energy deposit measured by ECL [40]. High momentum  $\pi^0$  detection needs the separation of two nearby photons and a precise determination of their opening angle, thus a fine-gained segmentation in ECL is required.

The Belle ECL consists of 8736 CsI(Tl) crystals with silicon photodiode read-out. Out of these, the barrel calorimeter has 6624, while the forward and the backward end-cap calorimeters have 1152 and 960 counters, respectively, as shown in Fig.2.17. The coverage in the polar angle ( $\theta$ ) with respect to the electron beam axis is about  $12.4^\circ < \theta < 155.1^\circ$  in the laboratory frame. The barrel part has 1250 mm inner radius. The mechanical support structure is comprised of an aluminum inner wall and fins suspended from stainless-steel-made reinforcing bars and outer walls. Each crystal has a tower-like shape and is arranged toward IP. The geometrical configuration is shown in Table.2.3. Typical dimension of a crystal for the barrel region is  $5.5 \times 5.5 \text{ cm}^2$  in the front face and  $6.5 \times 6.5 \text{ cm}^2$  in the rear face, while dimensions of the end-cap crystals have large variation. The 30 cm length (16.2 radiation) lengths is chosen to avoid determination of the energy resolution at high energy due to the fluctuations of shower leakages out the rear of the counter.

Using calibrated counter hits, the shower is reconstructed as following steps. First, we look for a "seed counter" which has the highest energy deposit among neighboring crystals and exceeds 10 MeV. Then inside the  $5 \times 5$  matrix, which is the crystal group formed by 25 counters including the seed counter, the recorded

## 2.2. BELLE DETECTOR

hits are gathered to obtain the shower and position due to electromagnetic shower behavior are applied using the information given by Monte Carlo simulation (MC). After the KEKB collider was commissioned in June 1999, a large number of Bhabha and  $\gamma\gamma$  events have been accumulated to perform the absolute counter-by-counter calibration. The energy resolution was achieved to be 1.7 % for the barrel ECL, and 1.74 % and 2.85 % for the forward and backward ECL, respectively.

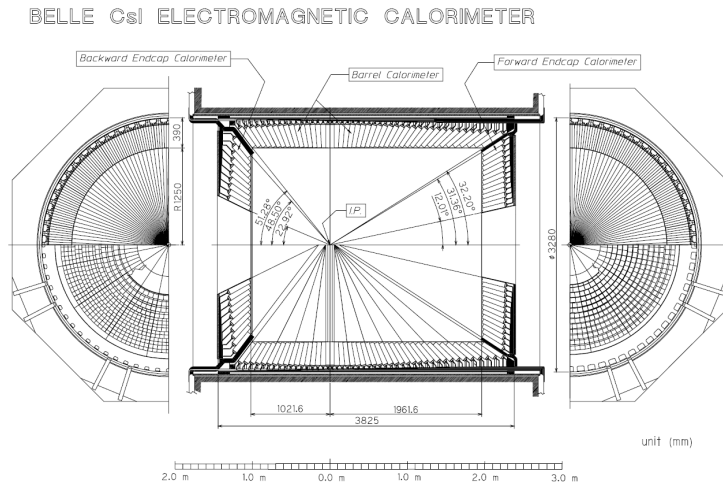


Figure 2.17: Overall configuration of ECL. [5].

Table 2.3: Geometrical parameters of ECL. [5].

Item	$\theta$ coverage	$\theta$ seg.	$\phi$ seg.	No. of crystals
Forward end-cap	$12.4^\circ < \theta < 31.4^\circ$	13	48 - 144	1152
Barrel	$32.2^\circ < \theta < 128.7^\circ$	46	144	6624
Backward end-cap	$130.7^\circ < \theta < 155.1^\circ$	10	64 - 144	960

### 2.2.8 Particle Identification of Electrons and Charged Kaons, EID and KID

In the analyses of physics data of Belle, EID and KID are performed by using data samples measured with CDC, ACC, TOF, and ECL.



### EID and the fake rate

Electrons are identified by using the following discriminants:

- the ratio of energy deposited in ECL and charged track momentum measured by CDC,
- transverse shower shape at ECL,
- the matching between a cluster at ECL and charged track position extrapolated to ECL,
- $dE/dx$  measured by CDC,
- light yield in ACC,
- time-of-flight measured by TOF.

We made probability density functions (PDF) for the discriminants beforehand. Based on each PDF, likelihood probabilities are calculated with track-by-track basis, and unified into a final likelihood output. This likelihood calculation is carried out taking into account the momentum and angular dependence.

### KID and pion fake rate

The  $K/\pi$  identification is carried out by combining information from three nearly independent measurements:

- $dE/dx$  measured by CDC,
- time-of-flight measured by TOF,
- measurement of the number of photoelectrons ( $N_{pe}$ ) in the ACC.

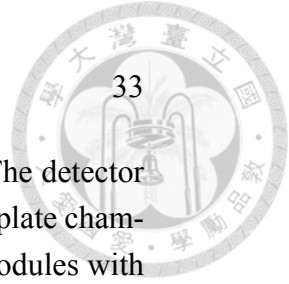
As in the case of EID, the likelihood function for each measurement was calculated and the product of the three likelihood functions yields the overall likelihood probability for being a kaon or a pion,  $P_K$  or  $P_\pi$ . A particle is then identified as a kaon or a pion by cutting on the likelihood ratio (PID):

$$PID(K) = \frac{P_K}{P_K + P_\pi} \quad (2.2)$$

$$PID(\pi) = 1 - PID(K) \quad (2.3)$$

### 2.2.9 $K_L$ and Muon Detection System (KLM)

The KLM detection system was designed to identify  $K_L$ 's and muons with high efficiency over a broad momentum range greater than 600 MeV/c. The KLM is



## 2.2. BELLE DETECTOR

comprised of the octagonal-shaped barrel and two end-cap regions. The detector consists of alternating layers of 3.7 cm thick glass-electrode resistive plate chamber (RPC) modules and 4.7 cm thick iron plates. The barrel has 15 modules with 14 iron plates, and each end-cap has 14 modules with 14 iron plates. The modules are rectangular in the barrel region (2 per octant layer) and fan-shaped (4 per layer) in the end-cap, see Fig.2.18. The barrel region covers the polar angular range from  $51^\circ$  to  $117^\circ$ ; the two end-cap extend this coverage to between  $25^\circ$  and  $145^\circ$ . The iron plates provide a total of 3.9 interaction lengths of material for a hadron crossing at normal incidence; this is in addition to the 0.8 interaction lengths of the ECL. Each RPC module contains two independent RPCs arranged back-to-back, sandwiched between orthogonal readout strip planes. This redundant superlayer design provides a three-dimensional measurement of the coordinates of a through-going charged track with better than 98 % efficiency, since a streamer that develops in either RPC will induce an image charge on both readout strip planes. The time resolution of the RPC signals is a few nanoseconds.

The rectangular  $z$ - and  $\phi$ -view readout strips in the barrel are roughly 5 cm wide. The  $\theta$ -view readout strips in the end-cap are 3.6 cm wide coaxial arcs, while the  $\phi$ -view readout strips are radial trapezoids of width 1.9 cm at the inner radius of 130.5 and 4.7 cm at the outer radius of 331.0 cm. There are a total of 38,000 readout strips in the system. The relatively high resistance of the glass  $\approx 5 \times 10^{12} \Omega \text{ cm}$ , limits the rate capability of these counters to  $\approx 0.2 \text{ Hz/cm}^2$ . However, in the present application in which the particle flux is little more than the cosmic ray flux, the detectors function with high efficiency. Signals typically have a 100 mV peak into a  $50 \Omega$  termination and have a full width at half maximum of less than 50 ns.

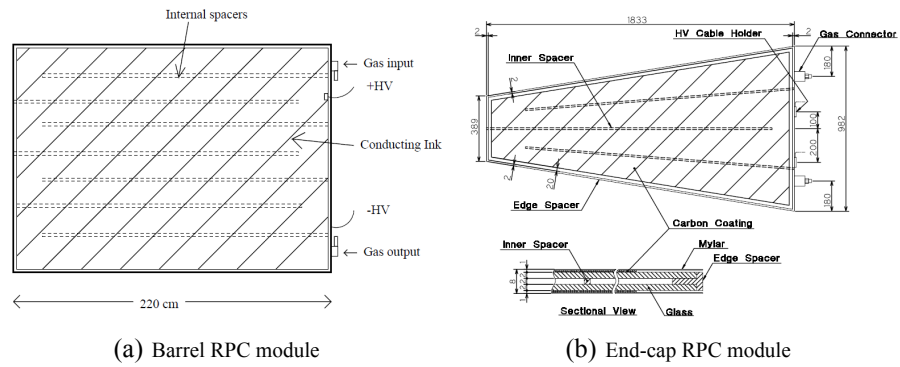
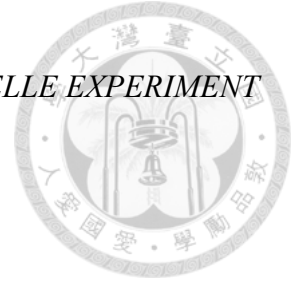


Figure 2.18: Schematic diagram of the internal spacer arrangement in the KLM detector. [5].



## Chapter 3

# *B* Reconstruction and Event Selection

In this paper, we report the current measurements of branching fractions and CP asymmetries for *B* charmless three-body decays,  $B^0(\bar{B}^0) \rightarrow \eta K^+ \pi^- (\eta K^- \pi^+)$ . There are three particles in final state, it includes two charged particles (*K* and  $\pi$ ) and one neutral particle  $\eta$ . We consider following final states:  $B \rightarrow \eta(\gamma\gamma)K\pi$  and  $B \rightarrow \eta(\pi^+ \pi^- \pi^0)K\pi$ .

This analysis is based on the data collected by Belle detector at the KEKB asymmetric-energy  $e^+e^-$  collider at the  $\Upsilon(4S)$  resonance. The total data sample consists of  $771.581 \pm 10.566$  million  $B\bar{B}$  pairs. Table.3.1 ~ Table.3.3 show the branching ratios of intermediate states for  $B^0(\bar{B}^0) \rightarrow \eta K^+ \pi^- (\eta K^- \pi^+)$  decay measured by previous study in PDG.

We combine  $K^+(K^-)$ ,  $\pi^-(\pi^+)$ ,  $\eta$  to form a  $B^0(\bar{B}^0)$  candidate for the decay,  $B^0(\bar{B}^0) \rightarrow \eta K^\pm \pi^\mp$ , *K* and  $\pi$  carry opposite electronic charge.

Two  $\eta$  decay branches are considered,  $\eta \rightarrow \gamma\gamma$  and  $\eta \rightarrow \pi^+ \pi^- \pi^0$ .

### 3.1 Charged Particle Selection

The track of charged particles from *B* are constrained to be through interaction point(IP),  $|\Delta r| < 0.3$  cm and  $|\Delta z| < 3.0$  cm.

Distinguishing *K*'s and  $\pi$ 's from *B* by  $\text{atc\_pid}(3,1,5,K/\pi) > 0.6$  for kaons and  $\text{atc\_pid}(3,1,5,K/\pi) < 0.4$  for pions. Tracks that are highly electron like ( $e\_id > 0.95$ ) or muon like ( $\mu\_id > 0.95$ ) are rejected.



Table 3.1: The branching ratio in  $B \rightarrow \eta K^*(892)^0$  is  $15.9 \pm 1.0$  in PDG.

Branching Ratio ( $10^{-6}$ )	Author	TECH	Comment
$15.2 \pm 1.2 \pm 1.0$	Wang	2007B BELL [11]	$e + e^- \rightarrow \Upsilon(4S)$
$16.5 \pm 1.1 \pm 0.8$	Aubert	2006H BABR [10]	$e + e^- \rightarrow \Upsilon(4S)$
$13.8^{+5.5}_{-4.6} \pm 1.6$	Richichi	2000 CLE2 [41]	$e + e^- \rightarrow \Upsilon(4S)$

Table 3.2: The branching ratio in  $B \rightarrow \eta K_0^*(1430)^0$  is  $11.0 \pm 2.2$  in PDG.

Branching Ratio ( $10^{-6}$ )	Author	TECH	Comment
$11.0 \pm 1.6 \pm 1.5$	Aubert	2006H BABR [10]	$e + e^- \rightarrow \Upsilon(4S)$

Table 3.3: The branching ratio in  $B \rightarrow \eta K_2^*(1430)^0$  is  $9.6 \pm 2.1$  in PDG.

Branching Ratio ( $10^{-6}$ )	Author	TECH	Comment
$9.6 \pm 1.8 \pm 1.1$	Aubert	2006H BABR [10]	$e + e^- \rightarrow \Upsilon(4S)$

Table 3.4: The branching ratio in  $\eta$  decay in PDG.

Decay mode	Branching Ratio (%)
$\gamma \gamma$	$39.31 \pm 0.20$
$\pi^+ \pi^- \pi^0$	$22.74 \pm 0.28$



### 3.2. $\eta$ RECONSTRUCTION

## 3.2 $\eta$ Reconstruction

**In  $\eta \rightarrow \gamma\gamma$  reconstruction**, the energy of the photons forming the  $\eta$  is required to be greater than 50 MeV. In order to reject soft photon background, we adopt  $|\cos(\theta_{heli})| < 0.9$  selection in  $\eta(\gamma\gamma)$  reconstruction, where  $\theta_{heli}$  is the angle between the photon direction and  $B$  candidate direction in  $\eta$  rest frame. Finally,  $\eta$  candidates are removed if either of the daughter photons can be combined with any other photon with  $E_\gamma > 100\text{MeV}$  to a  $\pi^0$  candidate.

**In  $\eta \rightarrow \pi^+\pi^-\pi^0$  reconstruction**,  $\pi^0$  candidate is chosen from Mdst\_ $\pi^0$  bank with photon energy above 50 MeV. The reconstructed  $\pi^0$  mass is required to be within 115 MeV/ $c^2$  and 152 MeV/ $c^2$ . Two charged pions are constrained to run through interaction point(IP), and distinguish pions from kaons by  $atc\_pid(3,1,5,K/\pi) < 0.4$ .

The final  $\eta$  candidates are selected by requiring the mass window cuts:  $500 < M_\eta < 575$  MeV/ $c^2$  for  $\eta \rightarrow \gamma\gamma$  and  $537.5 < M_\eta < 558$  MeV/ $c^2$  for  $\eta \rightarrow \pi^+\pi^-\pi^0$ .

Fig.3.1 shows the  $\eta$  mass distribution in data, Fig.3.2 ~ Fig.3.3 shows the  $\eta$  mass distribution in MC, Fig.3.4 shows the  $\pi^0$  mass distribution in data and MC.

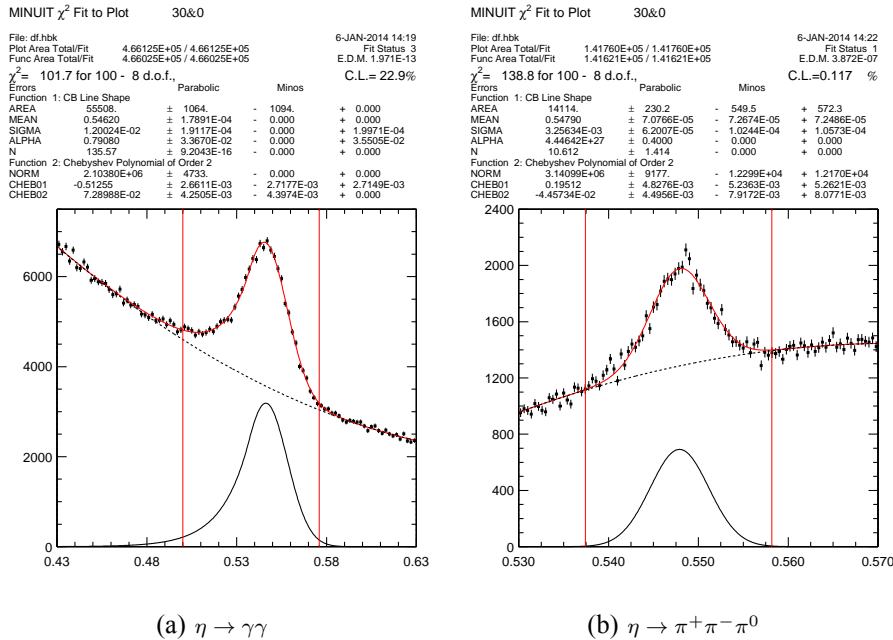


Figure 3.1: Invariant  $\eta$  mass distribution in data sample.

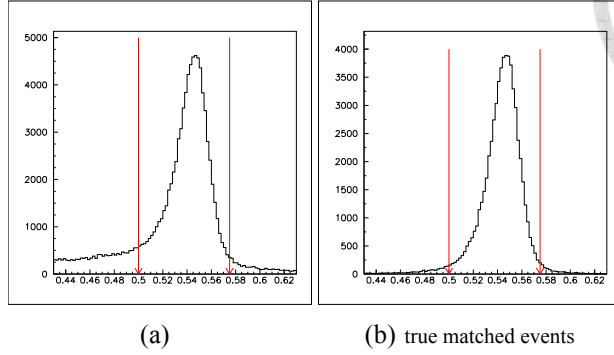
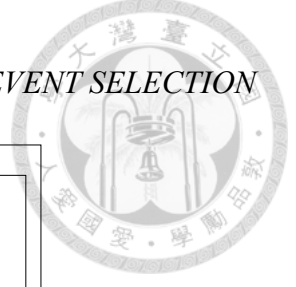


Figure 3.2: Invariant  $\eta$  mass distribution after all selections of  $\eta \rightarrow \gamma\gamma$  with three-body phase space decay in signal MC.

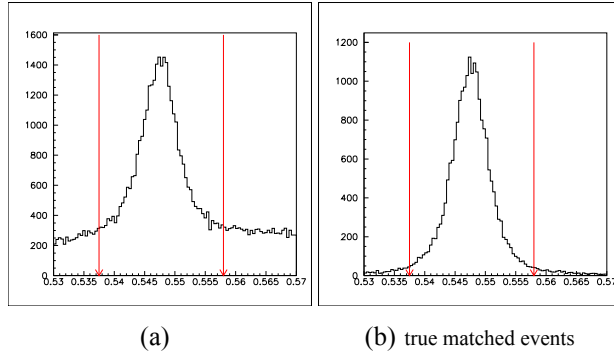


Figure 3.3: Invariant  $\eta$  mass distribution after all selections of  $\eta \rightarrow \pi^+ \pi^- \pi^0$  with three-body phase space decay in signal MC.

### 3.3 Best Candidate Selection

Assume that there is only one  $B_{cand}$  in each event, there should be a selection to choose one  $B$  candidate. Due to the  $\gamma$  caught uncertainty of detector and soft  $\gamma$  background, the best  $B$  candidate is chosen by closest  $\eta$  mass compared to  $\eta_{PDG}$  ( $547.853 \text{ MeV}/c^2$ ) for  $\eta \rightarrow \gamma\gamma$  mode and closest  $\pi^0$  mass compared to  $\pi^0_{PDG}$  ( $134.9766 \text{ MeV}/c^2$ ) for  $\eta \rightarrow \pi^+ \pi^- \pi^0$  mode. After mass selection, if there are still multiple  $B$  candidates with the same  $\eta$  (or  $\pi^0$ ) candidate, then choose the smallest  $\chi^2$  value, where  $\chi^2$  is the judgment for goodness to find the  $B$  vertex.

### 3.4. THE MODIFIED $M_{BC}$

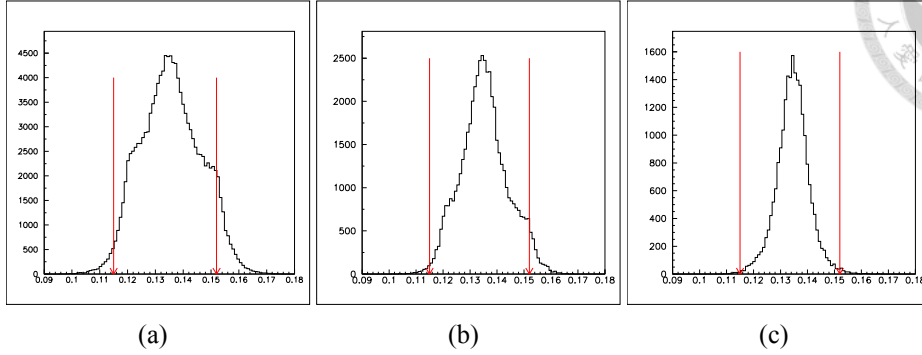


Figure 3.4: Invariant  $\pi^0$  mass distribution (a) in data sample (b) in signal MC without true event selection (c) in signal MC with true event selection.

## 3.4 The Modified $M_{bc}$

In Belle detector, the resolution of charged particles is better than photons, hence the correlation problem between  $\Delta E$  and the reconstructed  $B$  mass occurs.

Deb Mohapatra and Nakao-San provide the modified  $M_{bc}$  which is defined as:

$$M_{bc} = \sqrt{(E_{beam})^2 - (\vec{P}_{h1} + \vec{P}_{h2} + \frac{\vec{P}_{\eta}}{|\vec{P}_{\eta}|}) \times \sqrt{(E_{beam} - E_{h1} - E_{h2})^2 - M_{\eta}^2}} \quad (3.1)$$

Where  $E_{beam}$  is the beam energy,  $\vec{P}_{h1}$  and  $\vec{P}_{h2}$  are the momentum of hadrons,  $E_{h1}$  and  $E_{h2}$  are the energy of hadrons. In  $B^0 \rightarrow K \pi \eta$  case,  $h1$  and  $h2$  are  $K$  and  $\pi$ , in  $B^0 \rightarrow \pi \pi \eta$  case,  $h1$  and  $h2$  are both  $\pi$ 's.  $\vec{P}_{\eta}$  is the  $\eta$  momentum,  $M_{\eta}$  is the  $\eta$  mass.

And the typical  $M_{bc}$  is defined as:

$$M_{bc} = \sqrt{(E_{beam})^2 - (P_{recon})^2} \quad (3.2)$$

Where  $E_{beam}$  is the beam energy, and  $P_{recon}$  is the reconstructed momentum.

The modified  $M_{bc}$  is based on the idea that we use the beam constrained  $\eta$  energy, but not the reconstructed energy, so that we can avoid to use photon detector energy directly. The introduction of the modified  $M_{bc}$  reduces the correlation between  $\Delta E$  and  $M_{bc}$ , and lead us to use independent PDF's of  $\Delta E$  and  $M_{bc}$  to model the signal shape.

Fig.3.5 shows the comparison between typical  $M_{bc}$  and modified  $M_{bc}$  for  $\eta \rightarrow \gamma\gamma$  mode on  $\Delta E - M_{bc}$  scatter plot, and Fig.3.6 is for  $\eta \rightarrow \pi^+\pi^-\pi^0$  mode. Fig.3.7 shows the comparison between typical  $M_{bc}$  and modified  $M_{bc}$  by 1-D plot. Table. 3.5 shows the width values of typical  $M_{bc}$  and modified  $M_{bc}$  shape, fit by one Gaussian; the bottom of the table shows the correlation coefficients between  $\Delta E$  and  $M_{bc}$ . The resolution improvement is obvious in  $\eta \rightarrow \gamma\gamma$  modes; it also has slight improvement in  $\eta \rightarrow \pi^+\pi^-\pi^0$  modes but negligible; correlation is reduced a lot in  $\eta(\gamma\gamma)$  modes, but also negligible in  $\eta(\pi\pi\pi^0)$  modes. This is because  $\gamma$ 's from  $\eta(\gamma\gamma)$  have higher energy thus poorer detector resolution than that from  $\pi^0$  of  $\eta(\pi^+\pi^-\pi^0)$ , so the improvement of modified  $M_{bc}$  is more obvious for  $\eta(\gamma\gamma)$  modes.

In  $\eta(\pi^+\pi^-\pi^0)$  reconstruction, we also tried to correct the  $\pi^0$  momentum instead of correcting  $\eta$  momentum, the improvement is almost the same, even worse in  $\eta\pi^+\pi^-$  mode. So we just use the same modified  $M_{bc}$  definition for all modes.

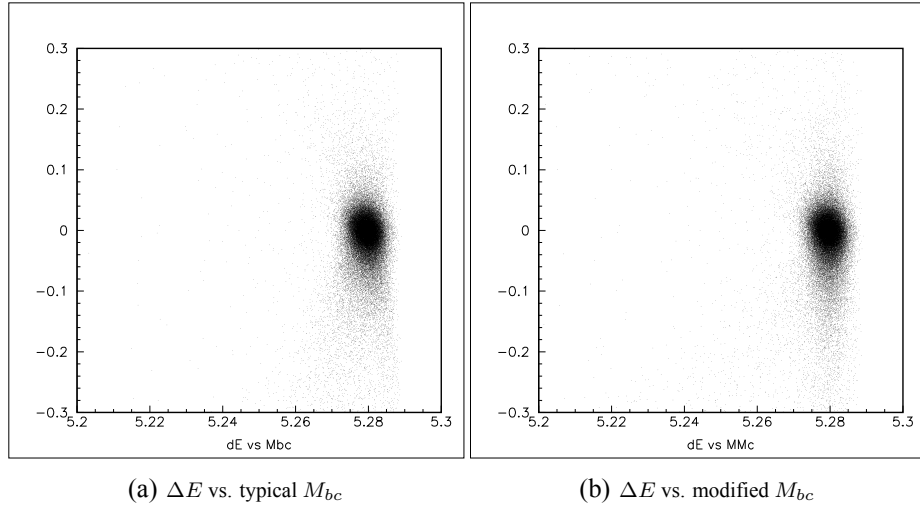


Figure 3.5:  $\Delta E$  and  $M_{bc}$  scatter plot in  $B \rightarrow K\pi\eta$ ,  $\eta \rightarrow \gamma\gamma$ .

### 3.5 Selections Summary

The energy difference  $\Delta E = E_{recon} - E_{beam}$  is calculated in the  $\Upsilon(4S)$  CM frame, where  $E_{recon}$  and  $E_{beam}$  are the reconstructed energy and beam energy. We use the modified  $M_{bc}$ (in section 3.4) definition for the reconstructed  $B$  mass. The

### 3.5. SELECTIONS SUMMARY

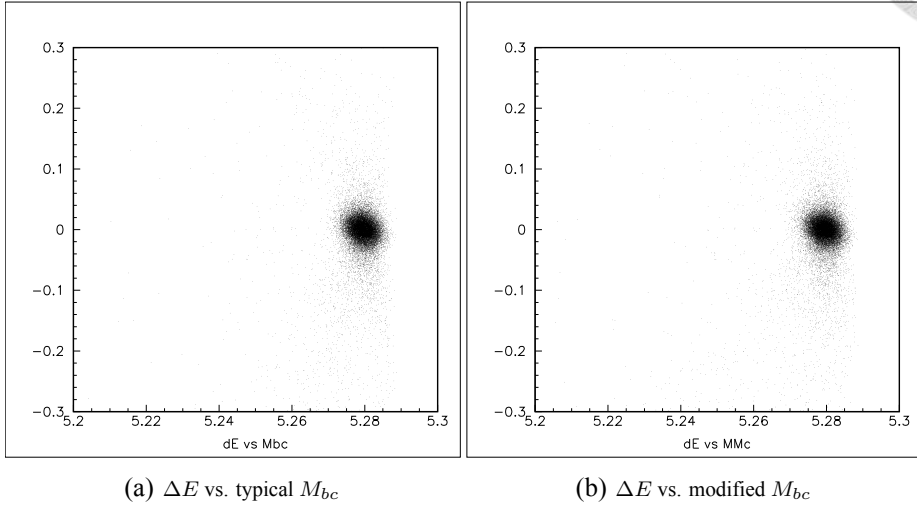


Figure 3.6:  $\Delta E$  and  $M_{bc}$  scatter plot in  $B \rightarrow K\pi\eta, \eta \rightarrow \pi^+\pi^-\pi^0$ .

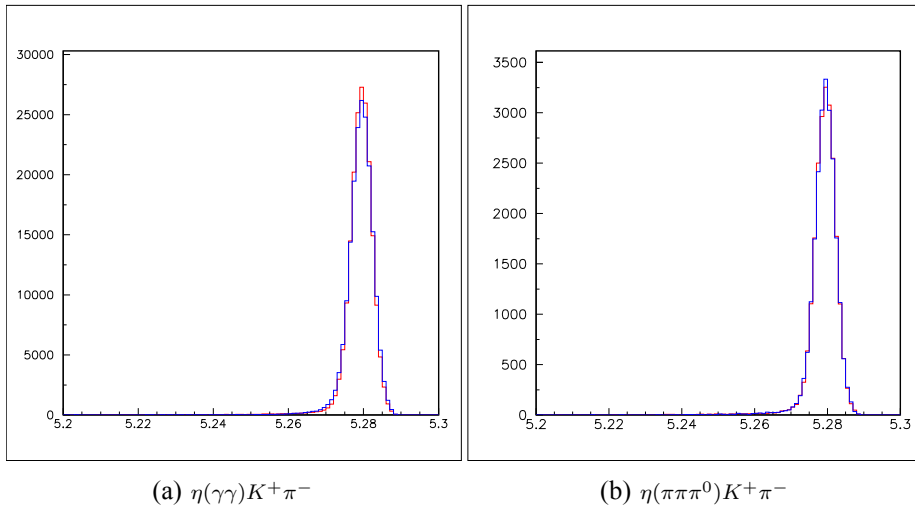


Figure 3.7: Modified  $M_{bc}$  and typical  $M_{bc}$ , the red line is modified  $M_{bc}$  and blue one is typical  $M_{bc}$ . Modified  $M_{bc}$  has better resolution.

Table 3.5: Width values of modified  $M_{bc}$  and typical  $M_{bc}$  ( $\text{MeV}/c^2$ ), and correlation coefficients ( $\times 10^{-2}$ ) between  $\Delta E$  and  $M_{bc}$  shown in the bottom of the table.

		$\eta(\gamma\gamma)K^+\pi^-$	$\eta(\pi\pi\pi^0)K^+\pi^-$
Width	Typical $M_{bc}$	$2.860 \pm 0.008$	$2.764 \pm 0.014$
	Modified $M_{bc}$	$2.726 \pm 0.008$	$2.756 \pm 0.014$
Correlation coefficient	Typical $M_{bc}$	-1.67	-10.9
	Modified $M_{bc}$	-0.951	-10.7

$\Delta E$  resolution of  $\eta \rightarrow \gamma\gamma$  is wider than that of  $\eta \rightarrow \pi^+\pi^-\pi^0$ . The  $\Delta E$  resolution also varies from lower  $\eta$  momentum region to higher region.

Events with  $M_{bc} > 5.2 \text{ GeV}/c^2$  and  $|\Delta E| < 0.3 \text{ GeV}$  are selected in sample box.

Table.3.6 shows the summary of selections.



Table 3.6: Summary of particle selection criteria.

Particle	Selection
$K, \pi$ from $B$	$\mathcal{L}_{K/\pi} > 0.6$ for $K^\pm$ $\mathcal{L}_{K/\pi} < 0.4$ for $\pi^\pm$ $eID < 0.95$ $\mu ID < 0.95$ $ \Delta r  < 0.3$ cm $ \Delta z  < 3.0$ cm
$\eta(\gamma\gamma)$	$E_\gamma > 50\text{MeV}$ in barrel region $E_\gamma > 100\text{MeV}$ in endcap region $\pi^0$ veto $ \cos\theta_{heli}(\eta)  < 0.9$ $500 < M_\eta < 575$ MeV/ $c^2$
$\eta(\pi^+\pi^-\pi^0)$	$\mathcal{L}_{K/\pi} < 0.4$ for $\pi^\pm$ $eID < 0.95$ for $\pi^\pm$ $\mu ID < 0.95$ for $\pi^\pm$ $ \Delta r  < 0.3$ cm for $\pi^\pm$ $ \Delta z  < 3.0$ cm for $\pi^\pm$ $0.115 < M_{\pi^0} < 0.152$ GeV/ $c^2$ $E_\gamma > 50\text{MeV}$ in barrel region $E_\gamma > 100\text{MeV}$ in endcap region $ \cos\theta_{heli}(\pi^0)  < 0.9$ $537.5 < M_\eta < 558.0$ MeV/ $c^2$







## Chapter 4

# Background Study

### 4.1 Overview of Backgrounds Study

Continuum background( $e^+e^- \rightarrow q\bar{q}$ ,  $q = u, d, s, c$ ), generic B background( $b \rightarrow c$  transition, include mixed and charged decay) and rare B background( $b \rightarrow u, d, s$  transition, include mixed and charged decay) are considered in this analysis.

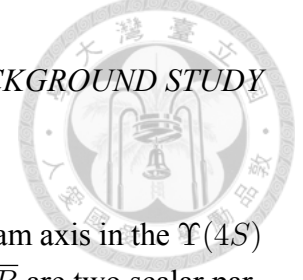
We study backgrounds with Monte Carlo(MC), all the MC and data are based on the new tracking algorithm(case B). 1 stream  $q\bar{q}$  MC, 2~6 times generic B MC and 50 times rare B MC are generated for different decay modes.

### 4.2 Continuum Background

Our dominant background comes from Continuum background decays, we can distinguish  $B\bar{B}$  spherical events from the more jet-like  $q\bar{q}$  events by the event shape variables.

#### 4.2.1 $\Delta Z$

$\Delta Z$  is the vertex difference between the B candidate and the accompanying B. Due to color confinement quarks can not isolate. In other words, the  $\Delta Z$  distribution of  $q\bar{q}$  events would be narrower than that of  $B\bar{B}$  events. Fig.4.2 shows the  $\Delta Z$  distribution for each mode.



### 4.2.2 $\cos\theta_B$

The  $\theta_B$  is the angle between B flight direction and the beam axis in the  $\Upsilon(4S)$  rest frame. Since  $\Upsilon(4S)$  is a vector particle (spin 1) while  $B\bar{B}$  are two scalar particles (spin 0), the angular distribution of  $\theta_B$  will be in the form:  $1 - \cos^2\theta_B$ , while the distribution of  $q\bar{q}$  is uniform. Fig.4.3 shows the  $\cos\theta_B$  distribution for each mode.

### 4.2.3 Kakuno Super Fox-Wolfram(KSFW)

KSFW is a useful method to separate signal from  $q\bar{q}$  events, it include 6 normalized Fox-Wolfram moments.

KSFW is defined as:

$$KSFW \equiv \sum_{l=0}^4 R_l^{so} + \sum_{l=0}^4 R_l^{oo} + \gamma \sum_{l=0}^{N_t} |P_{t,n}| \quad (4.1)$$

where the superscript  $s$  denotes the hadronic particle from the reconstructed  $B$  meson,  $o$  denotes which from other particles.  $P_t$  is transverse momentum, the sum of all momenta of particles (1 variable);  $N_t$  is the number of tracks in a event;  $\gamma$  is Fisher coefficient.

$R_l^{so}$  is defined as:

$$R_l^{so} \equiv \frac{\alpha_c (H_{charged})_l^{so} + \alpha_n (H_{neutral})_l^{so} + \alpha_m (H_{missing})_l^{so}}{E_{beam} - \Delta E} \quad (4.2)$$

We use  $H_c$ ,  $H_n$  and  $H_m$  to stand for  $H_{charged}$ ,  $H_{neutral}$  and  $H_{missing}$  respectively in later pages.

For  $l = 1, 3$  (2 variables)

$$(H_c)_l^{so} \equiv \beta_l^{so} \sum_i \sum_j Q_i Q_j |p_i| P_l(\cos\theta_{ij}) \quad (4.3)$$

and  $(H_n)_l^{so} = H_m = 0$

For  $l = 0, 2, 4$  (9 variables)

$$(H_{c,n,m})_l^{so} \equiv \beta_l^{so} \sum_i \sum_j |p_i| P_l(\cos\theta_{ij}) \quad (4.4)$$

## 4.2. CONTINUUM BACKGROUND

where  $i$  denotes the particle from  $B$  candidate,  $j$  iterates over the same category (charged, neutral, missing) tracks of others;  $Q_i, Q_j$  are the electrical charge of particle  $i$  and  $j$  respectively;  $P_l$  is the  $l$ -th Legendre polynomial.  $\theta_{ij}$  is the angle between particle  $i$  and  $j$ ;  $\alpha$  and  $\beta$  are Fisher coefficients.

$R_l^{oo}$  is defined as:

For  $l = 1, 3$  (2 variables)

$$R_l^{oo} = \frac{\beta_l^{oo} \sum_j \sum_{k(\neq j)} Q_j Q_k |p_j| |p_k| P_l(\cos\theta_{jk})}{(E_{beam} - \Delta E)^2} \quad (4.5)$$

For  $l = 0, 2, 4$  (3 variables)

$$R_l^{oo} = \frac{\beta_l^{oo} \sum_j \sum_{k(\neq j)} |p_j| |p_k| P_l(\cos\theta_{jk})}{(E_{beam} - \Delta E)^2} \quad (4.6)$$

The missing mass is defined as:

In the condition  $E_{\Upsilon(4S)} - \sum_{n=1}^{N_t} E_n > 0$

$$MM^2 = (E_{\Upsilon(4S)} - \sum_{n=1}^{N_t} E_n)^2 - (\sum_{n=1}^{N_t} \vec{p}_n)^2 \quad (4.7)$$

In the condition  $E_{\Upsilon(4S)} - \sum_{n=1}^{N_t} E_n < 0$

$$MM^2 = -((E_{\Upsilon(4S)} - \sum_{n=1}^{N_t} E_n)^2 - (\sum_{n=1}^{N_t} \vec{p}_n)^2) \quad (4.8)$$

where  $N_t$  is the total number of tracks in each event.  $E_n$  and  $\vec{p}_n$  are the energy and momentum of each track, respectively.

And we separate  $MM^2$  into 7 regions as following table:

Table 4.1: The  $MM^2$  regions of KSFV

Region	1	2	3	4	5	6	7
$MM^2(\text{GeV}/c^2)$	$<-0.5$	$-0.5 \sim 0.3$	$0.3 \sim 1.0$	$1.0 \sim 2.0$	$2.0 \sim 3.5$	$3.5 \sim 6.0$	$>6.0$



#### 4.2.4 Fisher Discriminant

The main idea of the Fisher discriminant is to combine  $n$ -dimensional KSFV variables into one dimension by a linearly weighted sum. We optimize the coefficients separately in 7 different  $MM^2$  regions. Table.4.2 shows Fisher distance for each  $MM^2$  bins, Fisher distance is the projected distance between Fisher discriminant distributions of signal and continuum events, which is maximized while minimizing the variance. Fig.4.1 shows the  $MM^2$  and Fisher discriminant distribution.

Table 4.2: The fisher distance for each  $MM^2$  region.

$MM^2$	0	1	2	3	4	5	6
$\eta(\gamma\gamma) K \pi$	2.10	2.48	2.40	2.15	2.07	1.86	1.59
$\eta(\pi^+\pi^-\pi^0) K \pi$	2.01	2.61	2.49	2.22	2.08	1.85	1.81

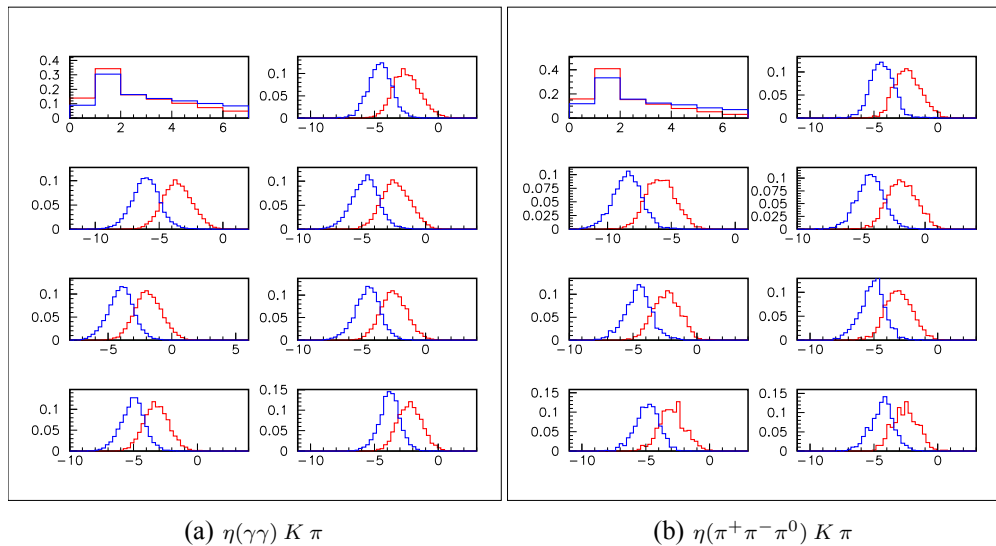


Figure 4.1: The distribution of  $MM^2$  and Fisher discriminant in each  $MM^2$  region. The red line stands for signal MC and the blue line stands for  $q\bar{q}$  MC.

## 4.2. CONTINUUM BACKGROUND

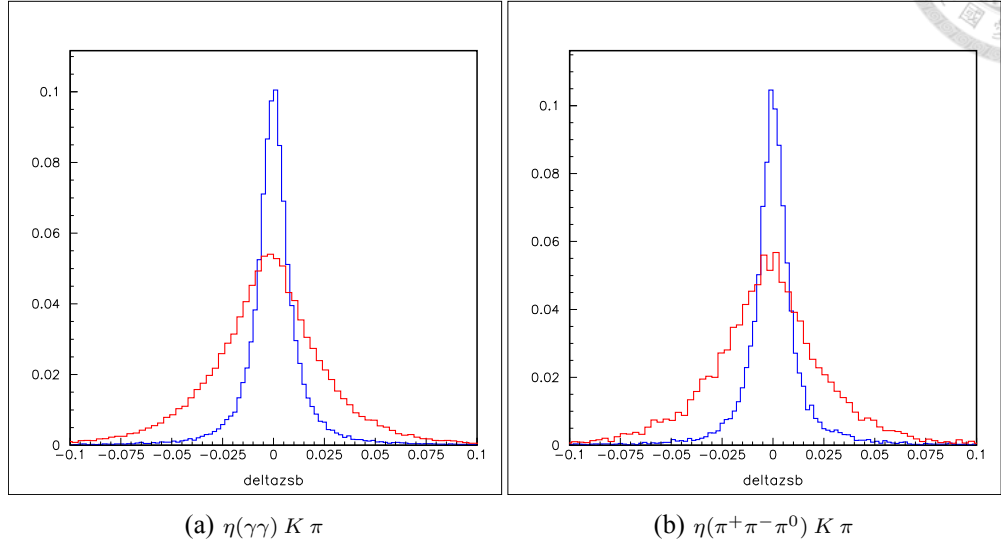


Figure 4.2:  $\Delta Z$  distribution for each mode. The red line stands for signal MC, and the blue line stands for  $q\bar{q}$  MC.

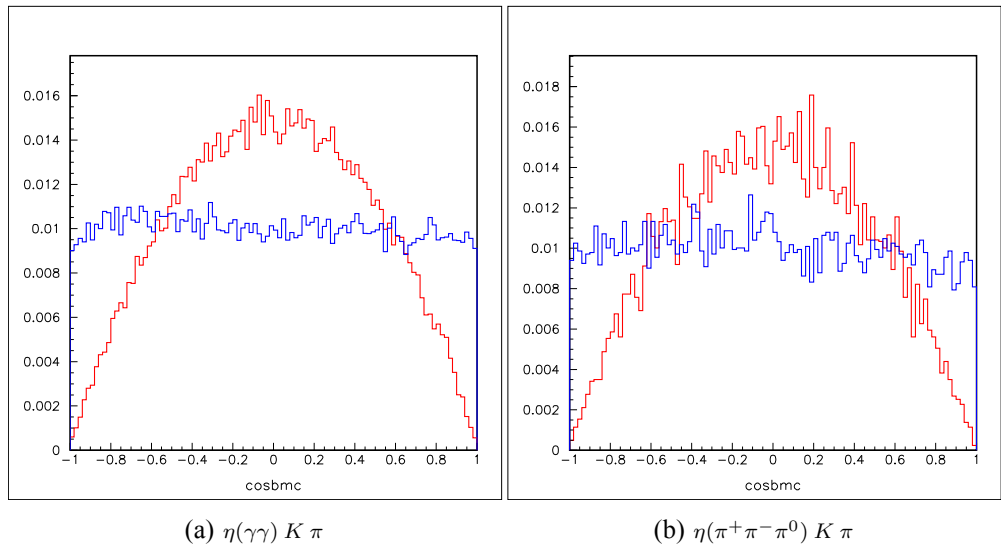


Figure 4.3:  $\cos\theta_B$  distribution for each mode. The red line stands for signal MC, and the blue line stands for  $q\bar{q}$  MC.



### 4.2.5 Likelihood Ratio(LR)

We combine KSFW,  $\Delta Z$  and  $\cos\theta_B$  probability density functions(PDFs) to determine likelihood ratio(LR). Likelihood is defined as:

$$L_{S(B)} = P(F) \times P(\Delta Z)_{S(B)} \times P(\cos\theta_B)_{S(B)} \quad (4.9)$$

where  $F$  denotes Fisher discriminator.  $S$  stands for signal,  $B$  stands for background. And LR is defined as:

$$LR = \frac{L_S}{L_S + L_B} \quad (4.10)$$

The normalized  $LR$  distribution of signal MC and continuum MC is shown in Fig.4.4.

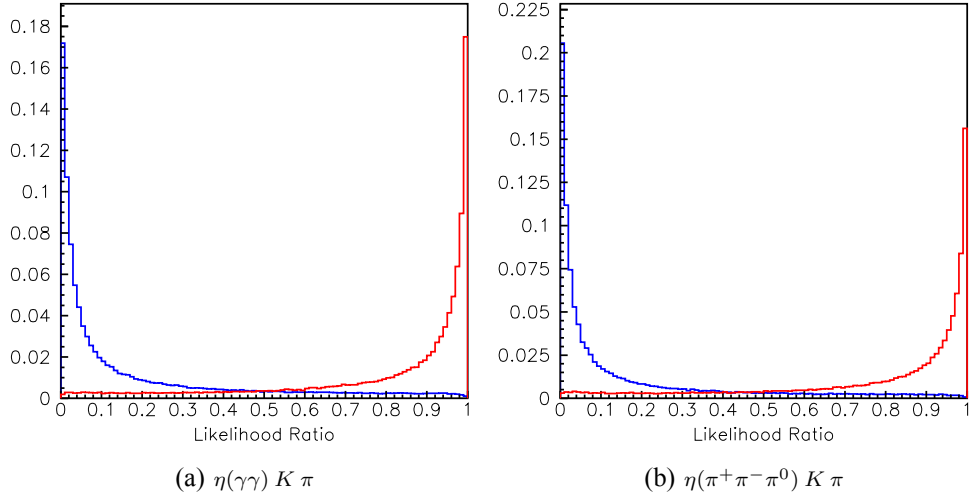


Figure 4.4:  $LR$  distribution for each mode. The red line stands for signal MC, and the blue line stands for  $q\bar{q}$  MC.

### 4.2.6 Optimization of LR cut

We also use another discriminator to judge if a particle like  $B$  meson or not. It is tagging information, " $q$ " and " $r$ ". The value of the preferred flavor  $q$ , equals +1 for particle  $B^0/B^+$ , -1 for anti-particle  $\bar{B}^0/B^-$ . The value of tagging quality factor  $r$  ranges from 0 to 1 for no flavor to definite flavor.

## 4.2. CONTINUUM BACKGROUND

For  $B \rightarrow \eta K \pi$  mode, we optimized the  $LR$  cut in six  $q \times q_B \times r$  bins, where  $q_B$  is the bottom flavor number of  $B$  candidate, in the analysis we use the electronic charge of daughter particle  $K^\pm$  from  $B$  candidate. The value of  $q \times q_B \times r$  is from -1 to +1, the bins are more narrow near -1 than near +1.

Maximizing the statistical significance, total Figure of Merit(F.O.M.), can help us to optimize  $LR$  cut. Total F.O.M is defined as:

$$F.O.M._{total} = \sum_{i=1}^n \frac{N_{S,i}}{\sqrt{N_{S,i} + N_{B,i}}} \quad (4.11)$$

where  $N_{S,i}$  and  $N_{B,i}$  are the expected signal and background yields in  $i$ -th  $q \times q_B \times r$  or  $|q \times r|$  bin. And  $N_S$  is calculated by

$$N_S = N_{B\bar{B}} \times BF_{PDG} \times \epsilon_{MC}$$

where  $N_{B\bar{B}}$  is the total  $B$  event in data,  $BF_{PDG}$  is the branching fraction in PDG, and  $\epsilon_{MC}$  is the efficiency in MC.

Fig.4.5 shows the  $q \times q_B \times r$  distribution. Table.4.3 shows the  $\mathcal{LR}$  cut in each ( $q \times q_B \times r$ ) bin after optimization.

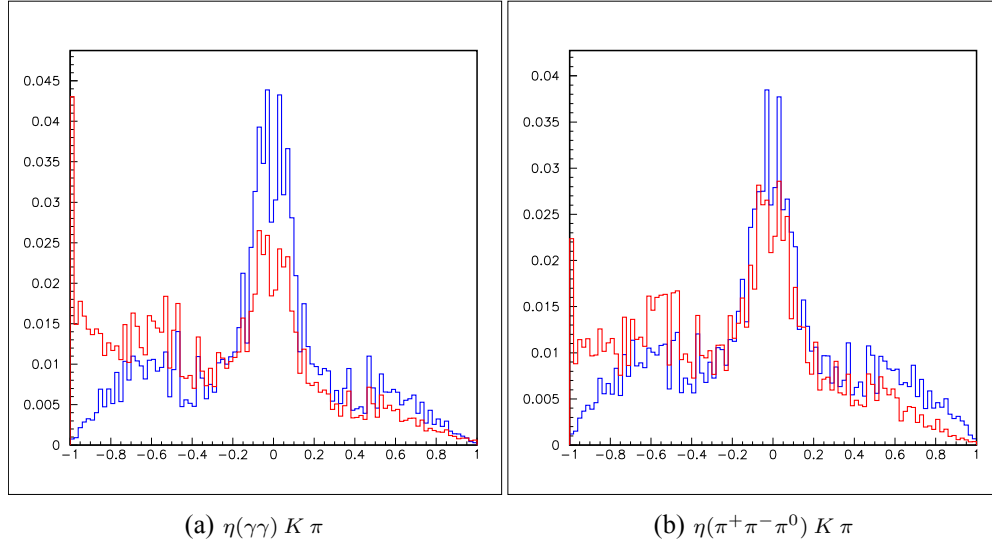
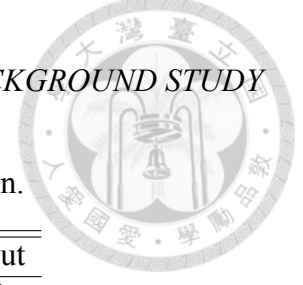


Figure 4.5:  $q \times q_B \times r$  distribution for  $B \rightarrow \eta K \pi$  mode. The red line stands for signal MC, and the blue line stands for  $q\bar{q}$  MC.



Table 4.3:  $\mathcal{LR}$  cut in each ( $q \times q_B \times r$ ) bin.

	$q \times q_B \times r$	$\mathcal{LR}$ cut
$\eta(\gamma\gamma) K \pi$	-1 $\sim$ -0.875	0.20
	-0.875 $\sim$ -0.75	0.85
	-0.75 $\sim$ -0.5	0.85
	-0.5 $\sim$ 0.0	0.90
	0.0 $\sim$ 0.5	0.90
	0.5 $\sim$ 1.0	0.80
$\eta(\pi^+\pi^-\pi^0) K \pi$	-1 $\sim$ -0.875	0.35
	-0.875 $\sim$ -0.75	0.95
	-0.75 $\sim$ -0.5	0.85
	-0.5 $\sim$ 0.0	0.95
	0.0 $\sim$ 0.5	0.95
	0.5 $\sim$ 1.0	0.85

### 4.3 Generic $B$ Background

Compare with  $q\bar{q}$  continuum events, generic B background is very few. Generic B decays are the  $B\bar{B}$  events with  $b \rightarrow c$  transition. The  $\Delta E$  and  $B_{bc}$  distributions in generic B MC are shown in Fig.4.6. There is no noticeable peaking contribution in  $\Delta E$  and  $M_{bc}$ .

In  $B^0 \rightarrow \eta(\gamma\gamma)K^+\pi^-$  study, 10 streams generic B MC are generated. The total events number after all selections is low but the distribution is quite different from other background, we still use the 10 streams sample to generate 2D smooth function.

### 4.4 Rare $B$ Background

Rare B background is another  $B\bar{B}$  background with  $b \rightarrow u, d, s$  transition, and also very few compared with  $q\bar{q}$  continuum events. The  $\Delta E$  and  $B_{bc}$  distributions in rare B MC are shown in Fig.4.7. Since signal is included in rare B MC, all signals have been removed from the plots.

We use rare B MC 2010 version generated by Jean Wicht, the size is 50 times of the 7-65 data.

#### 4.4. RARE B BACKGROUND

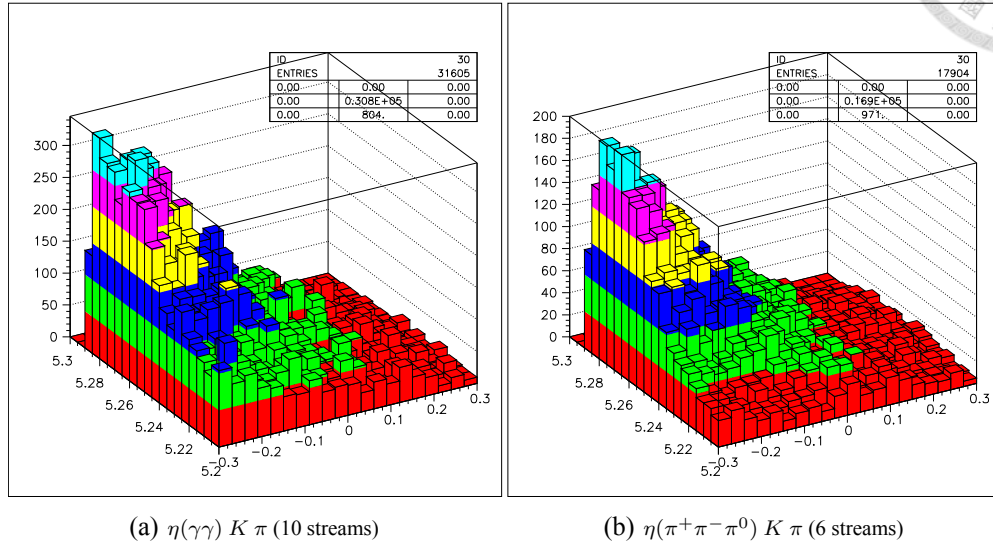
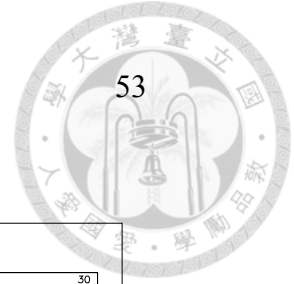


Figure 4.6: The 2D histogram lego plot of generic B background in MC.

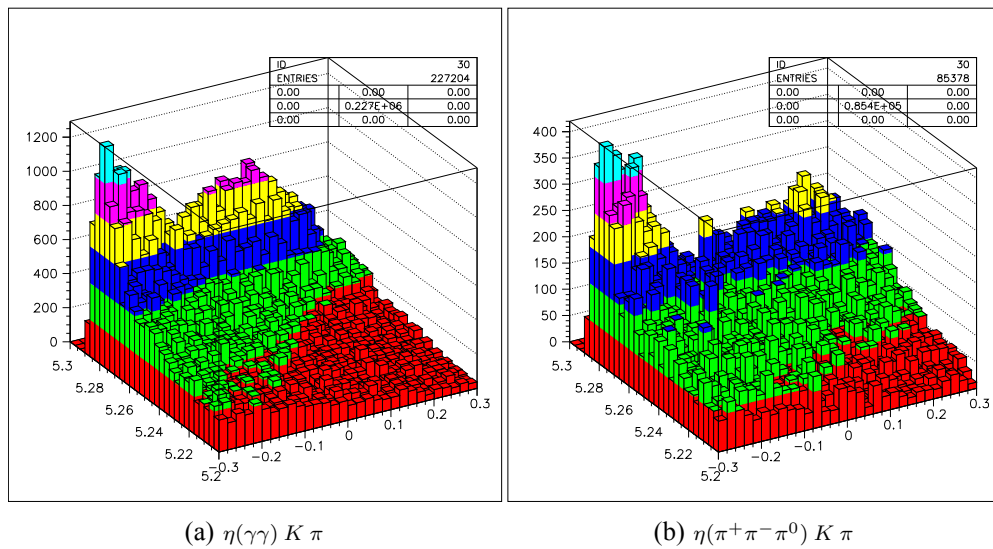
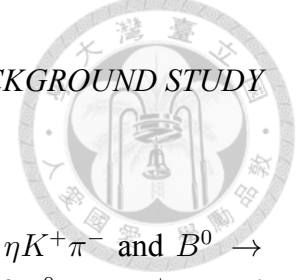


Figure 4.7: The 2D histogram lego plot of rare B background in MC. All are 50 times data.



## 4.5 Feedacross Background

Since the misidentification of  $K^\pm$  and  $\pi^\pm$ , the  $B^0 \rightarrow \eta K^+ \pi^-$  and  $B^0 \rightarrow \eta \pi^+ \pi^-$  feed across each other. We can do simultaneous fit of  $B^0 \rightarrow \eta K^+ \pi^-$  and  $B^0 \rightarrow \eta \pi^+ \pi^-$ . The event number of feedacross is constrained according to the KID efficiency and fake rate.

The number of feedacross of  $\eta \pi \pi$  mode fake to  $\eta K^\pm \pi^\mp$  is calculated by:

$$N_{(\eta K^\pm \pi^\mp)}^{fake} = \left[ \frac{N_{(\eta \pi \pi)fit}}{\epsilon_{(\eta \pi \pi)(\eta \pi \pi)} \times \epsilon_{\pi^+} \times \epsilon_{\pi^-}} \right] \times \epsilon_{(\eta \pi \pi)(\eta K \pi)} \times (\epsilon_{\pi^-} f_{K^+} + \epsilon_{\pi^+} f_{K^-}) \quad (4.12)$$

it is a remarkable fact that the first term in the right hand side is the total number of  $\eta \pi \pi$  events in real data.

$N_{(\eta K^\pm \pi^\mp)}^{fake}$ : the number of  $\eta \pi \pi$  events which fake to  $\eta K^\pm \pi^\mp$ .

$N_{(\eta \pi \pi)fit}$ : the fitting yield of  $\eta \pi \pi$  mode.

$\epsilon_{(\eta \pi \pi)(\eta \pi \pi)}$ : the  $\eta \pi \pi$  efficiency after applying  $\eta \pi \pi$  selection criteria.

$\epsilon_{(\eta \pi \pi)(\eta K \pi)}$ : the  $\eta \pi \pi$  efficiency after applying  $\eta K \pi$  selection criteria.

$\epsilon_{K^\pm}, \epsilon_{\pi^\pm}$ : the ratio of KID efficiency of  $\frac{Data}{MC}$ .

$f_{K^\pm}, f_{\pi^\pm}$ : the ratio of KID fake rate of  $\frac{Data}{MC}$ .

And the number of feedacross of  $\eta K \pi$  events fake to  $\eta \pi \pi$  is calculated by:

$$N_{(\eta \pi^\pm \pi^\mp)}^{fake} = N_{\eta K^+ \pi^-} \times \epsilon_{(\eta K \pi)(\eta \pi \pi)} \times \epsilon_{\pi^-} f_{\pi^+} + N_{\eta K^- \pi^+} \times \epsilon_{(\eta K \pi)(\eta \pi \pi)} \times \epsilon_{\pi^+} f_{\pi^-} \quad (4.13)$$

where  $N_{\eta K^\pm \pi^\mp}$  is the total number of  $\eta K^\pm \pi^\mp$  events in real data and is calculated by

$$N_{\eta K^\pm \pi^\mp} = \frac{N_{(\eta K \pi)fit}}{\epsilon_{(\eta K^\pm \pi^\mp)(\eta K \pi)} \times \epsilon_{K^\pm} \times \epsilon_{\pi^\mp}} \times \frac{1 \mp A_{CP, K \pi}}{2} \quad (4.14)$$

$N_{(\eta \pi^\pm \pi^\mp)}^{fake}$ : the number of  $\eta K^\pm \pi^\mp$  events which fake to  $\eta \pi^\pm \pi^\mp$ .

$N_{(\eta K \pi)fit}$ : the fitting yield of  $\eta K \pi$  mode.

$\epsilon_{(\eta K^\pm \pi^\mp)(\eta K \pi)}$ : the  $\eta K^\pm \pi^\mp$  efficiency after applying  $\eta K \pi$  selection criteria.

$\epsilon_{(\eta K \pi)(\eta \pi \pi)}$ : the  $\eta K \pi$  efficiency after applying  $\eta \pi \pi$  selection criteria.

$A_{CP}$ : the  $A_{CP}$  of  $\eta K \pi$  mode.

#### 4.5. FEEDACROSS BACKGROUND

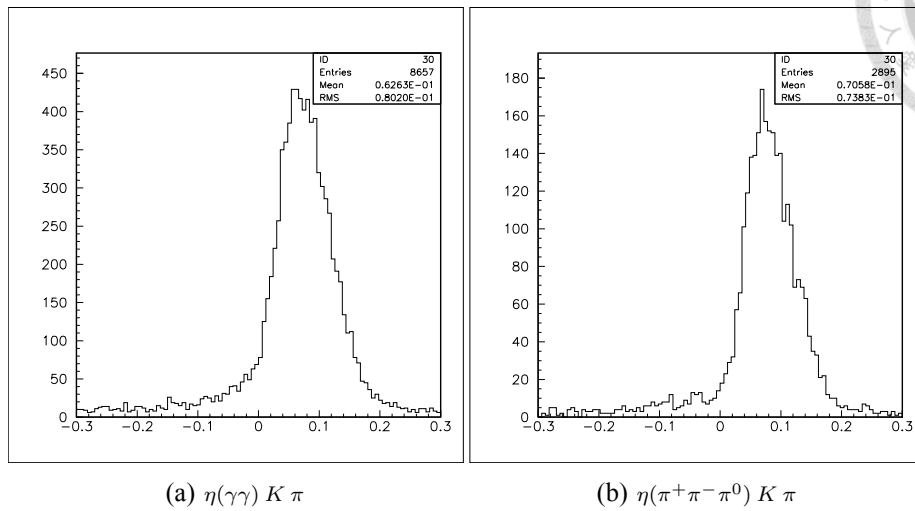
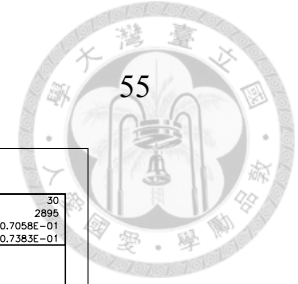


Figure 4.8: The  $\Delta E$  projection plot of feedacross from  $\eta\pi^+\pi^-$  in MC for  $\eta K^+\pi^-$  study.

Since the events number of feedacross is correlated closely with the total events, we will fit the data sample of  $\eta K^+\pi^-$  and  $\eta\pi^+\pi^-$  simultaneously, before the works of  $\eta\pi^+\pi^-$  is prepared, we would regard the feedacross from  $\eta\pi^+\pi^-$  as a neglect component in  $\eta K^+\pi^-$  data study.





# Chapter 5

## Control Sample Study

### 5.1 Introduction

We have two kinds of control samples, one for the calibration factor between real data and MC, another one for the check of  $\eta$  reconstruction method.

Since the  $\Delta E$ ,  $M_{bc}$  signal shapes are directly from MC, we have to investigate the difference between data and MC. The control samples for this purpose are:

- Inclusive  $B^0 \rightarrow K^+ \pi^- \pi^0$
- $B^0 \rightarrow D^-(K_S \pi) \rho^+$ , and  $K_S \rightarrow \pi^+ \pi^-$

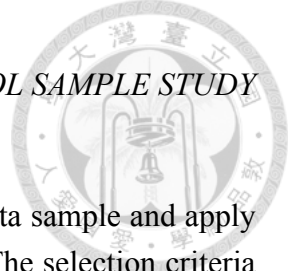
$B^0 \rightarrow K^+ \pi^- \pi^0$  is for the final state with 2 charged particles and 2 photons, and  $B^0 \rightarrow D^-(K_{S(\pi^+ \pi^-)} \pi) \rho^+$  is for the final state with 4 charged particles and 2 photons. We can use these control samples to get  $\Delta E$  and  $M_{bc}$  fudge factors, and get the error of fudge factors to give systematic error for  $\Delta E$  and  $M_{bc}$  signal shapes.

We choose the full case B data(Exp.7~65) as the data sample and apply a *very close* selection criteria as used in  $B^0 \rightarrow \eta K \pi$  study. The selection criteria for these two control samples are shown in Table.5.1 and Table.5.2.

And we check the  $\eta$  reconstruction method through following control samples:

- $B^+ \rightarrow \eta(\gamma\gamma) \pi^+$
- $B^+ \rightarrow \eta(\pi^+ \pi^- \pi^0) \pi^+$

The measurement result of branching fraction will be used to understand if the  $\eta$  selection criteria works well, and we can also get the error of all  $\eta$  selection



criteria

We also choose the full case B data(Exp.7~65) as the data sample and apply the *same*  $\eta$  selection criteria as used in  $B^0 \rightarrow \eta K \pi$  study. The selection criteria are shown in Table.5.3.

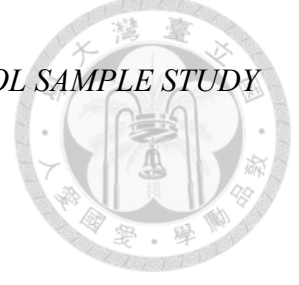
Table 5.1: Summary of  $B^0 \rightarrow K^+ \pi^- \pi^0$  selection criteria.

	Selection
$K, \pi$ from $B$	$\mathcal{L}_{K/\pi} > 0.6$ for $K^\pm$ $\mathcal{L}_{K/\pi} < 0.4$ for $\pi^\pm$ $eID < 0.95$ $\mu ID < 0.95$ $ \Delta r  < 0.3$ cm $ \Delta z  < 3.0$ cm
$\pi^0$	$E_\gamma > 50$ MeV in barrel region $E_\gamma > 100$ MeV in endcap region $0.115 < M_{\pi^0} < 0.152$ GeV/ $c^2$
$LR$ cut	$LR > 0.9$
Best candidate	Choose best $\pi^0$ event

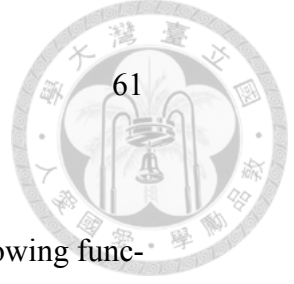
Table 5.2: Summary of  $B^0 \rightarrow D^-(K_{S(\pi^+\pi^-)}\pi)\rho^+$  selection criteria.

	Selection
$\pi^\pm$	$\mathcal{L}_{K/\pi} < 0.4$ $eID < 0.95$ $\mu ID < 0.95$ $ \Delta r  < 0.3 \text{ cm}$ $ \Delta z  < 3.0 \text{ cm}$
$K_S$	$ M_{K_s} - M_{K_s(PDG)}  < 0.04 \text{ GeV}/c^2$
$\rho^\pm$	$0.5 < M_{\rho^\pm} < 1.0 \text{ GeV}/c^2$
$\pi^0$	$E_\gamma > 50 \text{ MeV}$ in barrel region $E_\gamma > 100 \text{ MeV}$ in endcap region $0.115 < M_{\pi^0} < 0.152 \text{ GeV}/c^2$
$D^\pm$	$1.845 < M_{D^\pm} < 1.895 \text{ GeV}/c^2$
Best candidate	Choose best $\pi^0$ event
Fitting region	$ \Delta E  < 0.3$ $5.2 < M_{bc} < 5.3$



Table 5.3: Summary of  $B^+ \rightarrow \eta\pi^+$  selection criteria.

	Selection
$\pi^\pm$	$\mathcal{L}_{K/\pi} < 0.4$ $\mu ID < 0.9$ $ \Delta r  < 0.3 \text{ cm}$ $ \Delta z  < 3.0 \text{ cm}$
$\eta(\gamma\gamma)$	$E_\gamma > 50\text{MeV}$ in barrel region $E_\gamma > 100\text{MeV}$ in endcap region $ \cos\theta_{\text{heli}}(\eta)  < 0.9$ $\pi^0$ veto $500 < M_\eta < 575 \text{ MeV}/c^2$
$\eta(\pi^+\pi^-\pi^0)$	$E_\gamma > 50\text{MeV}$ in barrel region $E_\gamma > 100\text{MeV}$ in endcap region $\mathcal{L}_{K/\pi} < 0.6$ for $\pi^\pm$ $eID < 0.95$ for $\pi^\pm$ $\mu ID < 0.95$ for $\pi^\pm$ $ \Delta r  < 0.3 \text{ cm}$ for $\pi^\pm$ $ \Delta z  < 3.0 \text{ cm}$ for $\pi^\pm$ $0.115 < M_{\pi^0} < 0.152 \text{ GeV}/c^2$ $ \cos\theta_{\text{heli}}(\pi^0)  < 0.95$ $537.5 < M_\eta < 558.0 \text{ MeV}/c^2$
Best candidate	Choose best $\eta$ event
Fitting region	$ \Delta E  < 0.3$ $5.2 < M_{bc} < 5.3$
LR cut set	Optimization by maximizing F.O.M.



## 5.2. FITTING

### 5.2 Fitting

We use 2D-fit( $\Delta E$  and  $M_{bc}$ ) for each control sample, and use following functions for modeling signal and background shapes:

- In signal shape modeling, triple Gaussian for  $\Delta E$  and double Gaussian for  $M_{bc}$ .
- In continuum background shape modeling, Chebyshev polynomials of 2-order for  $\Delta E$  and Argus function for  $M_{bc}$ .
- In generic B and rare B background shape modeling, 2-D smooth function for both two.
- In self-cross feed(SXF) shape modeling, 2-D smooth function for this component.

Must be noted here, due to the  $\pi^0$  or  $\eta$  final state, we can just apply the same shape modelings to every control sample.

**In  $B^0 \rightarrow K^+\pi^-\pi^0$  and  $B^0 \rightarrow D^-(K_{S(\pi^+\pi^-)}\pi)\rho^+$  data fitting**, we float the number of signal, continuum, genericB and rareB background; also float the mean value and width of the first (dominant) Gaussian of signal shape, the mean value distance from any other Gaussian to dominant Gaussian is fixed, the ratio of width of any other Gaussian to dominant Gaussian is also fixed; and float the coefficients of Chebyshev function and effect value of Argus function, all other parameters are fixed; the ratio between signal and SXF yield is fixed.

**In  $B^+ \rightarrow \eta\pi^+$  data fitting**, all the floated and fixed values are similar to previous one, except that the generic B background component is combined with continuum background, and due to the little signal yield of this mode, we just use the same fudge factors between data and MC gotten by previous study(Belle note #1180) to fix the signal shape.

### 5.3 Calibration Factor Results

Fig.5.1 and Fig.5.3 show the signal shapes; Fig.5.2 and Fig.5.4 show the data fitting plots.

Table.5.4 and Table.5.6 show the fudge factors result after data fitting, the errors in the tables are statistical error.

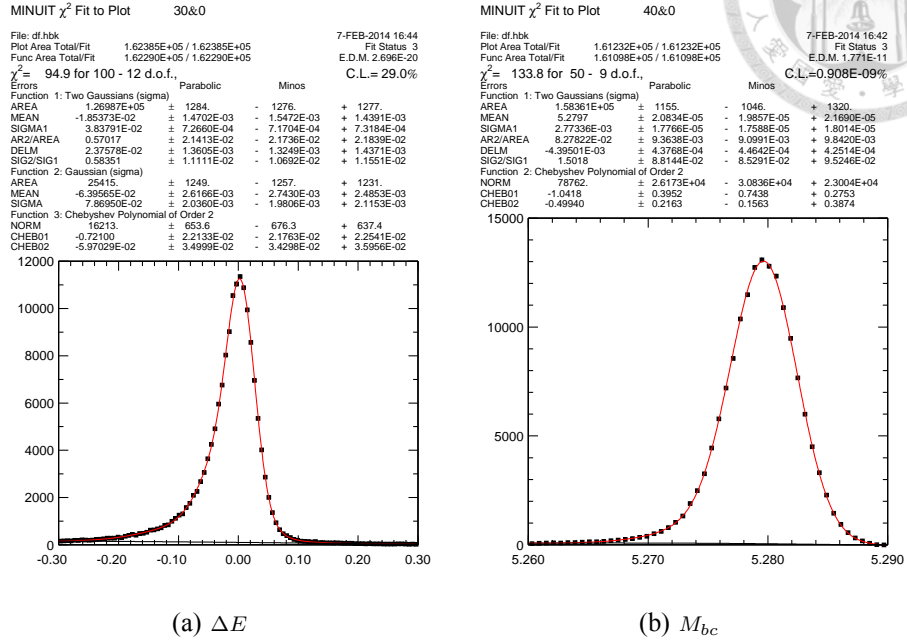


Figure 5.1: The  $\Delta E$ (top) and  $M_{bc}$ (bottom) projection plot in signal MC with true event selection of  $B^0 \rightarrow K\pi\pi^0$  mode.

Table 5.4: Fudge factors result of  $B^0 \rightarrow K\pi\pi^0$  between data and MC.

Width	Signal MC	Data	Ratio
$\Delta E(\text{MeV})$	$38.379 \pm 0.727$	$44.030 \pm 2.947$	$1.147 \pm 0.080$
$M_{bc}(\text{MeV}/c^2)$	$2.773 \pm 0.018$	$2.573 \pm 0.114$	$0.928 \pm 0.042$



5.3. CALIBRATION FACTOR RESULTS

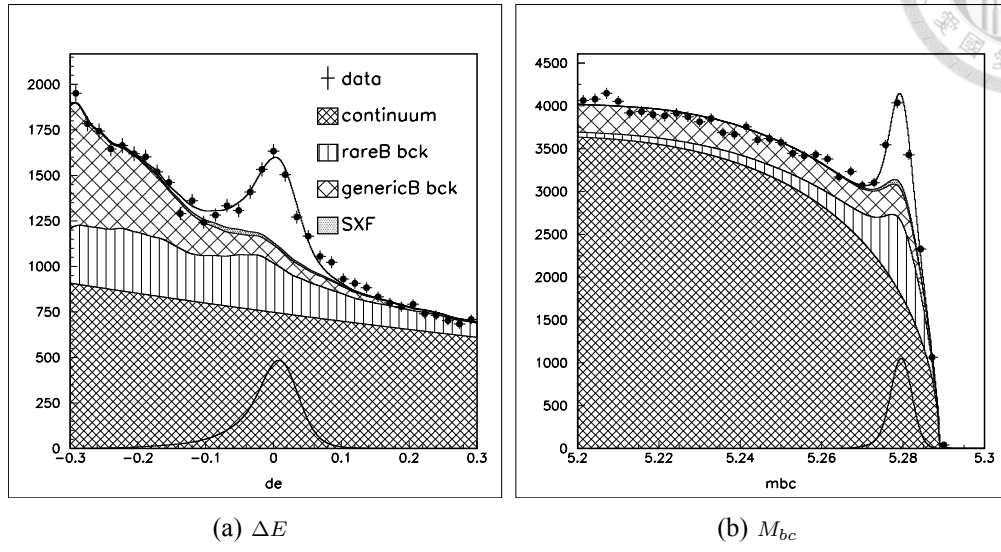


Figure 5.2: The  $\Delta E$ (left) and  $M_{bc}$ (right) projection plot of data fitting of  $B^0 \rightarrow K\pi\pi^0$  mode.

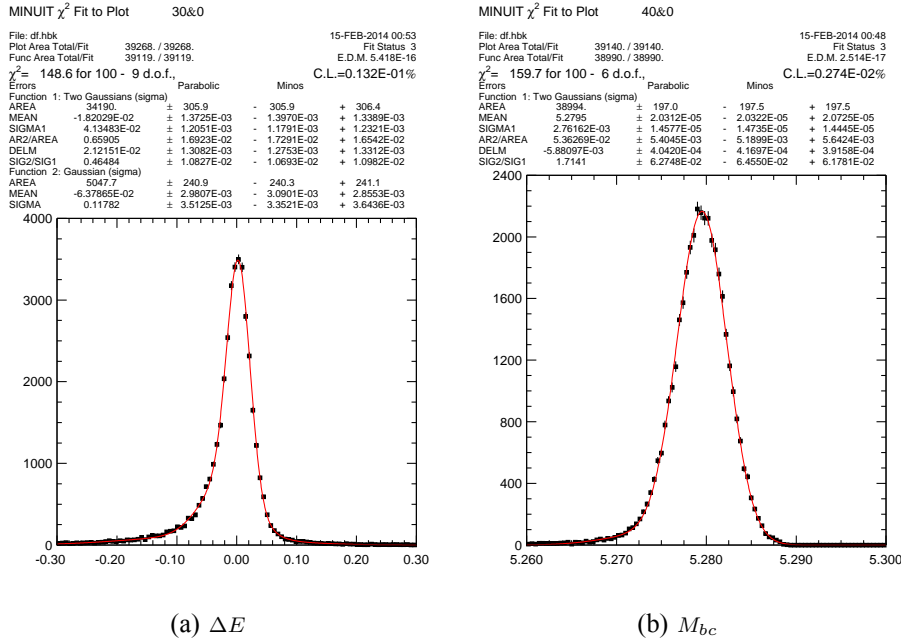


Figure 5.3: The  $\Delta E$  and  $M_{bc}$  projection plot in signal MC with true event selection of  $B^0 \rightarrow D^-(K_S(\pi^+\pi^-)\pi)\rho^+$  mode.

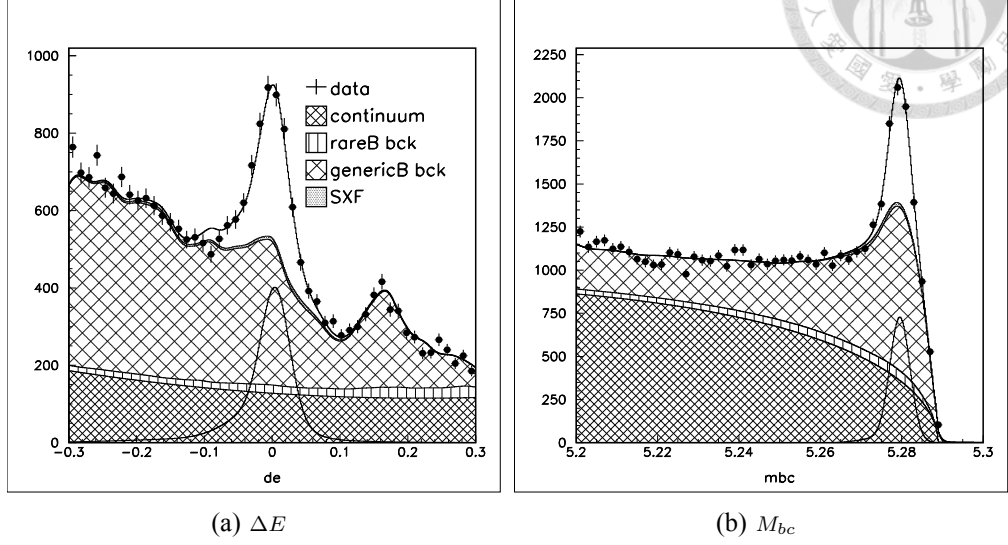


Figure 5.4: The  $\Delta E$  and  $M_{bc}$  projection plot of data fitting of  $B^0 \rightarrow D^-(K_{S(\pi^+\pi^-)}\pi)\rho^+$  mode.

Table 5.5: Mean value difference of  $B^0 \rightarrow K\pi\pi^0$  between data and MC.

Mean value	Signal MC	Data	Difference
$\Delta E(\text{MeV})$	$-18.537 \pm 1.470$	$-12.651 \pm 1.714$	$5.886 \pm 2.258$
$M_{bc}(\text{MeV}/c^2)$	$5279.700 \pm 0.021$	$5279.618 \pm 0.128$	$-0.08 \pm 0.130$

Table 5.6: Fudge factors result of  $D^-(K_{S(\pi^+\pi^-)}\pi)\rho^+$  between data and MC.

Width	Signal MC	Data	Ratio
$\Delta E(\text{MeV})$	$41.348 \pm 1.205$	$44.256 \pm 2.249$	$1.070 \pm 0.063$
$M_{bc}(\text{MeV}/c^2)$	$2.762 \pm 0.015$	$2.456 \pm 0.098$	$0.889 \pm 0.036$

Table 5.7: Mean value difference of  $D^-(K_{S(\pi^+\pi^-)}\pi)\rho^+$  between data and MC.

Mean value	Signal MC	Data	Difference
$\Delta E(\text{MeV})$	$-18.203 \pm 1.373$	$-16.359 \pm 1.165$	$1.844 \pm 1.801$
$M_{bc}(\text{MeV}/c^2)$	$5279.500 \pm 0.20$	$5279.567 \pm 0.107$	$0.067 \pm 0.227$



#### 5.4. $\eta$ SELECTION CHECK

### 5.4 $\eta$ Selection Check

This control sample,  $B^+ \rightarrow \eta\pi^+$ , is a cross check to the  $\eta$  reconstruction method. After getting the signal yields, we use the KID correction values gotten by previous study(Belle note #1180) and apply it on this mode, the data sample is the same to the previous study.

Fig.5.5 and Fig.5.7 show the signal shapes; Fig.5.6 and Fig.5.8 show the data fitting plots.

The branching fractions results and other details are shown in Table.5.8, the errors in the table are statistical error. Since 2D-fit is used in this study while 3d-fit is used in previous study, our statistical errors are slightly larger than previous results.

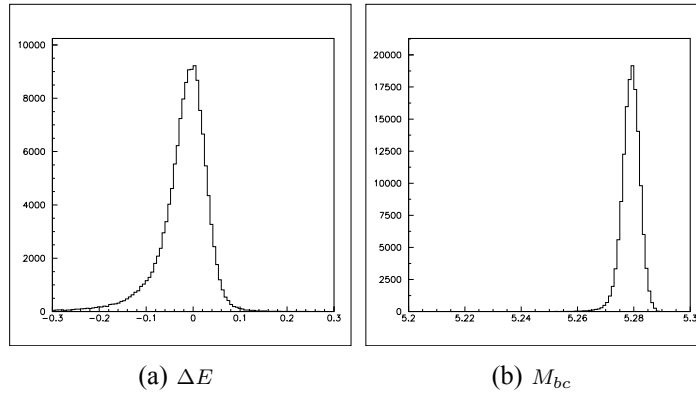


Figure 5.5: The  $\Delta E$  and  $M_{bc}$  projection plot in signal MC with true event selection of  $B^+ \rightarrow \eta(\gamma\gamma)\pi^+$  mode.

Table 5.8: Summary table of branching fractions and other details for each mode.

Mode	Yield	$\epsilon_{eff}(\%)$	KID correction	BF( $10^{-6}$ )	BF( $10^{-6}$ ) (previous study)
$B^+ \rightarrow \eta(\gamma\gamma)\pi^+$	$218 \pm 18$	17.75	0.9594	$4.22^{+0.35}_{-0.34}$	$4.24^{+0.31}_{-0.32}$
$B^+ \rightarrow \eta(\pi\pi\pi^0)\pi^+$	$53 \pm 10$	8.98	0.9101	$3.72 \pm 0.72$	$3.69 \pm 0.49$

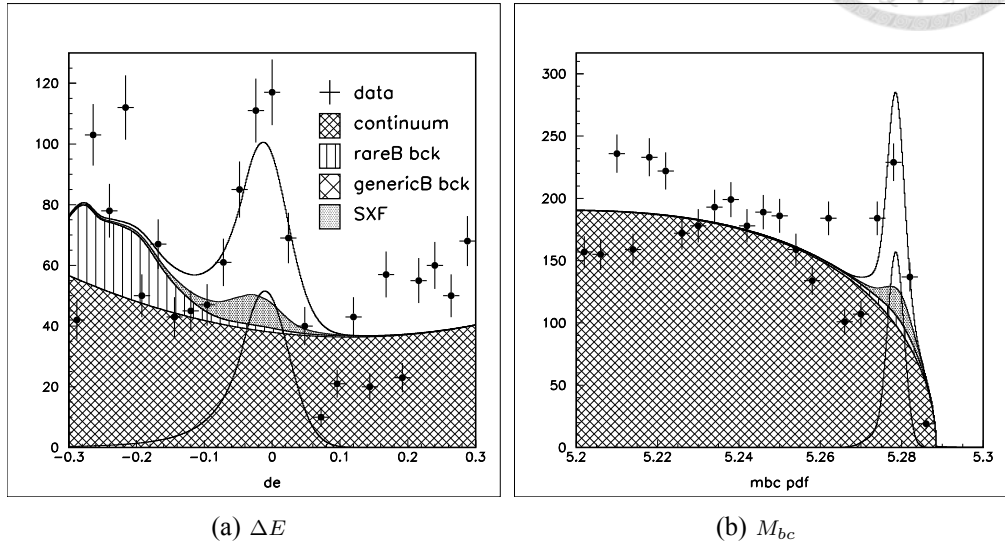
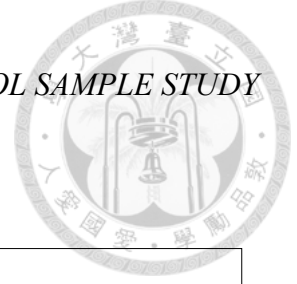


Figure 5.6: The  $\Delta E$  and  $M_{bc}$  projection plot of data fitting of  $B^+ \rightarrow \eta(\gamma\gamma)\pi^+$  mode.

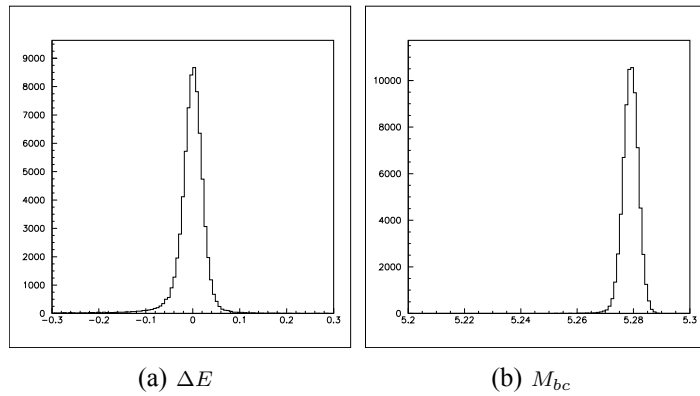


Figure 5.7: The  $\Delta E$  and  $M_{bc}$  projection plot in signal MC with true event selection of  $B^+ \rightarrow \eta(\pi^+\pi^-\pi^0)\pi^+$  mode.

5.4.  $\eta$  SELECTION CHECK

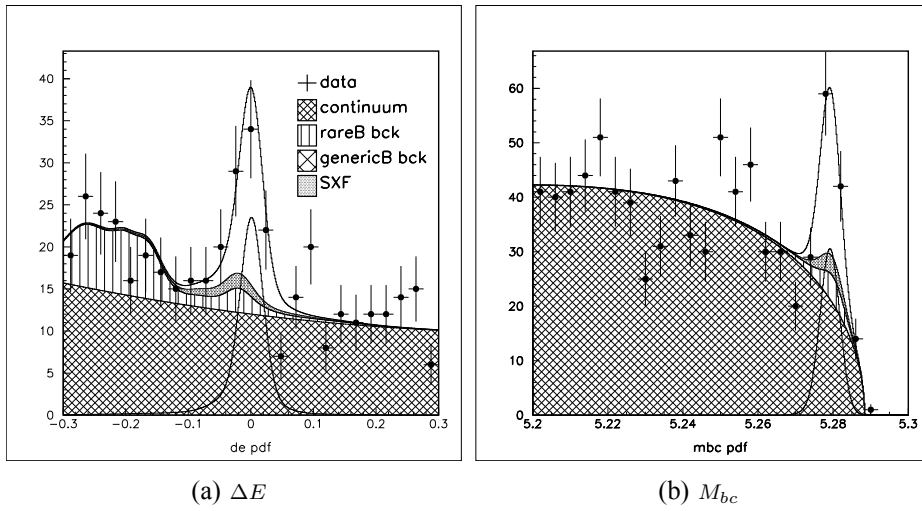


Figure 5.8: The  $\Delta E$  and  $M_{bc}$  projection plot of data fitting of  $B^+ \rightarrow \eta(\pi^+\pi^-\pi^0)\pi^+$  mode.







## Chapter 6

# Amplitude Analysis on Dalitz Plot

### 6.1 Introduction

The Dalitz plot is a scatter plot of  $M_{K^+\pi^-}$  versus  $M_{\eta\pi^-}$  in this study.  $M_{K^+\pi^-}$  is the invariant mass of  $K^+$  and  $\pi^-$ , while  $M_{\eta\pi^-}$  is the same, in four-momentum calculation we replace the energy of  $\eta$  by:

$$E_\eta = E_{beam} - E_{K^+} - E_{\pi^-} \quad (6.1)$$

but not the energy directly from detector, thus to reduce the serious smearing by energy of  $\eta$ ; where  $E_{beam}$  is beam energy.

In the study  $B^0(\overline{B}^0)$  decaying with the final state  $\eta K^\pm \pi^\mp$ , we consider following intermediate states:  $K^*(892)^0 \eta$ ,  $K_0^*(1430)^0 \eta$ ,  $K_2^*(1430)^0 \eta$ ,  $a_0(980)^\pm K^\mp$ ,  $a_0(1450)^\pm K^\mp$ ,  $a_2(1320)^\mp K^\pm$ .

The following selections are applied to veto  $D^\pm$  and  $D^0$  separately:

$$\begin{aligned} |M_{\pi\eta} - M_{D^\pm}| &> 0.07 \text{GeV}/c^2 \\ |M_{K\pi} - M_{D^0}| &> 0.03 \text{GeV}/c^2 \end{aligned} \quad (6.2)$$

### 6.2 Three-Body Signal Yields

We get total signal yield and number of events of each background component by performing  $\Delta E - M_{bc}$  distribution fit.

Fig.6.1 shows signal box and sideband region. Due to the two photons in final state,  $\Delta E$  distribution of signal has a long tail in  $\Delta E < 0$  region, thus the two  $\Delta E$  boundaries of signal box and sideband have different distance from  $\Delta E = 0$ .

We define signal box with the  $\Delta E - M_{bc}$  conditions in Table.6.1.

Table 6.1: Signal box region for each decay mode.

$B^0 \rightarrow \eta(\gamma\gamma)K^+\pi^-$	$-0.12 < \Delta E < 0.08$
	$5.27 < M_{bc} < 5.29$
$B^0 \rightarrow \eta(\pi^+\pi^-\pi^0)K^+\pi^-$	$-0.08 < \Delta E < 0.08$
	$5.27 < M_{bc} < 5.29$

We generate 1,000,000 signal MC events for  $B^0$  and  $\overline{B}^0$  decay modes separately, after applying all selection requirements, the number of events in signal box and efficiencies are shown in Table.6.2. Self-cross-feed(SXF) is also a component in fitting, we get the ratio between the number of SXF and signal events in signal MC and fix it in fitting, Table.6.3 shows the details.

Table 6.2: Number of events of pure three-body signal final state and corresponding efficiency for different decay modes in signal MC. All selection requirements are applied.

	Modes	$B^0$	$\overline{B}^0$
Number of events	$\eta(\gamma\gamma)K^+\pi^-$	128410	127748
	$\eta(\pi^+\pi^-\pi^0)K^+\pi^-$	51820	51743
Efficiency(%) after all cuts	$\eta(\gamma\gamma)K^+\pi^-$	12.841	12.775
	$\eta(\pi^+\pi^-\pi^0)K^+\pi^-$	5.182	5.174

## 6.2. THREE-BODY SIGNAL YIELDS



Table 6.3: Number of events and ratio between self-cross-feed and signal in signal MC after applying all selection requirements in entire  $\Delta E - M_{bc}$  signal yield fitting region. The ratio values are fixed in  $\Delta E - M_{bc}$  signal yield fitting.

	Modes	$B^0$	$\bar{B}^0$
$N_{SXF}/N_{SIG}$	$\eta(\gamma\gamma)K^+\pi^-$	31392/128410	31800/127748
	$\eta(\pi^+\pi^-\pi^0)K^+\pi^-$	14380/51820	14306/51743
Ratio(%)	$\eta(\gamma\gamma)K^+\pi^-$	24.447	24.892
	$\eta(\pi^+\pi^-\pi^0)K^+\pi^-$	28.042	27.648

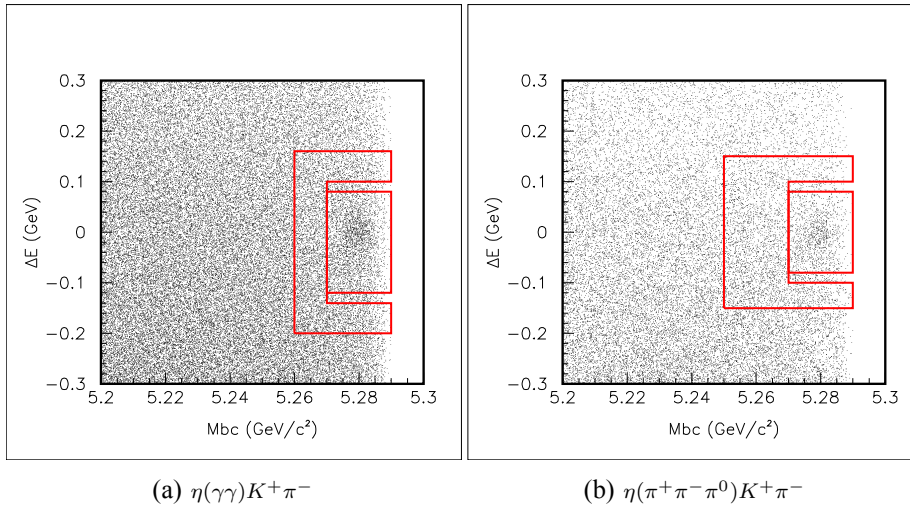
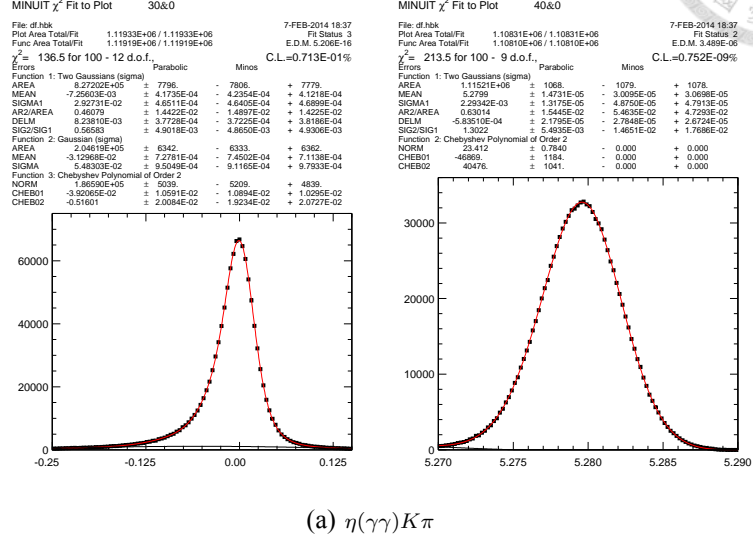
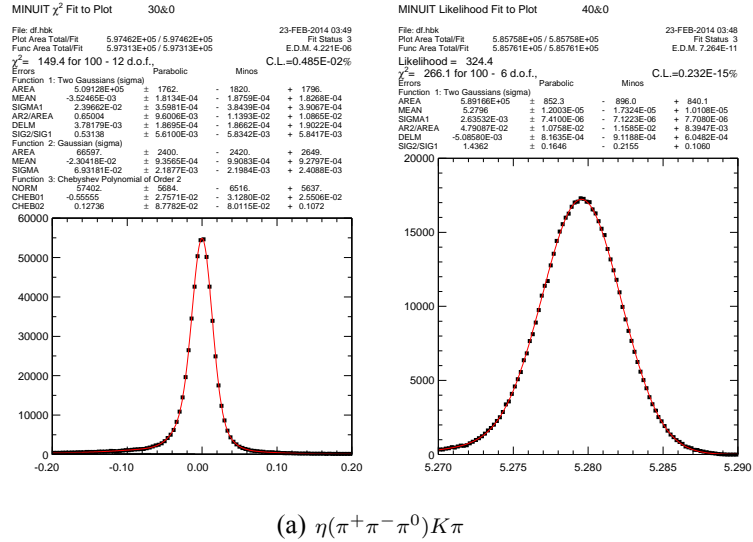
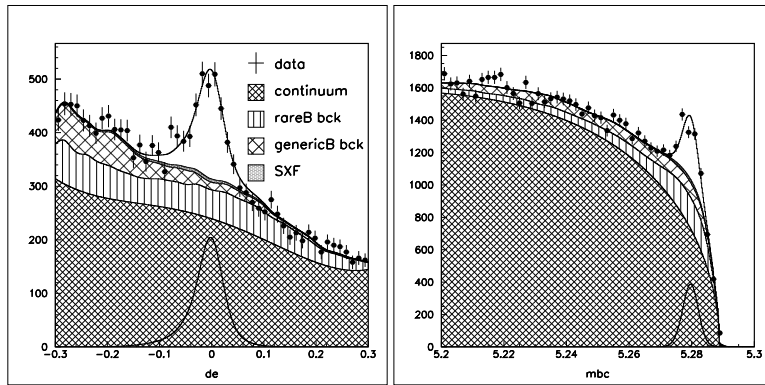
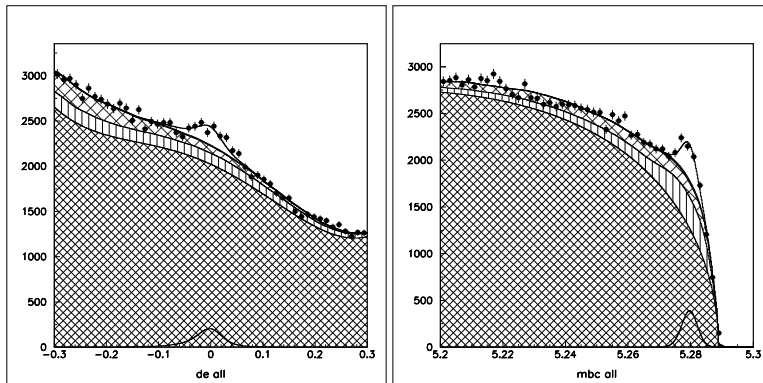


Figure 6.1: Signal box(rectangular region) and sideband(enclosing region) on  $\Delta E - M_{bc}$  scatter plot in data sample for each decay mode.

Figure 6.2: Signal shape of  $\Delta E$ (left) and  $M_{bc}$ (right) in signal MC for  $\eta(\gamma\gamma)K\pi$ .Figure 6.3: Signal shape of  $\Delta E$ (left) and  $M_{bc}$ (right) in signal MC for  $\eta(\pi^+\pi^-\pi^0)K\pi$ .

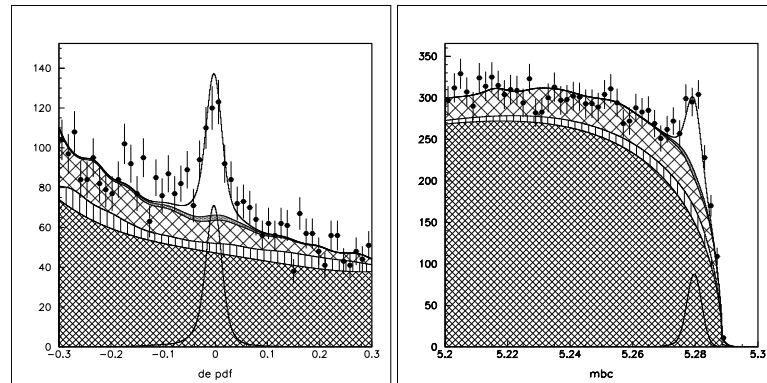
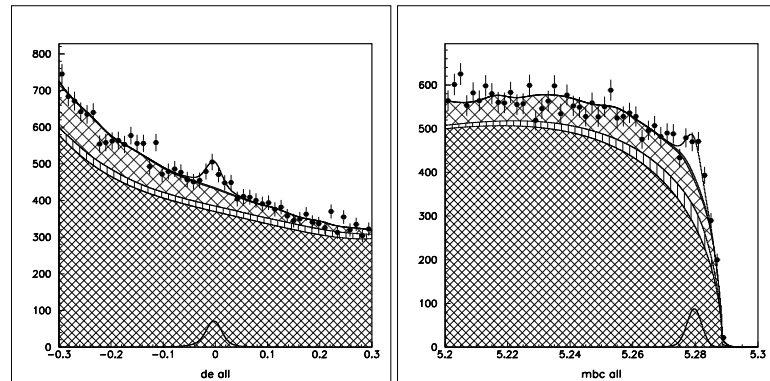


(a)  $\eta(\gamma\gamma)K\pi$  in signal box.



(b)  $\eta(\gamma\gamma)K\pi$  in entire  $\Delta E - M_{bc}$  fit region.

Figure 6.4: The  $\Delta E$ (left) and  $M_{bc}$ (right) projection plot of data fitting for  $\eta(\gamma\gamma)K\pi$ .

(a)  $\eta(\pi^+\pi^-\pi^0)K\pi$  in signal box.(b)  $\eta(\pi^+\pi^-\pi^0)K\pi$  in entire  $\Delta E - M_{bc}$  fit region.Figure 6.5: The  $\Delta E$ (left) and  $M_{bc}$ (right) projection plot of data fitting for  $\eta(\pi^+\pi^-\pi^0)K\pi$ .



### 6.3. SIGNAL AMPLITUDE FORMALISM

## 6.3 Signal Amplitude Formalism

In  $B^0 \rightarrow \eta K^+ \pi^-$  study, we model  $(K\pi)^*$  S-wave by two parametrization, Breit-Weigner function and LASS parametrization. See LASS parametrization in section.6.3.1.

For three-body decays of a spin-0 particle to all pseudo-scalar final states, the density of signal events on Dalitz plot can be described by:

$$d\Gamma = \frac{|\mathcal{M}|^2}{(2\pi)^3 32M^3} dm_{12}^2 dm_{23}^2 \quad (6.3)$$

where  $M$  is the invariant mass of decaying particle, in this study, it's  $B$  meson.  $\mathcal{M}$  is Lorentz-invariant matrix element.

The intermediate decay channels will cause non-uniform distributions on Dalitz plot. Resonance amplitude would interfere the nearby other resonance(include phase space decay), it's a good way to measure both magnitude of a decay and relative phases of intermediate states.

For this study,  $B^0(\overline{B^0})$  is spin-zero particle, so are the three daughter particles,  $\eta K^\pm \pi^\mp$ , there are only two degrees of freedom thus we describe the kinematics on Dalitz plot by  $m_{K\pi}^2$  and  $m_{\pi\eta}^2$ .  $m_{ij}$  is the invariant mass of particles  $i$  and  $j$ ,  $m_{ij}^2$  is the squared invariant mass, we use  $s_{12}$  to stand for  $m_{K\pi}^2$  and  $s_{23}$  for  $m_{\pi\eta}^2$  in the later pages.

We can get a constraint by energy and momentum conservation:

$$M_B^2 + m_1^2 + m_2^2 + m_3^2 = s_{12} + s_{23} + s_{31} \quad (6.4)$$

where  $m_i$  is the mass of daughter particle,  $M_B$  is  $B$  mass.

We can describe the amplitude for three-body  $B$  decay via the intermediate resonance  $r$  by:

$$\mathcal{A}_{r(J)} = F_B F_r B W_r T_r \quad (6.5)$$

where  $F$  are form factors, we use Blatt-Weisskopf barrier factor shown in Table. 6.4 for  $F_r$ . We set all meson radius  $d$  of intermediate resonances to be  $1.5 \text{ GeV}^{-1}$ .  $F_B$  is parametrized in a single pole approximation [42]:





$$F_B = \frac{1}{1 - \frac{m_{ij}^2}{M_{pole}^2}} \quad (6.6)$$

where we use the mass of  $B^*$  as a pole mass  $M_{pole}$  [43].

$BW_r$  in Eq.(6.5) is Breit-Weigner function given by:

$$BW_r(m_{ij}) = \frac{1}{m_r^2 - m_{ij}^2 - im_r\Gamma_{ij}(q)} \quad (6.7)$$

where  $m_r$  is the nominal mass of resonance, and  $\Gamma_{ij}$  is the "mass-dependent" width given by:

$$\Gamma_{ij}(q) = \Gamma_r \left(\frac{q}{q_0}\right)^{2J+1} \left(\frac{m_r}{m_{ij}}\right) F_r^2 \quad (6.8)$$

where  $q$  is the momentum of either daughter particle in the resonance candidate frame with the resonance mass equals to  $m_{ij}$ ,  $q_0$  is the momentum of either daughter particle in the resonance frame, calculated with the resonance mass equals to the nominal mass of resonance.  $J$  is the spin of resonance,  $\Gamma_r$  is the natural width of resonance  $r$ .

$T_r$  in Eq.(6.5) is angular distribution and it's different in following three case:

(1) Spin ( $J$ ) = 0

The spin of resonance  $r$  is zero, namely,  $r$  is a scalar state.

$$T_J = T_0 \equiv 1 \quad (6.9)$$

(2) Spin ( $J$ ) = 1

The spin of resonance  $r$  is one, namely,  $r$  is a vector state.

$$T_J = T_1(ijk|r_{ij}) = s_{ik} - s_{jk} + \frac{(M_B^2 - m_k^2)(m_j^2 - m_i^2)}{s_{ij}} \quad (6.10)$$

(3) Spin ( $J$ ) = 2

The spin of resonance  $r$  is two, namely,  $r$  is a tensor state.

$$T_J = T_2(ijk|r_{ij}) = (s_{ik} - s_{jk} + \frac{(M_B^2 - m_k^2)(m_j^2 - m_i^2)}{s_{ij}})^2 - \frac{1}{3}(s_{ij} - 2M_B^2 - 2m_k^2 + \frac{(M_B^2 - m_k^2)}{s_{ij}})(s_{ij} - 2m_i^2 - 2m_j^2 + \frac{(m_i^2 - m_j^2)}{s_{ij}}) \quad (6.11)$$

### 6.3. SIGNAL AMPLITUDE FORMALISM

"Non-resonant" amplitude is often described by a complex constant in  $D$  decay case, but the available phase space of  $B$  decay is much larger than that of  $D$  decay. In  $B \rightarrow \eta K \pi$  case, We describe it by a empirical parametrization:

$$\mathcal{A}_{nr} = a_{nr} e^{i\phi_{nr}} \quad (6.12)$$

where  $a_{nr}$  and  $\phi_{nr}$  are fit parameters.

So the complete description of signal amplitude is given by:

$$\mathcal{M} = \mathcal{A}_{total} = \sum_j a_j e^{i\delta_j} \mathcal{A}_{r,j} + \mathcal{A}_{nr} \quad (6.13)$$

where  $j$  stand for intermediate state,  $a_j$  is amplitude,  $\delta_j$  is relative phase. The fraction  $f_k$  of  $k$ -th component (can be non-resonant component) is calculated by:

$$f_k = \frac{\int |a_k \mathcal{A}^k|^2 ds_{12} ds_{23}}{\int |\mathcal{A}_{total}|^2 ds_{12} ds_{23}} \quad (6.14)$$

It must be noted that, the sum of the fractions for all component is not necessary to be unitary.

Table 6.4: Blatt-Weisskopf barrier factors.  $q_0$  is the momentum of either daughter particle in the resonance frame.  $q$  is the momentum of either daughter particle in the resonance candidate frame.  $d$  is impact parameter (resonance radius). Form factors are normalized to give  $F_r = 1$  for  $q^2 d^2 = q_0^2 d^2$  when  $m_{ab} = m_r$ .

Spin J	Form factor
0	1
1	$\sqrt{\frac{1+q_0^2 d^2}{1+q^2 d^2}}$
2	$\sqrt{\frac{(q_0^2 d^2 - 3)^2 + 9q_0^2 d^2}{(q^2 d^2 - 3)^2 + 9q^2 d^2}}$

#### 6.3.1 LASS Parametrization

We can also describe  $K_0^*(1430)$  resonance together with a effective range non-resonant component by LASS parametrization in  $K \pi$  spectrum, the effective range non-resonant component is cut off at  $1.6 \sim 1.8 \text{ GeV}/c^2$ .



$$R_0(m_{K\pi}) = \frac{m_{K\pi}}{q \cot \delta_B - iq} + e^{2i\delta_B} \frac{m_r \Gamma_0 \frac{m_r}{q_0}}{m_r^2 - m_{K\pi}^2 - im_r \Gamma_0 \frac{q}{m_{K\pi}} \frac{m_r}{q_0}} \quad (6.15)$$

where the first term is the non-resonant component and the second term is Breit-Wigner function with the relative phase  $2\delta_B$ ;  $m_{K\pi}$  is the  $(K^+\pi^-)$  invariant mass;  $\delta_B$  can be represented by cotangent form:

$$\cot \delta_B = \frac{1}{aq} + \frac{bq}{2} \quad (6.16)$$

where  $q$  is the momentum of either daughter particle in the resonance candidate frame;  $a$  is the scattering length and  $b$  is the effective range.

## 6.4 Efficiency over Dalitz Plot and Smearing

Reconstruction efficiency in general is not uniform over Dalitz plot, so that the original signal distribution on Dalitz plot can be distorted. We also consider the efficiency correction correspond to the momentum of charged kaons and pions. Fig.6.6 shows the efficiency distribution over Dalitz plot after PID correction. The efficiencies of top corner corresponding to low  $\eta$  energy in  $\eta(\pi^+\pi^-\pi^0)K^+\pi^-$  are obviously low, it's due to the photons,  $\pi^0$ 's and  $\eta$ 's selection.

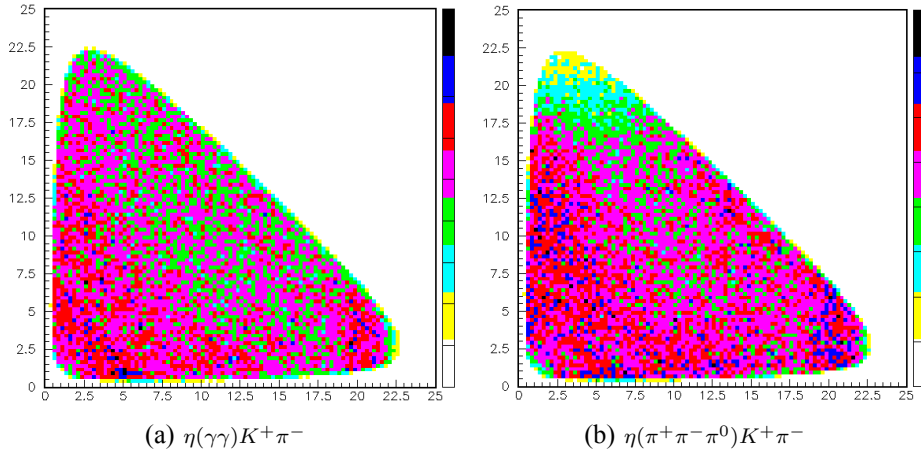


Figure 6.6: Reconstruction efficiency distribution over Dalitz plot.

It's important to describe the efficiency distribution over Dalitz plot. On the other hand, the number of events of sideband background is comparable to that

of signal in this study. Detector resolution can produce smearing of Dalitz plot boundaries, we use energy-momentum conservation to confine the allowable area (see section 6.6). Smearing also has effect on signal shape, but we neglect it since the intermediate states in general have large width compared with smearing effect.

We write the event density,  $P(s_{12}, s_{23}; \xi)$ , as:

$$P(s_{12}, s_{23}; \xi) = \frac{N_s \epsilon(s_{12}, s_{23}) S(s_{12}, s_{23}; \xi) + n_b b(s_{12}, s_{23})}{N_s \int_{DP} \epsilon(s_{12}, s_{23}) S(s_{12}, s_{23}; \xi) ds_{12} ds_{23} + n_b} \quad (6.17)$$

where  $N_s$  is the initial number of signal events distributed over Dalitz plot according to the signal density function  $S(s_{12}, s_{23}; \xi)$ .  $\epsilon(s_{12}, s_{23})$  is the reconstruction efficiency and it's a function of the position over Dalitz plot.  $n_b$  is the expected number of the observed background events distributed with the density function  $b(s_{12}, s_{23})$ .  $\xi$  is vector of parameters from unbinned maximum likelihood fit. The integration is performed in the entire Dalitz plot.

And the expected number of observed signal events  $n_s$  can be written as:

$$n_s = N_s \epsilon(s_{12}, s_{23}) = N_s \int_{DP} \epsilon(s_{12}, s_{23}) S(s_{12}, s_{23}; \xi) ds_{12} ds_{23} \quad (6.18)$$

The background density function can be written as:

$$B(s_{12}, s_{23}) = \frac{\epsilon_b b(s_{12}, s_{23})}{\epsilon(s_{12}, s_{23})} \quad (6.19)$$

So that we can write Eq.(6.17) into a function in terms of  $n_s$ :

$$P(s_{12}, s_{23}; \xi) = \epsilon(s_{12}, s_{23}) \frac{n_s S(s_{12}, s_{23}; \xi) / \epsilon_s + n_b B(s_{12}, s_{23}) / \epsilon_b}{n_s + n_b} \quad (6.20)$$

$\epsilon_s$  and  $\epsilon_b$  are overall signal and background efficiency gotten from MC:

$$\epsilon_s = \int \epsilon(s_{12}, s_{23}) S(s_{12}, s_{23}; \xi) ds_{12} ds_{23} = \frac{\Delta}{N_{gen}} \sum_{MC} S(s_{12}, s_{23}; \xi) \quad (6.21)$$

$$\epsilon_b = \int \epsilon(s_{12}, s_{23}) B(s_{12}, s_{23}) ds_{12} ds_{23} = \frac{\Delta}{N_{gen}} \sum_{MC} B(s_{12}, s_{23}) \quad (6.22)$$

The sum  $\sum_{MC}$  is performed from a set of MC events generated with a uniform distribution over the Dalitz plot, passed through detector simulation and all selection requirements.  $N_{gen}$  is the number of generated events.  $\Delta$  is Dalitz plot area.

The likelihood function to be minimized can be written as:

$$\begin{aligned} \mathcal{L} = & - \sum_{events} 2 \ln \left( F \frac{S(s_{12}, s_{23}; \xi)}{\sum_{MC} S(s_{12}, s_{23}; \xi)} + (1 - F) \frac{B(s_{12}, s_{23})}{\sum_{MC} B(s_{12}, s_{23}; \xi)} \right) \\ & - \sum_{events} 2 \ln \epsilon(s_{12}, s_{23}) + \frac{(F - F_0)^2}{\sigma_{F_0}^2} \end{aligned} \quad (6.23)$$

where  $S(s_{12}, s_{23}; \xi)$  and  $B(s_{12}, s_{23})$  are normalized to satisfy the requirements:

$$\int S(s_{12}, s_{23}; \xi) ds_{12} ds_{23} = 1 \quad (6.24)$$

and

$$\int B(s_{12}, s_{23}) ds_{12} ds_{23} = 1 \quad (6.25)$$

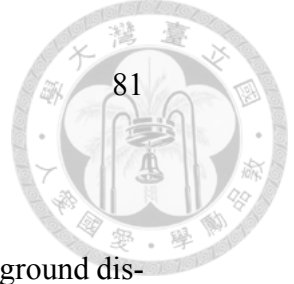
where  $F$  in Eq.(6.23) is the fraction of signal events in data sample, which is given by:

$$F = \frac{n_s}{n_s + n_b} \quad (6.26)$$

where  $F_0$  in Eq.(6.23) is the estimated fraction from  $\Delta E - M_{bc}$  distribution fit.

The 2nd term and 3rd term in Eq.(6.23) do not depend on vector of parameters  $\xi$ , they are constants in data fitting so that can be omitted in minimized likelihood calculation.

In practice, We generate a set of three-body phase space decay signal MC with large generated events number passing through detector simulation, divide entire Dalitz plot into  $100 \times 100$  bins and then count the number of events in each bin. Thus we get a efficiency function of position on Dalitz plot directly. In data fit, we use signal amplitude formalism (introduced in section 6.3) multiplied with efficiency function to describe signal distribution on Dalitz plot in data sample.



## 6.5 Sideband Background Modeling

For charmless three-body decays, it's important to understand background distribution since the number of background events is in general comparable to that of signal events.

The definition of  $\Delta E - M_{bc}$  sideband region is shown in Fig.6.1.

Fig.6.7 shows the distribution of sideband data on Dalitz plot.

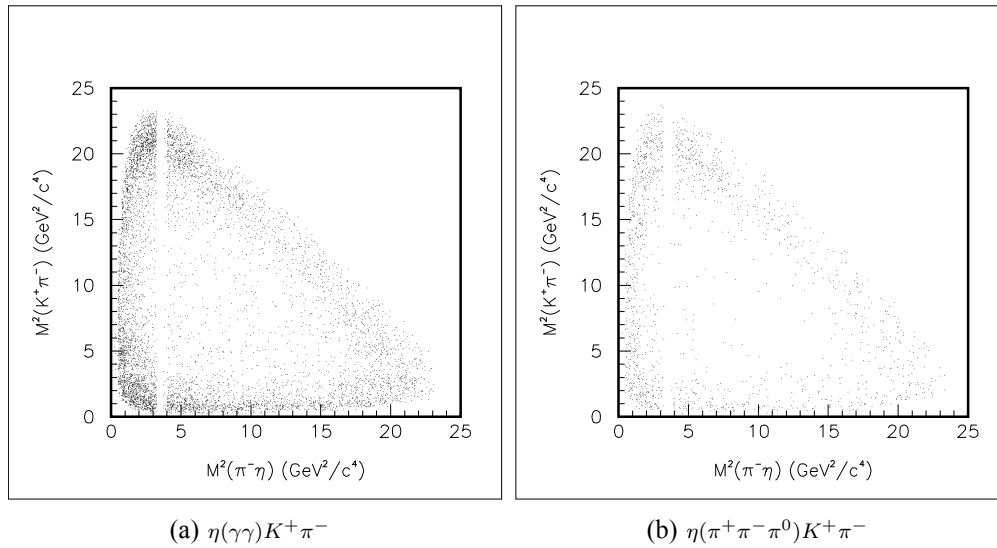


Figure 6.7: Dalitz plot in sideband region after all selection requirements in data sample.

We compared two method to know which is better for giving description of sideband background:

### (1) Parametrization

This method is a description of sideband background by a set of fit parameters, if we can find theoretical or empirical functions (or both) to model the background, it's easy to manipulate the fitting process.

We use the following basic parametrization to describe the distribution of sideband background events over Dalitz plot for  $\eta K^+\pi^-$  final states:



$$\begin{aligned}
B_{\eta K^+\pi^-}(s_{12}, s_{23}) = & \alpha_1 e^{-\beta_1 s_{12}} + \alpha_2 e^{-\beta_2 s_{23}} + \alpha_3 e^{-\beta_3 s_{13}} \\
& + \alpha_4 e^{-\beta_4 s_{12} - \beta_5 s_{23}} + \alpha_5 e^{-\beta_6 s_{23} - \beta_7 s_{13}} + \alpha_6 e^{-\beta_8 s_{12} - \beta_9 s_{13}} \\
& + \alpha_7 |BW_{scalar}(K^*(892))|^2 \\
& + \alpha_8 |BW_{scalar}(a_0(980))|^2
\end{aligned} \tag{6.27}$$

where  $\alpha$  and  $\beta$  are fit parameters, for convenience, we set  $\alpha_1$  to be 1.

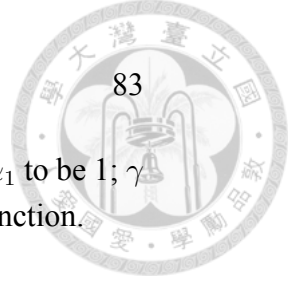
$BW_{scalar}(K^*(892))$  and  $BW_{scalar}(a_0(980))$  are uniform distribution of  $K^*(892)$  and  $a_0(980)$  over Dalitz plot, the masses and widths are fixed at PDG average values. Fig.C.1 shows the fit result of parametrization. We use the goodness-of-fit defined by Eq.(6.32) and Eq.(6.33) (more details in section 6.7) to know the quality of fit, but here, it also offer a way to give comparison between parametrization and smooth fn. modeling.

The fit result is good over entire Dalitz plot except high  $M_{K^+\pi^-}$  and  $M_{\pi^-\eta}$  region. Even though lots of function types had been tried to match the data distribution in the regions, we still could not find some suitable function types. Thus 2D smooth function modeling was developed to give a better description in this study.

## (2) Parametrization + 2D smooth function

Pure parametrization has pool performance in the large  $M_{K^+\pi^-}$  and  $M_{\pi^-\eta}$ , thus we use 2D smooth function to model this region with the condition:  $M_{K^+\pi^-}^2 > 3.5$  and  $M_{\pi^-\eta}^2 > 3.5 \text{ GeV}/c^2$ , while we still use parametrization for other regions for a better uniform resonance distribution modeling. Therefore the distribution on Dalitz plot of this method can be described as:

$$\begin{aligned}
B_{\eta K^+\pi^-}(s_{12}, s_{23}) = & \alpha_1 e^{-\beta_1 s_{12}} + \alpha_2 e^{-\beta_2 s_{23}} + \alpha_3 e^{-\beta_3 s_{13}} \\
& + \alpha_4 e^{-\beta_4 s_{12} - \beta_5 s_{23}} + \alpha_5 e^{-\beta_6 s_{23} - \beta_7 s_{13}} + \alpha_6 e^{-\beta_8 s_{12} - \beta_9 s_{13}} \\
& + \alpha_7 |BW_{scalar}(K^*(892))|^2 \\
& + \alpha_8 |BW_{scalar}(a_0(980))|^2 \\
& + \gamma \times \text{2D smooth function}(s_{12}, s_{23})
\end{aligned} \tag{6.28}$$



## 6.6. DALITZ PLOT BOUNDARY

where  $\alpha$ ,  $\beta$  and  $\gamma$  are fit parameters, for convenience, we also set  $\alpha_1$  to be 1;  $\gamma$  is a scale factor between parametrization and generated 2D smooth function.

Fig.C.2 - Fig.C.5 show the fit results.

We compare these two modeling method by  $\chi^2$ , Table.6.5 shows that.  $N_{bins}$  is number of bins in  $\chi^2$  calculation,  $N_{para.}$  is number of fit parameters. We can see that performance of combined method modeling is better than pure parametrization.

Table 6.5:  $\chi^2$  comparison of parametrization and combined method modeling.  $(\chi^2)_1$  is defined as Eq.(6.32),  $(\chi^2)_2$  is defined as Eq.(6.33).

	Parametrization	Parametrization + 2D-smooth-fn.
	$\eta(\gamma\gamma)K^+\pi^-$	
$(\chi^2)_1$	218	216
$(\chi^2)_2$	337	290
$N_{bins}$	191	191
$N_{para.}$	16	17
	$\eta(\pi^+\pi^-\pi^0)K^+\pi^-$	
$(\chi^2)_1$	79	16
$(\chi^2)_2$	142	64
$N_{bins}$	66	66
$N_{para.}$	16	17

Even though we have had these two modeling method, it's still a big problem to describe the background in signal box on Dalitz plot. We find that the background in signal box is always different from any sideband region choice, so we just check that parametrization is suitable to model sideband distribution, and then float some parameters in data fitting.

## 6.6 Dalitz Plot Boundary

The detector resolution produces smearing of the Dalitz plot boundaries, so that the phase space for the reconstructed B candidates exceeds the kinematically allowed area. Three-body combinations are kinematically fit to the nominal B mass to correct for this effect. Confining the boundaries let the fit easier because





we can neglect the different boundaries between signal and background.

We have the following conditions:

$$\begin{aligned} s_{12} &= M_B^2 + m_3^2 - 2M_B E_3 \\ s_{23} &= M_B^2 + m_1^2 - 2M_B E_1 \end{aligned} \quad (6.29)$$

where  $E_i$  is the energy of  $i$ -th daughter particle.

We can use two variables  $s_{12}$  and  $s_{23}$  to describe Dalitz plot, but it's more convenient by working with  $E_1$  and  $E_3$  to find the Dalitz plot kinematical boundary. we also have the following energy-momentum conservation:

$$\begin{aligned} \vec{p}_1 + \vec{p}_2 + \vec{p}_3 &= 0 \\ E_1 + E_2 + E_3 &= M_B \end{aligned} \quad (6.30)$$

Expressing all momenta in terms of  $E_1$  and  $E_3$  and nominal masses, we can yield that:

$$2\sqrt{(E_1^2 - m_1^2)(E_3^2 - m_3^2)} + m_2^2 - m_1^2 - m_3^2 - M_B^2 + 2M_B(E_1 + E_3) - 2E_1E_3 = 0 \quad (6.31)$$

By using Eq.(6.31) we can get the  $s_{12}$  and  $s_{23}$  boundaries on Dalitz plot, see more details in [44].

## 6.7 Fitting and Goodness-of-Fit

The amplitude analysis on Dalitz plot is performed by unbinned maximum likelihood fit. But unbinned maximum likelihood fit does not provide a direct goodness-of-fit, we estimate the goodness of fit by following two steps:

(1) We divide the entire Dalitz plot into  $1 \text{ (GeV}^2/c^4) \times 1 \text{ (GeV}^2/c^4)$  bins, if the number of events in one bin is less than  $N_{min} = 16$ , we combine this bin with adjacent bins until the number of events is more than  $N_{min}$ .

(2) And we calculate  $\chi^2$  by following two functions:

## 6.7. FITTING AND GOODNESS-OF-FIT

$$\chi^2 = -2 \sum_{i=1}^{N_{bins}} n_i \ln\left(\frac{p_i}{n_i}\right)$$

$$\chi^2 = \sum_{i=1}^{N_{bins}} \frac{(p_i - n_i)^2}{n_i} \quad (6.33)$$

where  $n_i$  is the number of events in  $i$ -th bin,  $p_i$  is the predicted number of events from the fit.

Eq.(6.32) is from Garmash [9], and Eq.(6.33) is a general definition of  $\chi^2$ .





## 6.8 Fit Strategy

Amplitude analysis are performed with data sample only in  $\Delta E - M_{bc}$  signal box. We fit the data sample by using unbinned maximum likelihood fit, Eq.(6.23) becomes:

$$\mathcal{F} = -2 \sum_{\text{events}} \ln P(s_{12}, s_{23}; \xi) \quad (6.34)$$

$$P(s_{12}, s_{23}; \xi) = F \frac{S(s_{12}, s_{23}; \xi)}{\sum_{MC} S(s_{12}, s_{23}; \xi)} + (1 - F) \frac{B(s_{12}, s_{23})}{\sum_{MC} B(s_{12}, s_{23}; \xi)}$$

where mode 1 and mode 2 are  $B^0 \rightarrow \eta(\gamma\gamma)K\pi$  and  $B^0 \rightarrow \eta(\pi^+\pi^-\pi^0)K\pi$ , separately;  $F$  is the fraction of signal in data sample, the value in general is a constant, but it's a function here like this:  $F(\Delta E, M_{bc})$ , the fraction value depends on the position on  $\Delta E - M_{bc}$  scatter plot;

The description of signal amplitude on Dalitz plot of  $\eta K^+\pi^-$  is:

$$\begin{aligned} \mathcal{M} = & c_{K^*} e^{i\phi_{K^*}} \mathcal{A}_1(\eta K^+\pi^- | K^*(892)^0) + c_{K_0^*} e^{i\phi_{K_0^*}} \mathcal{A}_0(\eta K^+\pi^- | K_0^*(1430)^0) \\ & + c_{K_2^*} e^{i\phi_{K_2^*}} \mathcal{A}_2(\eta K^+\pi^- | K_2^*(1430)^0) + c_{a_0^-} e^{i\phi_{a_0^-}} \mathcal{A}_0(K^+\pi^-\eta | a_0^-(980)^-) \\ & + c_{a_2^-} e^{i\phi_{a_2^-}} \mathcal{A}_2(K^+\pi^-\eta | a_2^-(1320)^-) + c_{nr} e^{i\phi_{nr}} \end{aligned} \quad (6.35)$$

details of this description are explained in section.6.3. We let the amplitude and relative phase of  $\eta K^*(892)^0$  be fixed, all others are float. The natural width of  $a_0^-(980)$  is not a definite value in PDG, we fix the value by 57MeV in fitting. The non-resonant term,  $c_{nr} e^{i\phi_{nr}}$ , is a complex constant in this study.

We should also consider the efficiency distribution on Dalitz plot, thus use the following description to model signal in data:

$$\mathcal{M}_{\text{in data}} = \mathcal{M} \times \epsilon(s_{12}, s_{23}) \quad (6.36)$$

where  $\epsilon(s_{12}, s_{23})$  is a function used to model the efficiency on Dalitz plot, it's from Monte Carlo.



## Chapter 7

# Systematics and Efficiency Correction

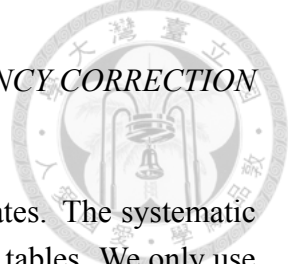
We discuss several kinds of systematic uncertainties here, the correlated errors are added linearly and uncorrelated the square root of quadratic sum. Table.7.7 shows the summary of systematic errors.

### 7.1 Tracking uncertainty

Tracking reconstruction of charged particles are studied using partially reconstructed  $D^{*+} \rightarrow D^0(\pi^+\pi^-\pi^0)\pi^+$  decay sample with  $P_T > 200\text{MeV}/c$  [45]. By comparing the track finding efficiency in data and Monte Carlo, the systematic uncertainty has been evaluated to be  $-0.13 \pm 0.30 \pm 0.10 \%$  for each track. The suggestion of the systematic uncertainty is of 0.35% per track and applied in the study.

### 7.2 PID Identification Uncertainty

The PID efficiency and fake rate are studied by using the inclusive  $D^*$  sample via PID Group, where  $D^{*+} \rightarrow D^0\pi^+$ ,  $D^0 \rightarrow K^+\pi^-$ . The  $K/\pi$  efficiency and fake rate are obtained by looking up the official table with corresponding  $P_{lab}$  and  $\cos\theta$  values. The results are used to correct branching fractions of our study. We generate a phase space MC sample, and then apply the PID efficiency correction on each bin ( $100 \times 100$ ) of Dalitz plot, thus to get a corrected efficiency function



of the position on Dalitz plot.

Table.7.1 and Table.7.2 show the efficiencies and fake rates. The systematic uncertainty from this source is evaluated by  $\frac{\text{statistical error}}{\text{meanvalue}}$  in the tables. We only use the error value as the systematic error in final result.

We have the PID efficiency correction of 0.9526 for  $(K^\pm\pi^\mp)$  in  $B^0 \rightarrow \eta(\gamma\gamma)K^\pm\pi^\mp$  and of 0.9388 for  $B^0 \rightarrow \eta(\pi^+\pi^-\pi^0)K^\pm\pi^\mp$ ; the systematic error is 1.23% and 1.50%, respectively.

Table 7.1: The KID efficiency (%) and fake rate for  $\eta(\gamma\gamma)K^\pm\pi^\mp$ . Ratio = (Data/MC).

	$K^+$	$K^-$	$\pi^+$	$\pi^-$
Data eff.	$85.93 \pm 0.50$	$86.32 \pm 0.49$	$88.34 \pm 0.45$	$87.79 \pm 0.46$
MC eff.	$86.69 \pm 0.05$	$86.62 \pm 0.05$	$92.54 \pm 0.03$	$92.52 \pm 0.03$
Ratio	$99.17 \pm 0.90$	$99.70 \pm 0.89$	$95.57 \pm 0.81$	$95.01 \pm 0.82$
Data fake	$8.56 \pm 0.42$	$8.94 \pm 0.43$	$9.90 \pm 0.45$	$9.67 \pm 0.45$
MC fake	$4.84 \pm 0.03$	$4.87 \pm 0.03$	$9.43 \pm 0.04$	$9.57 \pm 0.04$
Ratio	$175.59 \pm 11.39$	$183.86 \pm 11.54$	$105.52 \pm 7.52$	$102.27 \pm 7.32$

Table 7.2: The KID efficiency (%) and fake rate for  $\eta(\pi^+\pi^-\pi^0)K^\pm\pi^\mp$ . Ratio = (Data/MC).

$K^\pm$ and $\pi^\pm$ from $B$				
	$K^+$	$K^-$	$\pi^+$	$\pi^-$
Data eff.	$86.03 \pm 0.50$	$86.33 \pm 0.49$	$88.32 \pm 0.45$	$87.80 \pm 0.47$
MC eff.	$86.79 \pm 0.05$	$86.65 \pm 0.05$	$92.55 \pm 0.03$	$92.52 \pm 0.03$
Ratio	$99.30 \pm 0.90$	$99.81 \pm 0.91$	$95.66 \pm 0.81$	$95.10 \pm 0.82$
Data fake	$8.55 \pm 0.42$	$8.95 \pm 0.44$	$9.88 \pm 0.46$	$9.63 \pm 0.46$
MC fake	$4.85 \pm 0.03$	$4.87 \pm 0.03$	$9.38 \pm 0.04$	$9.54 \pm 0.04$
Ratio	$175.54 \pm 11.53$	$183.08 \pm 11.72$	$105.81 \pm 7.56$	$102.28 \pm 7.40$
$\pi^\pm$ from $\eta$				
	$\pi^+$	$\pi^-$		
Data eff.	$95.81 \pm 0.50$	$93.92 \pm 0.52$		
MC eff.	$97.56 \pm 0.04$	$96.36 \pm 0.04$		
Ratio	$98.79 \pm 0.83$	$98.34 \pm 0.85$		
Data fake	$9.30 \pm 0.48$	$7.45 \pm 0.48$		
MC fake	$10.08 \pm 0.07$	$8.20 \pm 0.06$		
Ratio	$98.95 \pm 10.05$	$98.86 \pm 11.41$		



### 7.3. NUMBER OF $B\bar{B}$ PAIRS UNCERTAINTY

## 7.3 Number of $B\bar{B}$ pairs uncertainty

There are  $771.581 \pm 10.566 \times 10^{-6}$   $B\bar{B}$  pairs in real data, the systematic error is 1.37% [46].

## 7.4 Signal PDF( $\Delta E$ , $M_{bc}$ ) uncertainty

This is obtained by varying each parameter of signal shape by  $\pm 1\sigma$  and obtain the yield difference. And the yield differences for every variation take the square root of quadratic sum. Table.7.3 shows all the parameters we considered and corresponding systematic error, here we only consider the fixed fitting parameters.

The total signal PDF uncertainty is 4.07% for  $B^0 \rightarrow \eta(\gamma\gamma)K^\pm\pi^\mp$  and 3.83% for  $B^0 \rightarrow \eta(\pi^+\pi^-\pi^0)K^\pm\pi^\mp$ .

Table 7.3: Parameters and the corresponding systematic error in signal PDF systematics study (%).

		$\eta(\gamma\gamma)K^+\pi^-$	$\eta(\pi^+\pi^-\pi^0)K^+\pi^-$
$\Delta E$	fudge factor	3.67	3.37
	$\sigma_2/\sigma_1$	0.18	0.21
	$\sigma_3/\sigma_1$	0.18	0.14
	Mean <sub>2</sub> - Mean <sub>1</sub>	0.02	0.01
	Mean <sub>3</sub> - Mean <sub>1</sub>	0.01	0.01
	Area <sub>2</sub> /Area <sub>1</sub>	0.21	0.26
	Area <sub>3</sub> /Area <sub>1</sub>	0.19	0.43
$M_{bc}$	fudge factor	1.70	1.63
	$\sigma_2/\sigma_1$	0.09	0.07
	Mean <sub>2</sub> - Mean <sub>1</sub>	0.04	0.28
	Area <sub>2</sub> /Area <sub>1</sub>	0.15	0.52
Summary		4.07	3.83

## 7.5 Rare B PDF uncertainty

The PDF of Rare B background is from Monte Carlo, however some of the assigned amplitude of decays channel in rare B MC are upper limit but not ob-

served, might not be very reliable. And we use 2D smooth function for rare B in data fit. The uncertainty is obtained by the signal yield by comparing fixing rare B to expected value and floating it. We have the rare B MC systematic error of 2.1% for  $B^0 \rightarrow \eta(\gamma\gamma)K^\pm\pi^\mp$  and 0.74% for  $B^0 \rightarrow \eta(\pi^+\pi^-\pi^0)K^\pm\pi^\mp$ .

## 7.6 MC efficiency uncertainty

Given by the ratio of statistical error in the total yield of signal MC, 0.18% for  $B^0 \rightarrow \eta(\gamma\gamma)K^\pm\pi^\mp$  and 0.29% for  $B^0 \rightarrow \eta(\pi^+\pi^-\pi^0)K^\pm\pi^\mp$ .

## 7.7 $\eta$ efficiency correction and systematics

The distribution of  $M_\eta$  is different between data and MC, therefore the efficiency of  $\eta$  mass requirement gotten from MC needs correction. We use the events in the sideband region,  $M_{\eta(\gamma\gamma)} < 0.47$  or  $> 0.59$  GeV/c<sup>2</sup>;  $M_{\eta(\pi^+\pi^-\pi^0)} < 0.535$  or  $> 0.56$  GeV/c<sup>2</sup>, to obtain the background shape and then fix all parameters of background to fit  $\eta$  distribution. We use Crystal Ball line plus Gaussian to model  $\eta$  shape, third order Chebyshev Polynomial for background shape. The efficiency correction of  $\eta$  between data and MC is obtained by comparing the data and MC. Table.7.4 show the results.

Table 7.4: The  $\eta$  selection efficiency(%) for data and MC. Ratio = (Data/MC).

	$\eta(\gamma\gamma)$	$\eta(\pi^+\pi^-\pi^0)$
Data eff.	$95.89 \pm 1.73$	$99.61 \pm 1.38$
MC eff.	$96.30 \pm 2.77$	$99.80 \pm 0.38$
Ratio	$99.57 \pm 3.38$	$99.81 \pm 1.43$

## 7.8 $\pi^0$ efficiency and systematic error

The  $\pi^0$  efficiency and the systematic error are obtained using the branching ratio of  $\tau^- \rightarrow \pi^-\pi^0\nu_\tau$  channel by lepton tagging method using case A and case B data. The efficiency correction is 95.7%, the corresponding systematic error is



## 7.9. $\mathcal{LR}$ CUT UNCERTAINTY

suggested to be 2.20%. This result also extends to high momentum as  $\eta(\gamma\gamma)$  to give  $\eta \rightarrow \gamma\gamma$  reconstruction systematic uncertainty.

## 7.9 $\mathcal{LR}$ cut uncertainty

The  $\mathcal{LR}$  cut uncertainty comes from the discrepancy of efficiency between data and MC. We calculate  $\mathcal{LR}$  of  $B^+ \rightarrow \bar{D}^0\pi^+$  by using the same fisher discriminant,  $\cos\theta_B$  and  $\Delta Z$  distribution obtained in the  $B \rightarrow \eta K\pi$  decay.

The yield before and after the  $\mathcal{LR}$  cut shown in Table.4.3 make a efficiency, we calculate the error for the efficiency by binomial error which is defined as:

$$error = \sqrt{\frac{\varepsilon \times (1 - \varepsilon)}{N}} \quad (7.1)$$

where  $\varepsilon$  is the efficiency and  $N$  the number of events before  $\mathcal{LR}$  cut. Table.7.5 shows the efficiency of data and MC, and the corresponding ratio ( $\varepsilon_{data}/\varepsilon_{MC}$ ).  $\mathcal{LR}$  systematic uncertainty is evaluated by the ratio value, the error of ratio is gotten by error propagation. We estimate the  $\mathcal{LR}$  systematic uncertainty by

$$\sqrt{(1 - ratio)^2 + error_{ratio}^2} \quad (7.2)$$

The  $\mathcal{LR}$  cut uncertainty is 0.98% for  $B^0 \rightarrow \eta(\gamma\gamma)K^\pm\pi^\mp$  and 0.69% for  $B^0 \rightarrow \eta(\pi^+\pi^-\pi^0)K^\pm\pi^\mp$ .

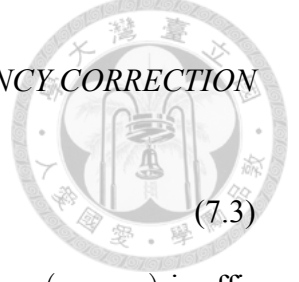
Table 7.5: The  $\mathcal{LR}$  cut efficiency(%) for data and MC. Ratio = (Data/MC).

	$\eta(\gamma\gamma)K^+\pi^-$	$\eta(\pi^+\pi^-\pi^0)K^+\pi^-$
Data eff.	$0.7640 \pm 0.0016$	$0.5433 \pm 0.0019$
MC eff.	$0.7569 \pm 0.0013$	$0.5404 \pm 0.0014$
Ratio	$1.0094 \pm 0.0027$	$1.0053 \pm 0.0044$

## 7.10 Reconstruction Efficiency

We also consider the efficiency correction for each resonance state depends on the position of Dalitz plot, it can be calculated by summation over a phase space sample:





$$\varepsilon_{res} = \frac{\sum_{MC} A_{res} \epsilon(s_{12}, s_{23})}{\sum_{MC} \epsilon(s_{12}, s_{23})} \quad (7.3)$$

where  $A_{res}$  is normalized amplitude for a resonance state;  $\epsilon(s_{12}, s_{23})$  is efficiency function generated by Monte Carlo, Fig.6.6 shows the distribution of efficiency over Dalitz plot.

For  $B \rightarrow \eta(\gamma\gamma)K^+\pi^-$  decay, we consider the  $\eta$  selection efficiency correction between data and MC, PID performance correction, efficiency for each resonance and the reconstruction efficiency gotten from signal MC sample:

$$\varepsilon_{recon} = \varepsilon_{MC} \times \varepsilon_{res} \times \varepsilon_{\eta} \times \varepsilon_{PID} \quad (7.4)$$

For  $B \rightarrow \eta(\pi^+\pi^-\pi^0)K^+\pi^-$  decay, we consider the  $\eta$  selection efficiency correction between data and MC, PID performance correction, efficiency for each resonance, the reconstruction efficiency gotten from signal MC sample and  $\pi^0$  reconstruction correction:

$$\varepsilon_{recon} = \varepsilon_{MC} \times \varepsilon_{res} \times \varepsilon_{\eta} \times \varepsilon_{PID} \times \varepsilon_{\pi^0} \quad (7.5)$$

Table.7.6 shows the summary of signal efficiencies and corrections, Table.7.7 shows the summary of systematic error.

In Dalitz plot analysis, we only fit data sample in signal region, the selection of signal region also have a corresponding efficiency. We get the efficiency directly by the results of  $\Delta E - M_{bc}$  2D-fit, it's 97.42% for  $\eta(\gamma\gamma)K^+\pi^-$  and 95.86% for  $\eta(\pi^+\pi^-\pi^0)K^+\pi^-$



Table 7.6: Signal efficiencies and efficiency corrections for each mode.

Mode	$\varepsilon_{MC}$ (%)	$\varepsilon_{PID}$	$\varepsilon_{res}$	$\varepsilon_{\eta}$	$\varepsilon_{\pi^0}$	$\varepsilon_{recon}$ (%)
$B \rightarrow \eta(\gamma\gamma)K^+\pi^-$						
$\eta K^*(892)$	12.84	0.9422	0.9577	0.9957	1.0	11.54
$\eta K_0^*(1430)$	12.84	0.9422	1.0879	0.9957	1.0	13.10
$\eta K_2^*(1430)$	12.84	0.9422	1.0279	0.9957	1.0	12.38
$K^+ a_0^-(980)$	12.84	0.9422	1.0349	0.9957	1.0	12.47
$K^+ a_2^-(1320)$	12.84	0.9422	0.9877	0.9957	1.0	11.90
Non-resonant	12.84	0.9422	1.0359	0.9957	1.0	12.48
$B \rightarrow \eta(\gamma\gamma)K^-\pi^+$						
$\eta \overline{K}^*(892)$	12.78	0.9528	0.9577	0.9957	1.0	11.61
$\eta \overline{K}_0^*(1430)$	12.78	0.9528	1.0879	0.9957	1.0	13.19
$\eta \overline{K}_2^*(1430)$	12.78	0.9528	1.0279	0.9957	1.0	12.46
$K^- a_0^+(980)$	12.78	0.9528	1.0349	0.9957	1.0	12.54
$K^- a_2^+(1320)$	12.78	0.9528	0.9877	0.9957	1.0	11.98
Non-resonant	12.78	0.9528	1.0359	0.9957	1.0	12.56
$B \rightarrow \eta(\pi^+\pi^-\pi^0)K^+\pi^-$						
$\eta K^*(892)$	5.18	0.9174	0.9775	0.9981	0.9570	4.44
$\eta K_0^*(1430)$	5.18	0.9174	1.0944	0.9981	0.9570	4.97
$\eta K_2^*(1430)$	5.18	0.9174	1.0276	0.9981	0.9570	4.66
$K^+ a_0^-(980)$	5.18	0.9174	1.1043	0.9981	0.9570	5.01
$K^+ a_2^-(1320)$	5.18	0.9174	0.8842	0.9981	0.9570	4.01
Non-resonant	5.18	0.9174	1.0439	0.9981	0.9570	4.74
$B \rightarrow \eta(\pi^+\pi^-\pi^0)K^-\pi^+$						
$\eta \overline{K}^*(892)$	5.17	0.9276	0.9775	0.9981	0.9570	4.48
$\eta \overline{K}_0^*(1430)$	5.17	0.9276	1.0944	0.9981	0.9570	5.01
$\eta \overline{K}_2^*(1430)$	5.17	0.9276	1.0276	0.9981	0.9570	4.71
$K^- a_0^+(980)$	5.17	0.9276	1.1043	0.9981	0.9570	5.06
$K^- a_2^+(1320)$	5.17	0.9276	0.8842	0.9981	0.9570	4.05
Non-resonant	5.17	0.9276	1.0439	0.9981	0.9570	4.78



Table 7.7: Systematic error for branching fraction (unit in %).

	$\eta(\gamma\gamma)K^\pm\pi^\mp$	$\eta(\pi^+\pi^-\pi^0)K^\pm\pi^\mp$
Tracking	0.49	0.70
PID	1.23	1.50
$N_{B\bar{B}}$	1.37	1.37
Signal PDF	4.07	3.83
Rare $B$ MC	2.10	0.74
Signal MC	0.18	0.29
$\eta$ mass window	3.39	1.43
$\pi^0/\eta \rightarrow \gamma\gamma$ reconstruction	2.20	2.20
$LR$ cut	0.98	0.69
$\eta$ mass window	3.39	1.43
2D fitter bias	0.76	1.32
Summary	6.52	5.38



# Chapter 8

## Summary and Conclusion

### 8.1 Fitting Results

Fig.8.1 shows the Dalitz plot in  $\Delta E - M_{bc}$  signal region,  $s_1$  stands for  $M_{K^+\pi^-}$  and  $s_2$  stands for  $M_{\eta\pi^-}$ .

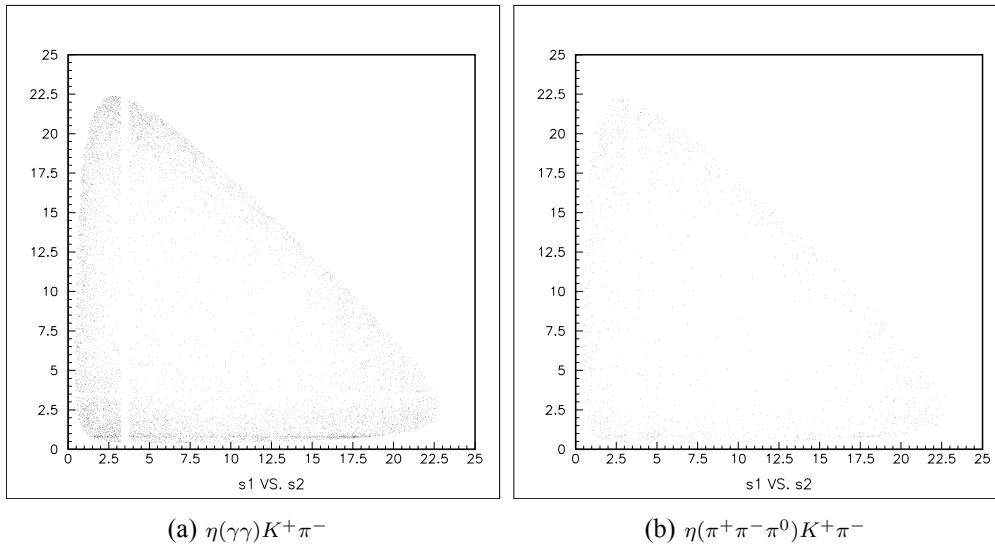


Figure 8.1: Dalitz plot in signal region after all selection requirements in data sample.

In data fitting, we find that LASS parametrization is better to describe  $K_0^*(1430)$  component and interference with non-resonant component, we also tried to use exponential forms to describe the excess component in  $1.0 < M_{K\pi} < 2.0 \text{ GeV}/c^2$ , several forms are adopted as Garmash used in  $h^+h^+h^-$  study [9], but there is no

any result good enough. So we only report the fitting result with LASS.

We calculate the branching fraction of  $K_0^*(1430)$  by the Breit-Wigner term of LASS, branching fraction of non-resonant decay by complex summation of constant term  $c_{nr}e^{i\phi_{nr}}$  and non-resonant term in LASS.

Table.8.1 shows the parameters of fitting results. Some other parameters are fixed but important are listed in Table.D.1. Fig.8.2 ~ Fig.8.9 show the projection plots in each slice and retire region. The close views of low  $M_{K\pi}$  and  $M_{\eta\pi}$  are shown in Fig.D.1 ~ Fig.D.4.

We also calculate the upper limits with 90% confidence level for those have statistical significance smaller than  $4\sigma$ .

$$\int_0^{f_{90}} G(\text{mean}, s; x)dx = 0.90 \int_0^{\infty} G(\text{mean}, s; x)dx \quad (8.1)$$

where  $\text{mean}$  is the mean value of branching fraction,  $s$  is the error and  $G(\text{mean}, s; x)$  is Gaussian function. We calculate  $(\text{mean} + 1.6423\sigma)$  directly to get the upper limit.

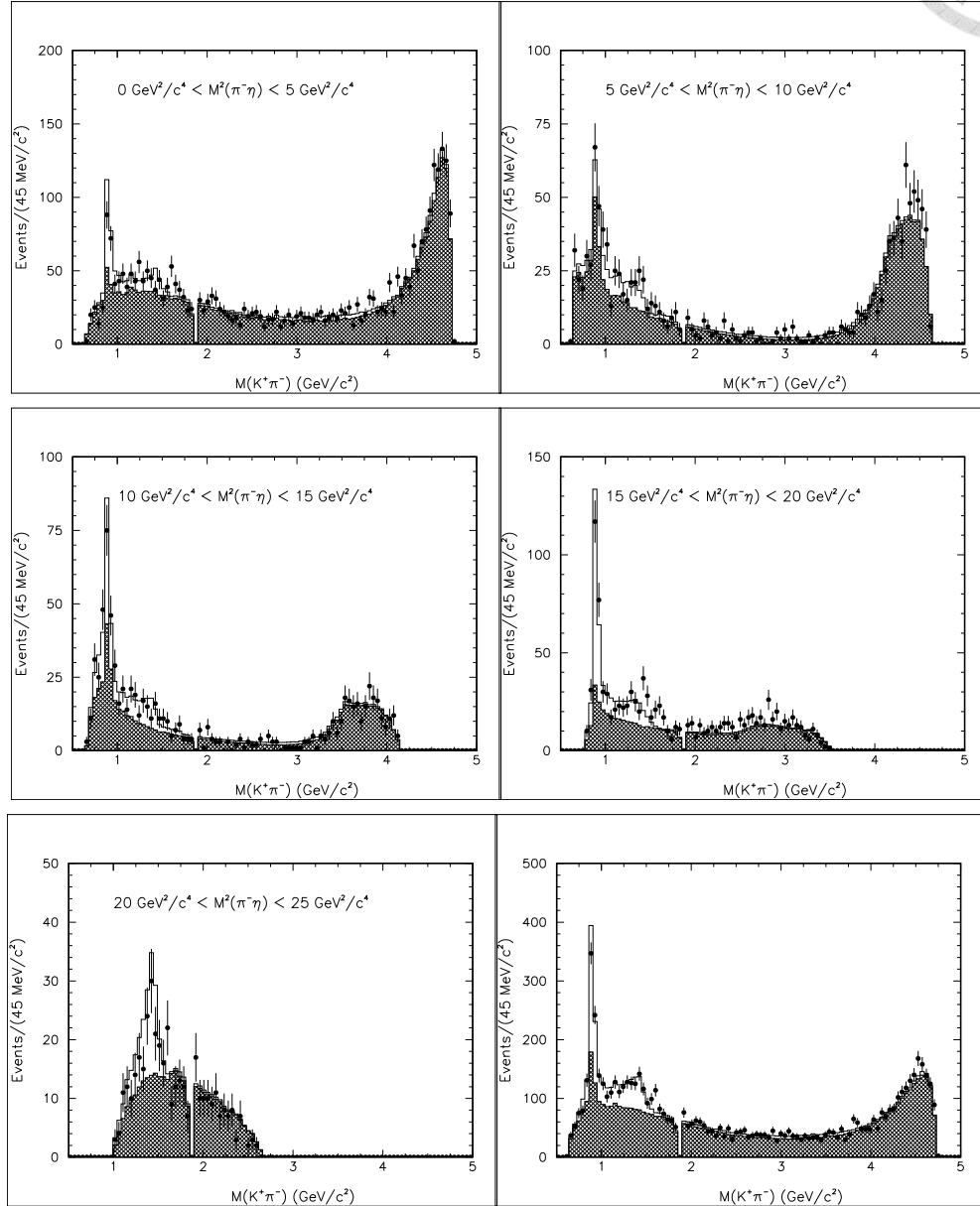


Figure 8.2: Dalitz analysis result in data  $\Delta E - M_{bc}$  signal box of  $\eta(\gamma\gamma)K^+\pi^-$ , first five plots show invariant mass of  $K^+\pi^-$  in  $M_{\eta\pi^-}$  slices, the bottom right one is the whole plot. Points with error bars are data, histograms are fit result, hatched histograms are background.

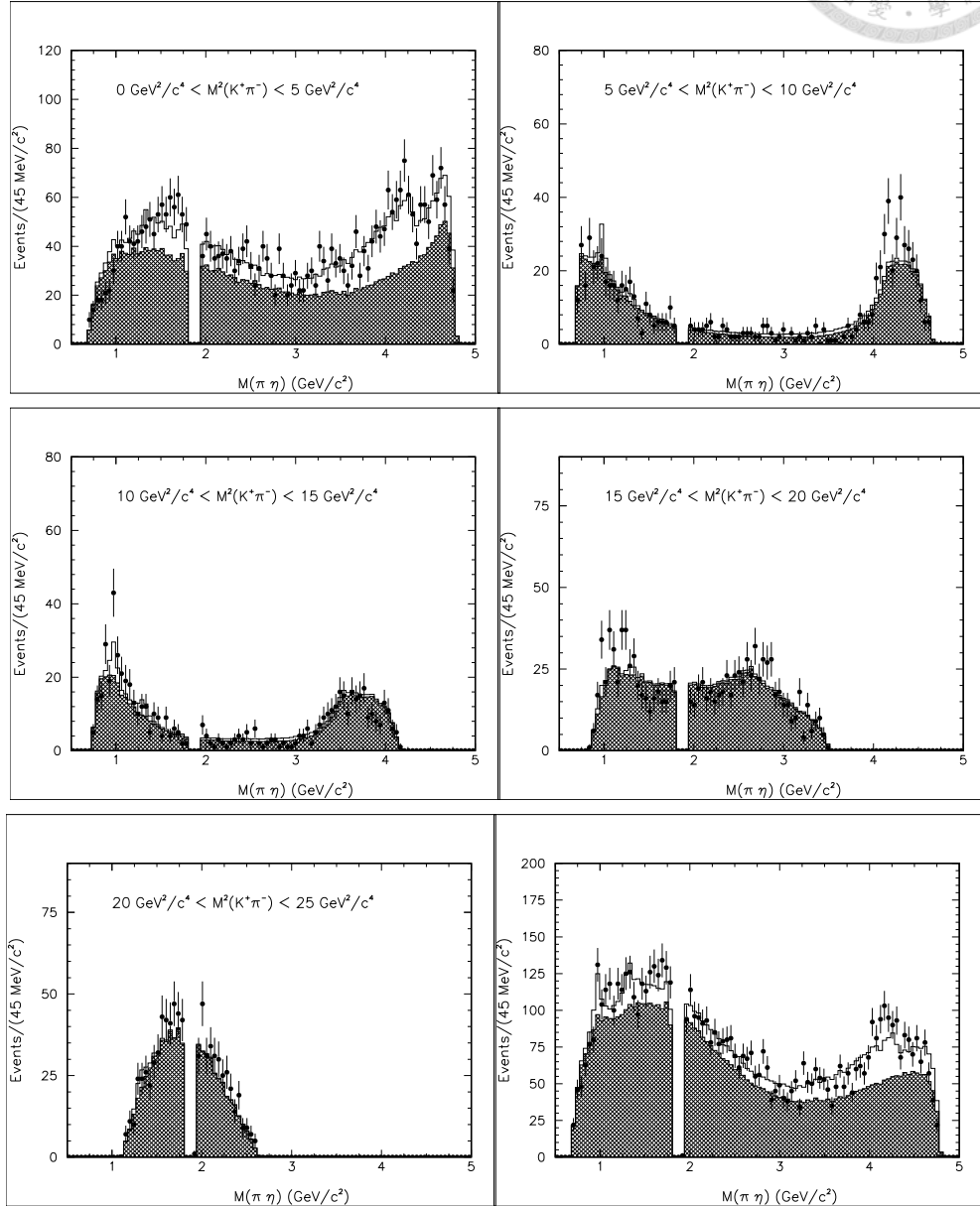


Figure 8.3: Dalitz analysis result in data  $\Delta E - M_{bc}$  signal box of  $\eta(\gamma\gamma)K^+\pi^-$ , first five plots show invariant mass of  $\eta\pi^-$  in  $M_{K^+\pi^-}$  slices, the bottom right one is the whole plot. Points with error bars are data, histograms are fit result, hatched histograms are background.

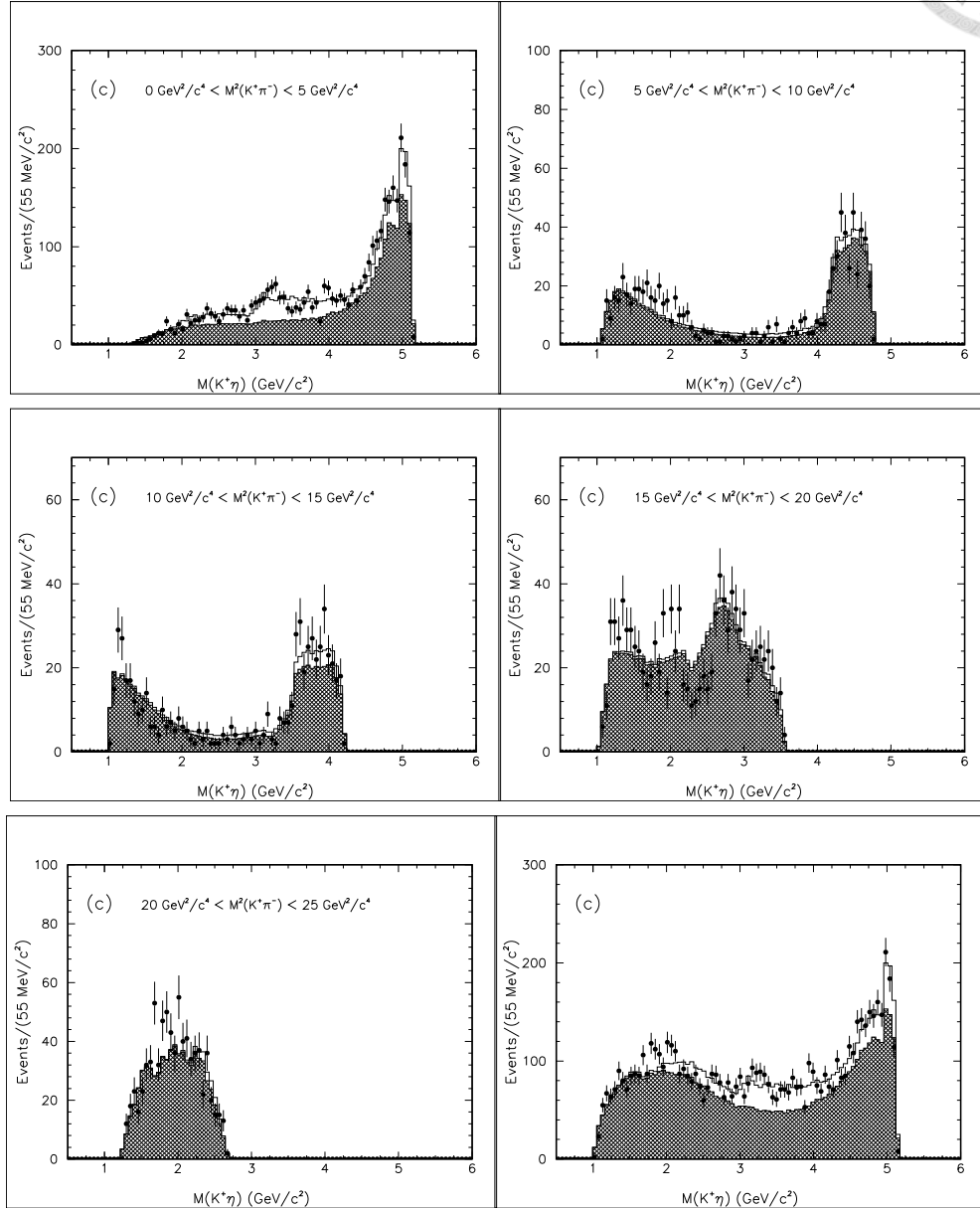


Figure 8.4: Dalitz analysis result in data  $\Delta E - M_{bc}$  signal box of  $\eta(\gamma\gamma)K^+\pi^-$ , first five plots show invariant mass of  $K^+\eta$  in  $M_{K^+\pi^-}$  slices, the bottom right one is the whole plot. Points with error bars are data, histograms are fit result, hatched histograms are background.



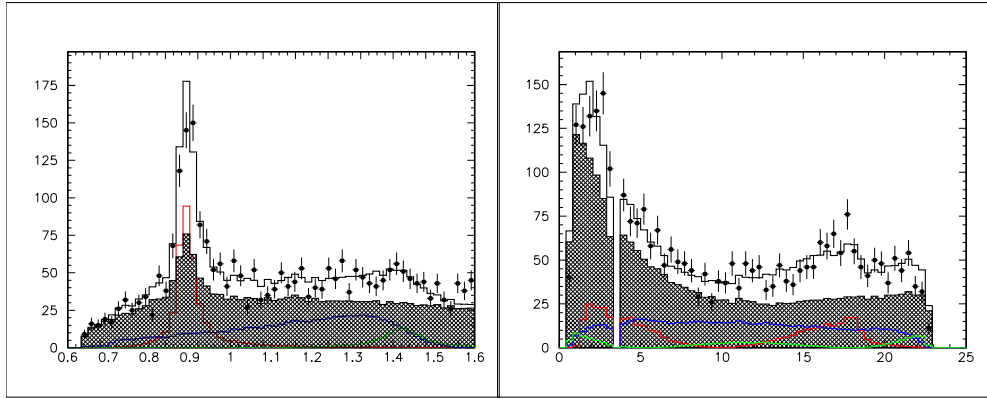


Figure 8.5: Dalitz analysis result in data  $\Delta E - M_{bc}$  signal box of  $\eta(\gamma\gamma)K^+\pi^-$ , the left plot is invariant mass of  $K^+\pi^-$ , the right plot is invariant mass of  $\eta\pi^-$  in  $M_{K\pi} < 1.8 \text{ GeV}/c^2$ . Points with error bars are data, histograms are fit result, hatched histograms are background, red line is  $K^*(892)^0$ , blue line is  $K_0^*(1430)^0$  by LASS, green line is  $K_2^*(1430)^0$ . The effect of interference between each component is not shown in these plots.

## 8.1. FITTING RESULTS

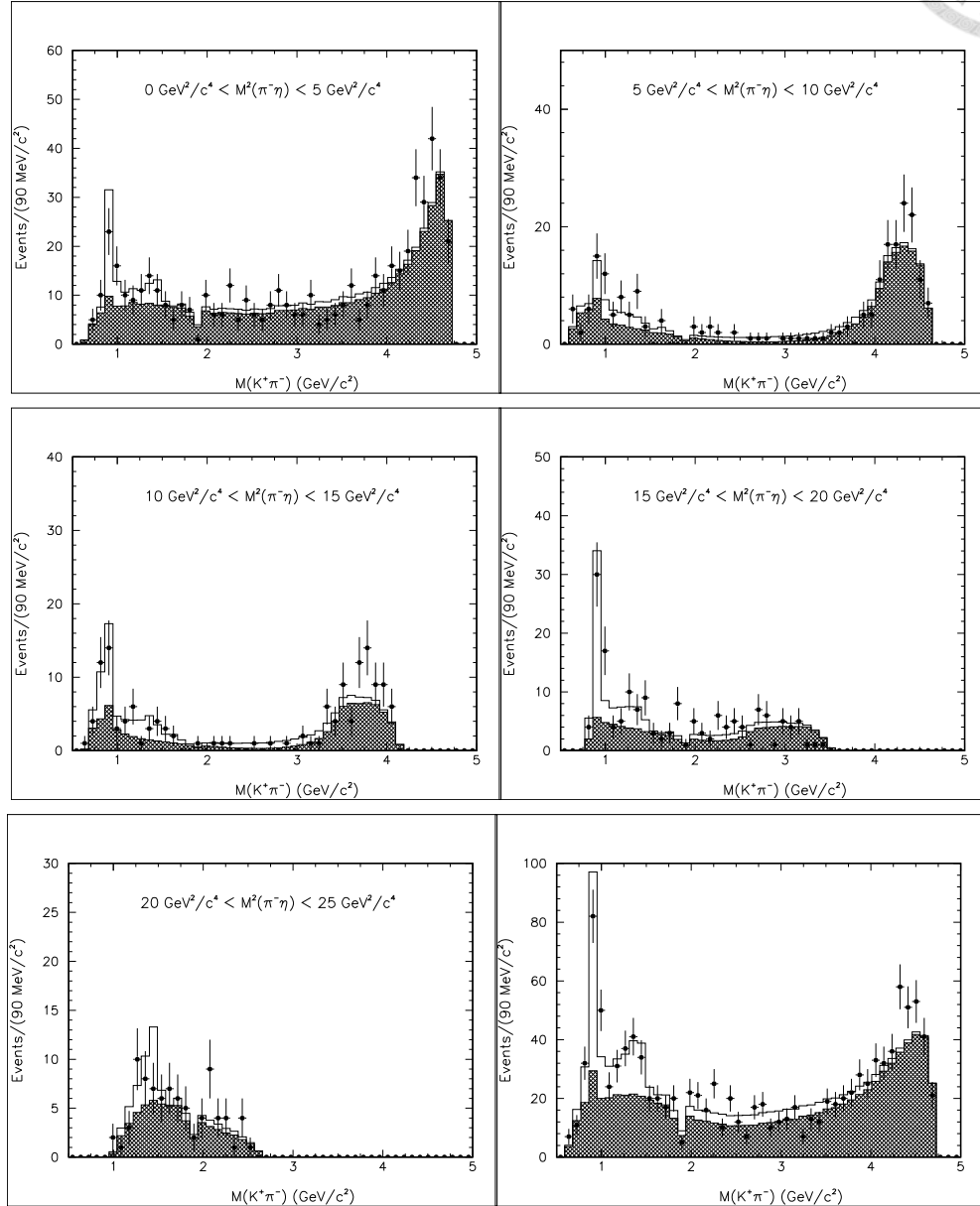


Figure 8.6: Dalitz analysis result in data  $\Delta E - M_{bc}$  signal box of  $\eta(\pi^+\pi^-\pi^0)K^+\pi^-$ , first five plots show invariant mass of  $K^+\pi^-$  in  $M_{\eta\pi^-}$  slices, the bottom right one is the whole plot. Points with error bars are data, histograms are fit result, hatched histograms are background.

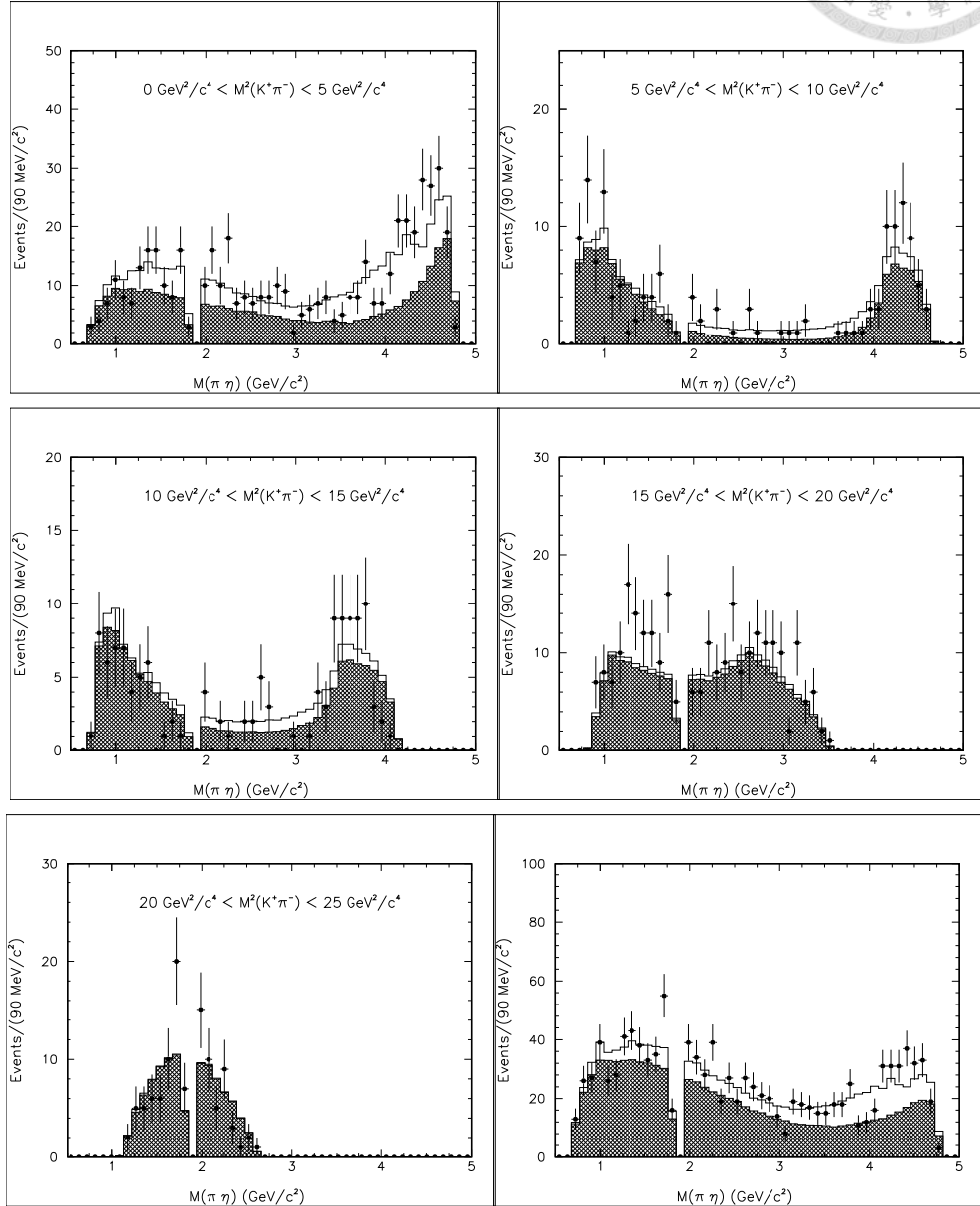


Figure 8.7: Dalitz analysis result in data  $\Delta E - M_{bc}$  signal box of  $\eta(\pi^+\pi^-\pi^0)K^+\pi^-$ , first five plots show invariant mass of  $\eta\pi^-$  in  $M_{K^+\pi^-}$  slices, the bottom right one is the whole plot. Points with error bars are data, histograms are fit result, hatched histograms are background.

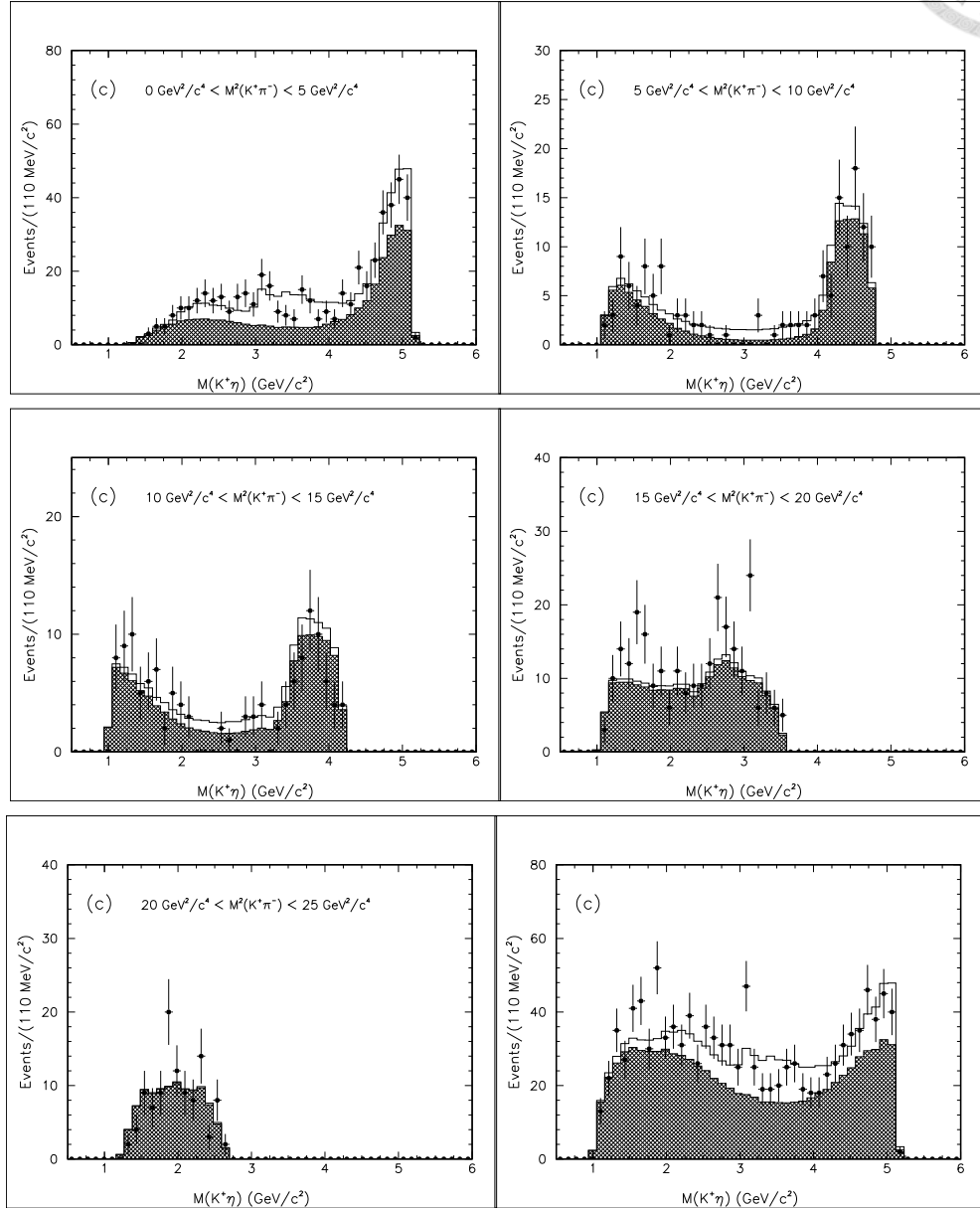


Figure 8.8: Dalitz analysis result in data  $\Delta E - M_{bc}$  signal box of  $\eta(\pi^+\pi^-\pi^0)K^+\pi^-$ , first five plots show invariant mass of  $K^+\eta$  in  $M_{K^+\pi^-}$  slices, the bottom right one is the whole plot. Points with error bars are data, histograms are fit result, hatched histograms are background.

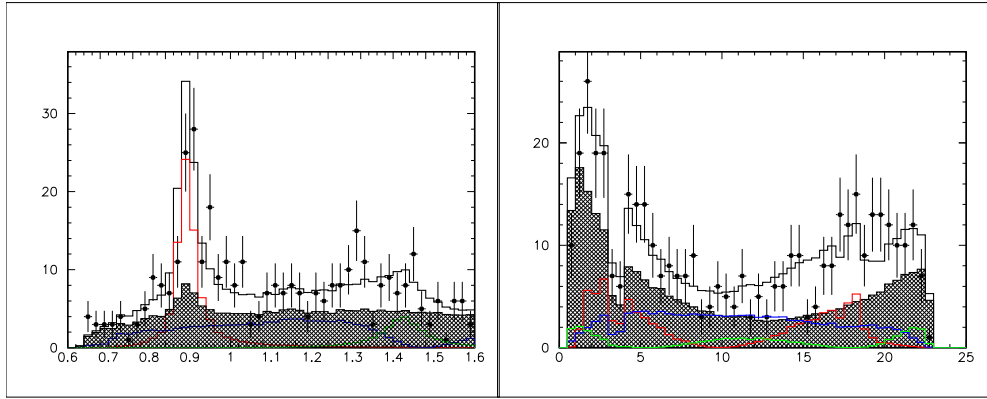


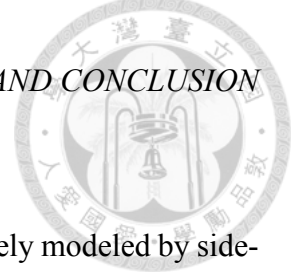
Figure 8.9: Dalitz analysis result in data  $\Delta E - M_{bc}$  signal box of  $\eta(\pi^+\pi^-\pi^0)K^+\pi^-$ , the left plot is invariant mass of  $K^+\pi^-$ , the right plot is invariant mass of  $\eta\pi^-$  in  $M_{K\pi} < 1.8 \text{ GeV}/c^2$ . Points with error bars are data, histograms are fit result, hatched histograms are background, red line is  $K^*(892)^0$ , blue line is  $K_0^*(1430)^0$  by LASS, green line is  $K_2^*(1430)^0$ . The effect of interference between each component is not shown in these plots.



## 8.1. FITTING RESULTS

Table 8.1: Results of Dalitz analysis in  $B^0 \rightarrow \eta K^+ \pi^-$  in signal box without considering  $CP$  violation.

Intermediate Mode	Parameter	Parameter value	
		$\eta \rightarrow \gamma\gamma$	$\eta \rightarrow \pi^+ \pi^- \pi^0$
$K^*(892)^0 \eta$	fraction, %	$33.20 \pm 2.63$	$29.22 \pm 6.19$
	phase, $^\circ$	0 (fixed)	0 (fixed)
$(K_0^*(1430)^0 \eta) \times (K_0^*(1430)^0 \rightarrow K^+ \pi^-)$	fraction, %	$34.03 \pm 2.80$	$22.12 \pm 4.69$
	phase, $^\circ$	$24.65 \pm 6.26$	$333.12 \pm 15.75$
$(K_2^*(1430)^0 \eta) \times (K_2^*(1430)^0 \rightarrow K^+ \pi^-)$	fraction, %	$9.31 \pm 1.26$	$9.59 \pm 2.44$
	phase, $^\circ$	$30.31 \pm 8.29$	$22.63 \pm 21.64$
$(a_0(980)^- K^+) \times (a_0(980)^- \rightarrow \eta \pi^-)$	fraction, %	$3.54 \pm 0.78$	$0.45 \pm 0.55$
	phase, $^\circ$	$244.33 \pm 25.42$	$97.07 \pm 107.52$
$(a_2(1320)^- K^+) \times (a_2(1320)^- \rightarrow \eta \pi^-)$	fraction, %	$6.29 \pm 1.09$	$4.26 \pm 5.87$
	phase, $^\circ$	$198.36 \pm 15.94$	$133.96 \pm 34.79$
Non-resonant	fraction, %	$36.49 \pm 1.80$	$51.48 \pm 5.08$
	phase, $^\circ$	$279.14 \pm 13.93$	$201.19 \pm 24.78$
	a(LASS)	$2.45 \pm 0.46$	$3.63 \pm 1.44$
	b(LASS)	$1.63 \pm 0.72$	$0.17 \pm 1.20$
Total charmless	fraction, %	$122.86 \pm 4.65$	$117.12 \pm 11.26$



## 8.2 Floating Background

Since the background of signal region can not be completely modeled by sideband, we float some parameters of background to get a better fit, they are  $\alpha_4$ ,  $\alpha_6$ ,  $\beta_4$ ,  $\beta_5$ ,  $\beta_8$  and  $\beta_9$  in Eq.(6.27). We also find that the contribution of uniform  $K^*(892)$  in background can largely vary with the different chosen sideband region, thus  $\alpha_7$  is also a float parameter. We define a low mass region(LMR) by  $0.755 < m_{K\pi} < 1.035 \text{ GeV}/c^2$  and high mass region(HMR) by  $1.035 < m_{K\pi} < 1.535 \text{ GeV}/c^2$ . And we compare the yield of  $\Delta E - M_{bc}$  2D-fit in these two region with the result of Dalitz analysis. We see that the results of Dalitz analysis are in statistical error of the results of  $\Delta E - M_{bc}$  2D-fit, thus we can trust floating the background in Dalitz fit.

Table 8.2: Comparison between  $\Delta E - M_{bc}$  fit and Dalitz analysis in LMR and HMR.

	LMR	HMR
$B^0 \rightarrow \eta(\gamma\gamma)K^+\pi^-$		
$\Delta E - M_{bc}$ fit	$430.54 \pm 29.54$	$417.33 \pm 30.59$
Dalitz analysis	$447.35 \pm 21.15$	$431.79 \pm 20.78$
$B^0 \rightarrow \eta(\pi^+\pi^-\pi^0)K^+\pi^-$		
$\Delta E - M_{bc}$ fit	$94.71 \pm 11.40$	$67.36 \pm 11.04$
Dalitz analysis	$90.88 \pm 9.53$	$74.76 \pm 8.65$

## 8.3 Conclusion

The measured branching fractions and upper limits at 90% confidence level are summarized in Table.8.3, the measured branching fractions and  $\mathcal{A}_{CP}$  for inclusive decay are in Table.E.1. We have similar results comparing with previous measurements for  $K^*$  modes (except  $K^*(892)$  mode where the result is much smaller). We also observed a large branching fraction for non-resonant decay. Our measurement for  $B^0 \rightarrow a_0(980)^- K^+$  is consistent with the previous measurement. It may help to clarify the nature of  $a_0(980)^-$ .

We already have preliminary results, but there are many things needed to be

### 8.3. CONCLUSION

studied. For examples :1. The modeling of background, we need a subtler method to understand the difference between signal box and sideband. 2. Study of  $\mathcal{A}_{CP}$  for each intermediate state is an undone work. 3. Less parameterization is simple to fit data, but is too complicate to manipulate and understand; we'll try more forms to describe non-resonant component.





Table 8.3: Branching fraction and significance for each mode, the first error term is statistical error and the second term is systematic error.

Mode	Branching fraction ( $\times 10^{-6}$ )	$\sigma$
$B \rightarrow \eta(\gamma\gamma)K^+\pi^-$		
$\eta K^*(892)$	$11.24 \pm 1.29 \pm 0.73$	21.43
$(K_0^*(1430)^0 \eta) \times (K_0^*(1430)^0 \rightarrow K^+\pi^-)$	$11.52 \pm 1.38 \pm 0.75$	5.68
$(K_2^*(1430)^0 \eta) \times (K_2^*(1430)^0 \rightarrow K^+\pi^-)$	$3.15 \pm 0.63 \pm 0.21$	4.35
$(a_0(980)^- K^+) \times (a_0(980)^- \rightarrow \eta\pi^-)$	$1.20 \pm 0.40 \pm 0.08 (< 1.87)$	(3.16)
$(a_2(1320)^- K^+) \times (a_2(1320)^- \rightarrow \eta\pi^-)$	$2.13 \pm 0.78 \pm 0.14 (< 3.16)$	(2.61)
Non-resonant	$12.35 \pm 1.25 \pm 0.81$	7.50
$B \rightarrow \eta(\pi^+\pi^-\pi^0)K^+\pi^-$		
$\eta K^*(892)$	$10.43 \pm 3.36 \pm 0.56$	10.83
$(K_0^*(1430)^0 \eta) \times (K_0^*(1430)^0 \rightarrow K^+\pi^-)$	$7.90 \pm 2.55 \pm 0.43$	6.68
$(K_2^*(1430)^0 \eta) \times (K_2^*(1430)^0 \rightarrow K^+\pi^-)$	$3.42 \pm 1.34 \pm 0.18$	4.37
$(a_0(980)^- K^+) \times (a_0(980)^- \rightarrow \eta\pi^-)$	$0.16 \pm 0.41 \pm 0.01 (< 0.83)$	(0.49)
$(a_2(1320)^- K^+) \times (a_2(1320)^- \rightarrow \eta\pi^-)$	$1.52 \pm 7.07 \pm 0.08 (< 13.13)$	(1.53)
Non-resonant	$18.38 \pm 2.65 \pm 0.99$	7.35



## Appendix A

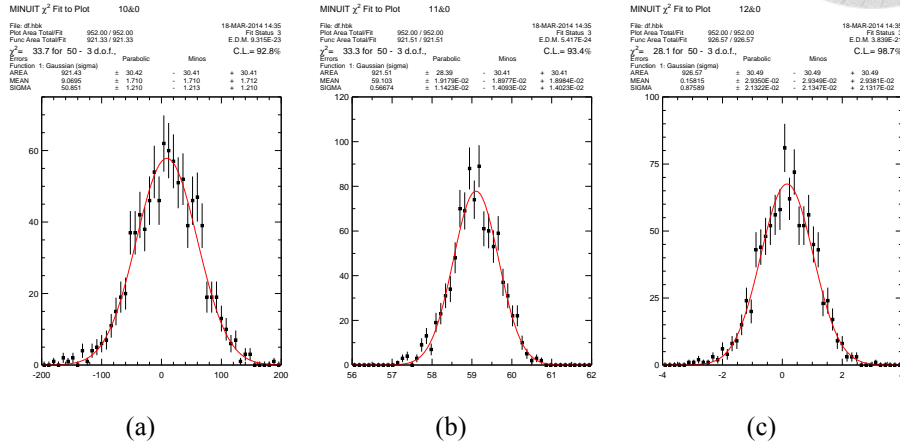
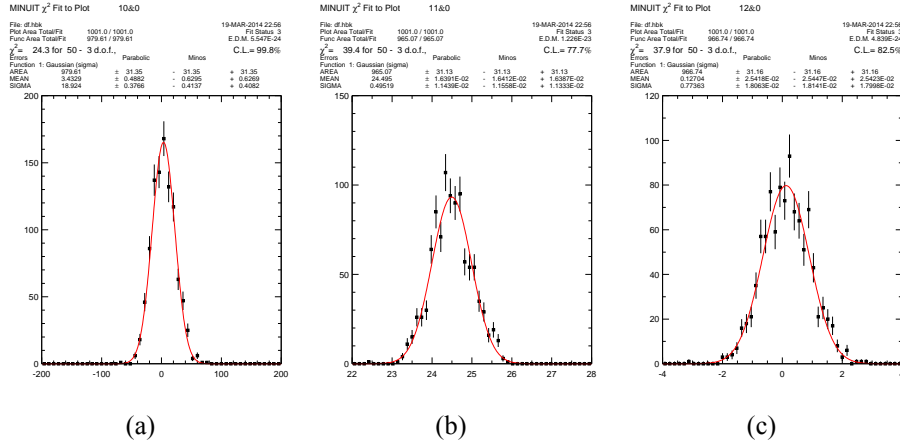
### Bias of 2D ( $\Delta E$ , $M_{bc}$ ) fit

We use ensemble test to check the fit bias in our 2D fitter, all the signal events are from GSIM MC, all the backgrounds are toy. we generate two ensemble for  $B^0 \rightarrow \eta(\gamma\gamma)K^+\pi^-$  and  $B^0 \rightarrow \eta(\pi^+\pi^-\pi^0)K^+\pi^-$ , there are 1000 samples in each ensemble. Table.A.1 shows the input values and the fit results. Fig.A.1 and Fig.A.2 show the distributions of bias, error and pull for all fit parameters, we use one Gaussian to model them. The pull value is defined by

$$\text{Pull} = \frac{\text{yield} - \text{input number}}{\text{fitting error}} \quad (\text{A.1})$$

Table A.1: The input number and fitting value of ensemble test.

	Input number	Yield	Difference	$\varepsilon$ (%)
$\eta(\gamma\gamma)K^+\pi^-$	1200	1209.07	+9.07	0.76
$\eta(\pi^+\pi^-\pi^0)K^+\pi^-$	260	263.43	+3.43	1.32

Figure A.1: Bias, error and pull result of ensemble test for  $B^0 \rightarrow \eta(\gamma\gamma)K^+\pi^-$ .Figure A.2: Bias, error and pull result of ensemble test for  $B^0 \rightarrow \eta(\pi^+\pi^-\pi^0)K^+\pi^-$ .



## Appendix B

### Bias of Dalitz fitter

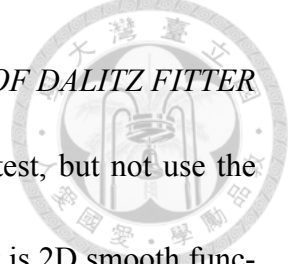
We check fit bias of Dalitz analysis by using ensemble test. In our ensemble, both signal and background are toyMC, 1000 samples are generated. In each sample,  $\Delta E$ ,  $M_{bc}$ ,  $M_{K^+\pi^-}$  and  $M_{\pi^-\eta}$ , these four parameters are generated. In ensemble test, we generate  $\Delta E$  and  $M_{bc}$  as data sample of  $B \rightarrow \eta(\gamma\gamma)K^+\pi^-$  mode to get fit bias.

The number of events in signal box of each component (signal and every background) are from  $\Delta E - M_{bc}$  2D yield fit directly; other parameters of PDF (probability density functions) of signal and background are the same. Number of events in signal box of each component is shown in Table.B.1, they are all fixed value in Dalitz analysis, just provide the signal fraction information for maximum likelihood fit.

Table B.1: Number of events in each sample while ensemble test.

Component	Number of events
Signal	1223
Continuum	6524
Rare B	1430
Generic B	702
Self-cross-feed	108

In order to check the fit bias of all signal parameter, and require that the statistics of each channel is similar, every decay channel (include non-resonant decay) are generated with similar number of events, we assign the amplitude of each de-



cay channel and relative phase between them in ensemble test, but not use the measurement result of previous study.

The description of background distribution on Dalitz plot is 2D smooth function, more details are shown in section.6.5

Table.B.2 and Table.B.3 show the assigned values ,the fit results, bias, error and pull values. Fig.B.2 - Fig.B.11 shows the distributions of bias, error and pull for all fit parameters, we use one Gaussian to model them. The pull value is defined by

$$\text{Pull} = \frac{\text{fitting value} - \text{input value}}{\text{fitting error}} \quad (\text{B.1})$$

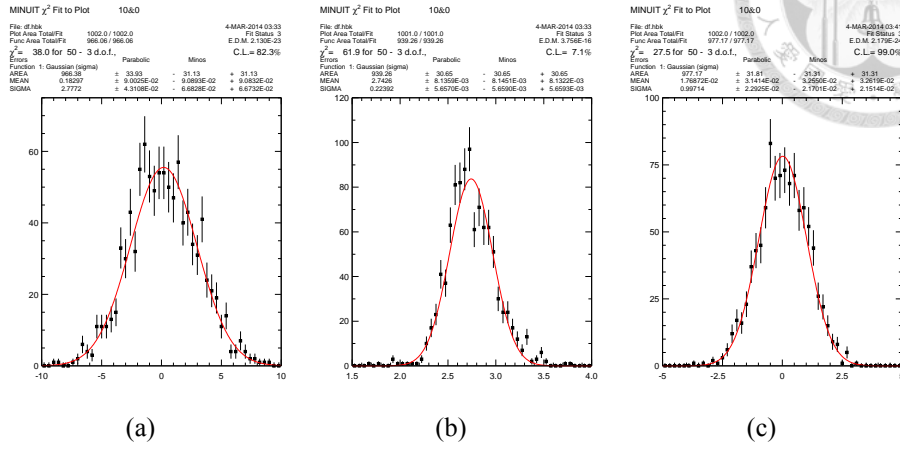
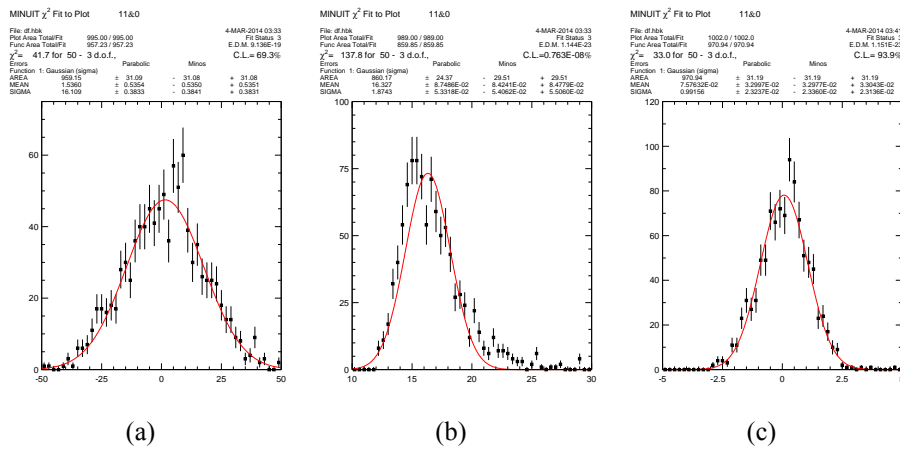
Table B.2: Given values and fit values for each parameter in ensemble test.

	Assigned values	Fit results
$A_{K^*}$	1, fixed	fixed
$\phi_{K^*}, ^\circ$	0, fixed	fixed
$A_{K_0^*}$	20.000	$20.186 \pm 0.086$
$\phi_{K_0^*}, ^\circ$	60.000	$61.063 \pm 0.559$
$A_{K_2^*}, \times 10^{-1}$	1.0000	$0.9980 \pm 0.0017$
$\phi_{K_2^*}, ^\circ$	120.00	$120.26 \pm 0.525$
$A_{a_0}$	10.000	$10.060 \pm 0.039$
$\phi_{a_0}, ^\circ$	180.00	$180.68 \pm 0.70$
$\Gamma_{a_0}, \times 10^{-2} \text{ (GeV)}$	5.7000	$5.6883 \pm 0.0270$
$A_{a_2}, \times 10^{-1}$	1.0000	$0.9995 \pm 0.0025$
$\phi_{a_2}, ^\circ$	210.00	$211.19 \pm 0.567$
$A_{nr}$	18.000	$18.192 \pm 0.053$
$\phi_{nr}, ^\circ$	240.00	$241.26 \pm 0.765$



Table B.3: Bias, error and pull for each parameter in ensemble test.

	Bias	Error	Pull ( $\times 10^{-2}$ )
$A_{K^*}$	fixed	fixed	fixed
$\phi_{K^*}, ^\circ$	fixed	fixed	fixed
$A_{K_0^*}$	$0.18297 \pm 0.09003$	$2.7426 \pm 0.00813$	$1.7687 \pm 3.1414$
$\phi_{K_0^*}, ^\circ$	$1.5360 \pm 0.5354$	$16.327 \pm 0.0875$	$7.5763 \pm 3.2997$
$A_{K_2^*}$	$-0.00023 \pm 0.00023$	$0.00765 \pm 0.00002$	$-3.7106 \pm 1.8061$
$\phi_{K_2^*}, ^\circ$	$0.28489 \pm 0.5459$	$16.471 \pm 0.085$	$0.3340 \pm 3.2342$
$A_{a_0}$	$0.05328 \pm 0.04059$	$1.1078 \pm 0.0044$	$-2.9517 \pm 3.6334$
$\phi_{a_0}, ^\circ$	$0.55756 \pm 0.72610$	$21.379 \pm 0.1065$	$3.2011 \pm 3.4202$
$\Gamma_{a_0}$ (GeV)	$-0.8881 \pm 2.6932$ ( $\times 10^{-4}$ )	$7.9800 \pm 0.0437$ ( $\times 10^{-3}$ )	$-10.558 \pm 3.503$
$A_{a_2}$	$0.1641 \pm 2.4955$ ( $\times 10^{-4}$ )	$7.8715 \pm 0.0168$ ( $\times 10^{-3}$ )	$-3.7397 \pm 3.1277$
$\phi_{a_2}, ^\circ$	$1.1663 \pm 0.5616$	$17.079 \pm 0.110$	$8.1889 \pm 3.2261$
$A_{nr}$	$0.18751 \pm 0.04309$	$1.6714 \pm 0.0044$	$7.5033 \pm 3.0423$
$\phi_{nr}, ^\circ$	$1.4350 \pm 0.7738$	$22.239 \pm 0.1145$	$10.069 \pm 3.364$

Figure B.1: Bias, error and pull result of ensemble test for the parameter  $A_{K_0^*}$ .Figure B.2: Bias, error and pull result of ensemble test for the parameter  $\phi_{K_0^*}$ .

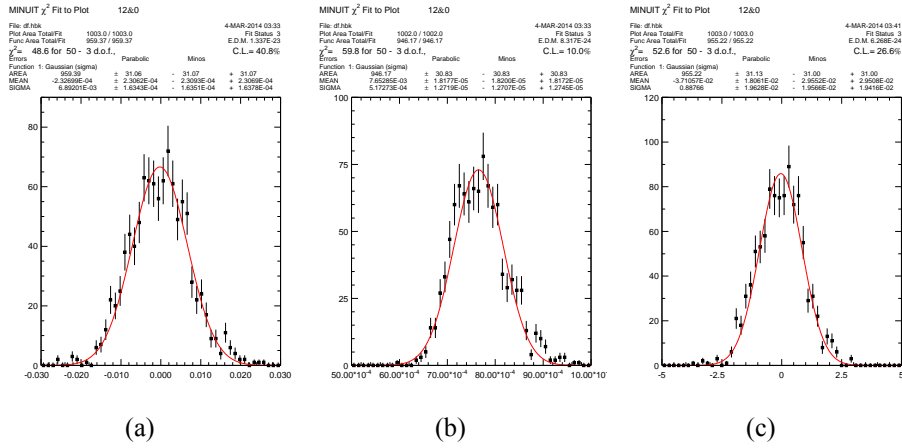


Figure B.3: Bias, error and pull result of ensemble test for the parameter  $A_{K_2^*}$ .

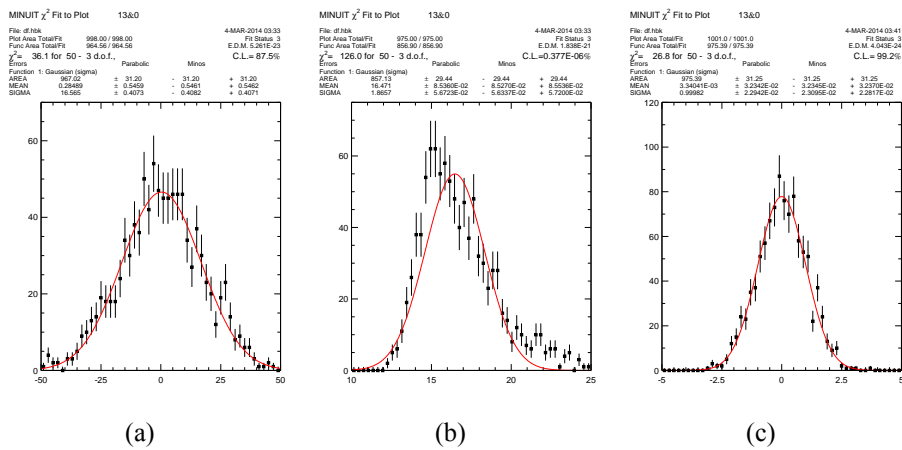
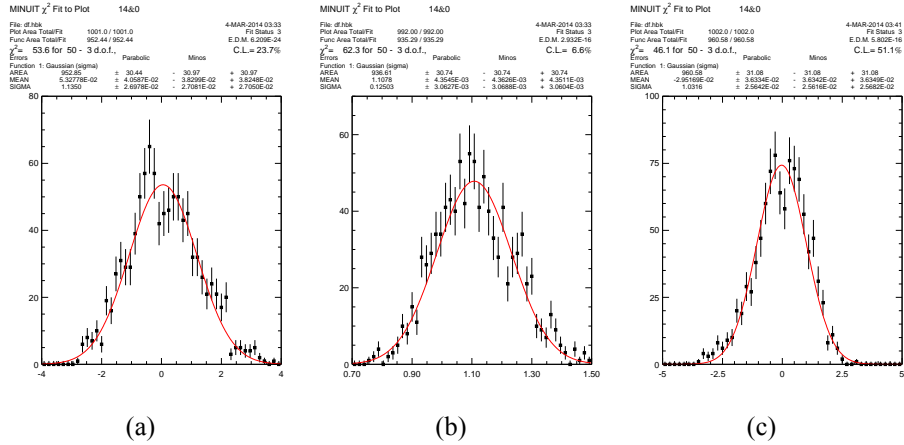
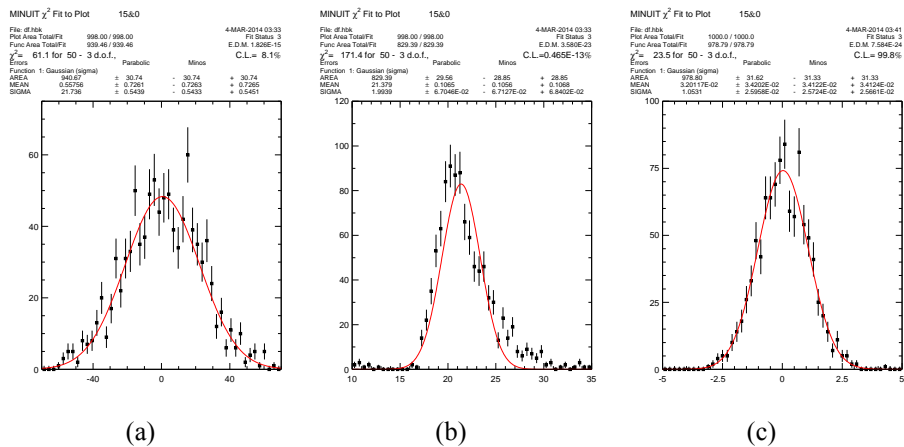


Figure B.4: Bias, error and pull result of ensemble test for the parameter  $\phi_{K_2^*}$ .



Figure B.5: Bias, error and pull result of ensemble test for the parameter  $A_{a_0}$ .Figure B.6: Bias, error and pull result of ensemble test for the parameter  $\phi_{a_0}$ .

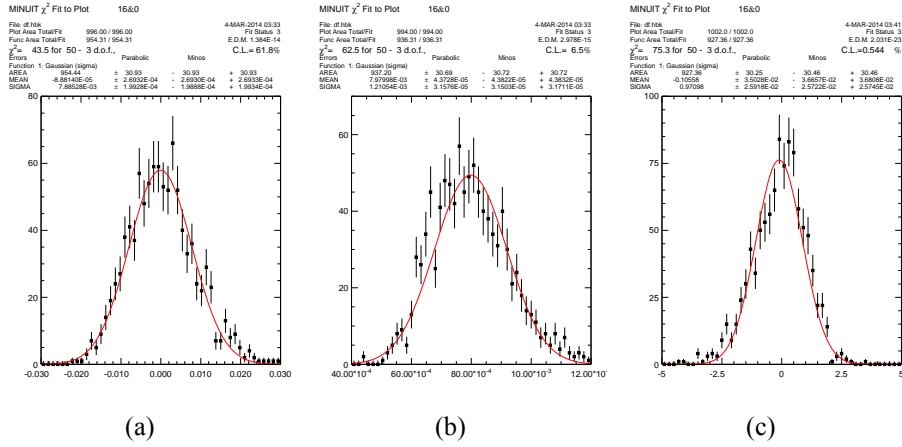


Figure B.7: Bias, error and pull result of ensemble test for the parameter  $\Gamma_{a_0}$ .

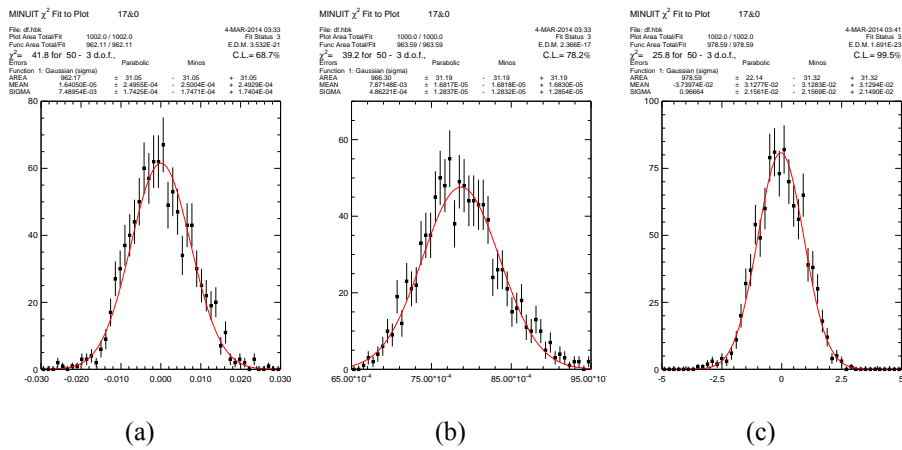
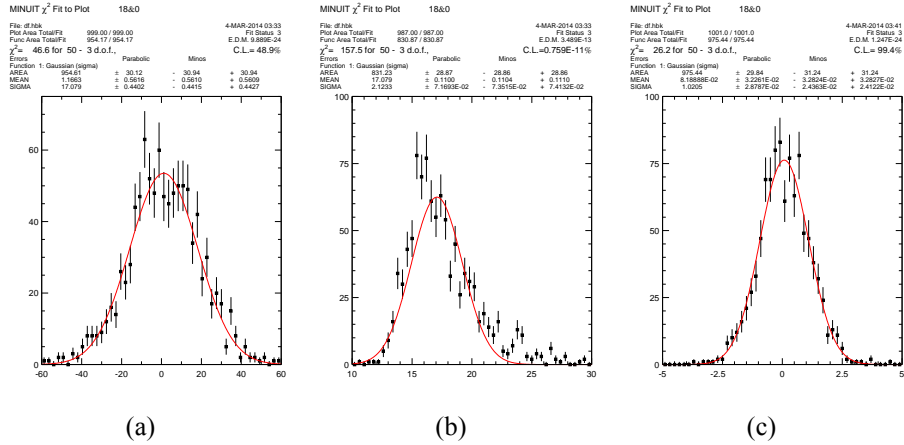
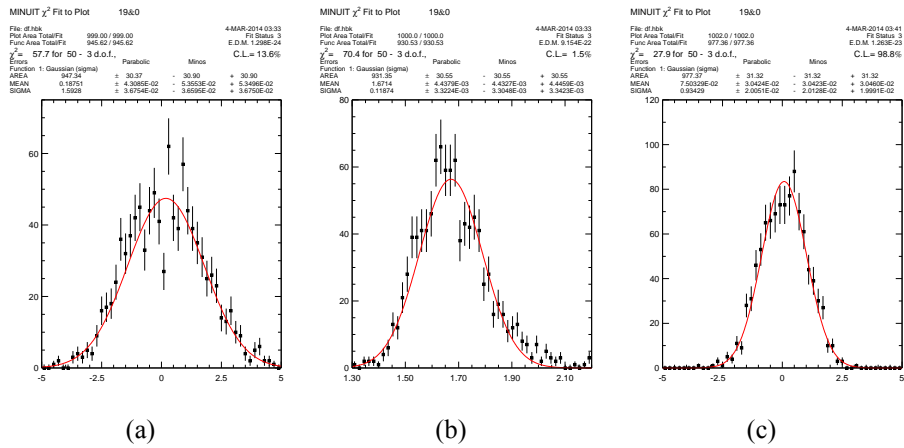


Figure B.8: Bias, error and pull result of ensemble test for the parameter  $A_{a_2}$ .

Figure B.9: Bias, error and pull result of ensemble test for the parameter  $\phi_{a_2}$ .Figure B.10: Bias, error and pull result of ensemble test for the parameter  $A_{nr}$ .

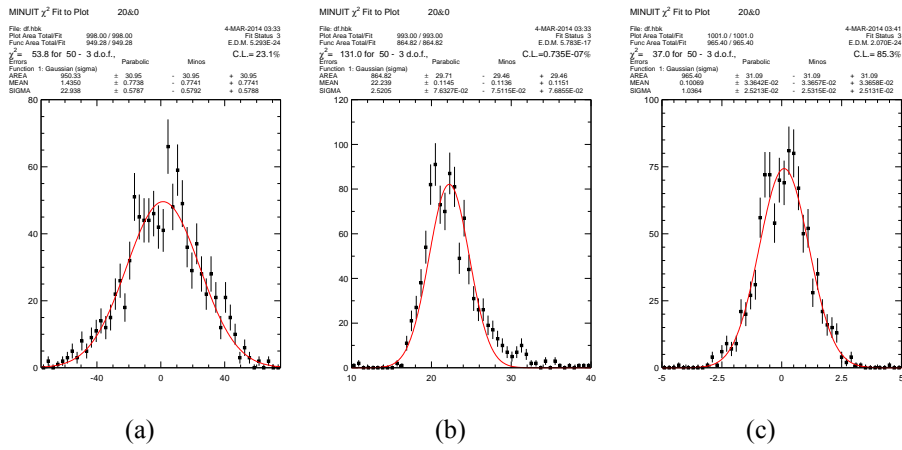


Figure B.11: Bias, error and pull result of ensemble test for the parameter  $\phi_{nr}$ .





## **Appendix C**

# **Figures of Dalitz Plot Sideband Modeling**

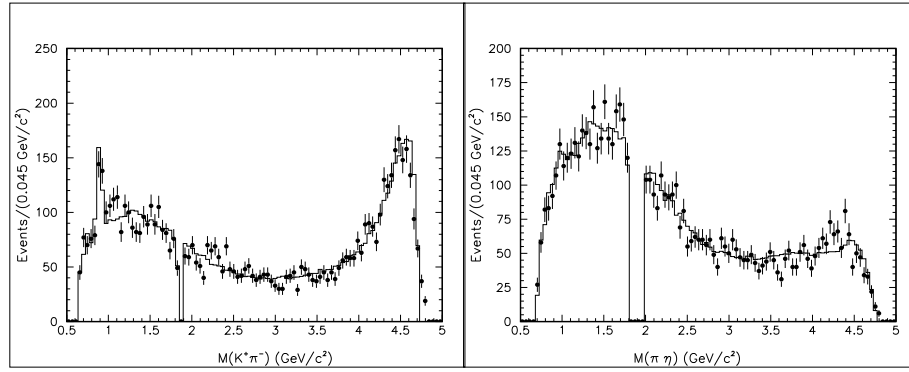
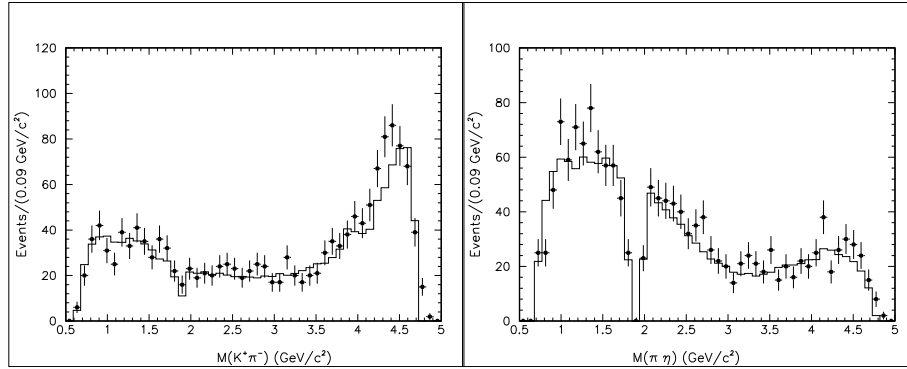
(a)  $\eta(\gamma\gamma)K^+\pi^-$ (b)  $\eta(\pi^+\pi^-\pi^0)K^+\pi^-$ 

Figure C.1: Result of unbinned maximum likelihood fit of parametrization in data  $\Delta E - M_{bc}$  sideband, the left two plots show the invariant mass of  $K^+\pi^-$ , the right two show the invariant mass of  $\pi^-\eta$ . Points with error bars are data, histograms are fit result.

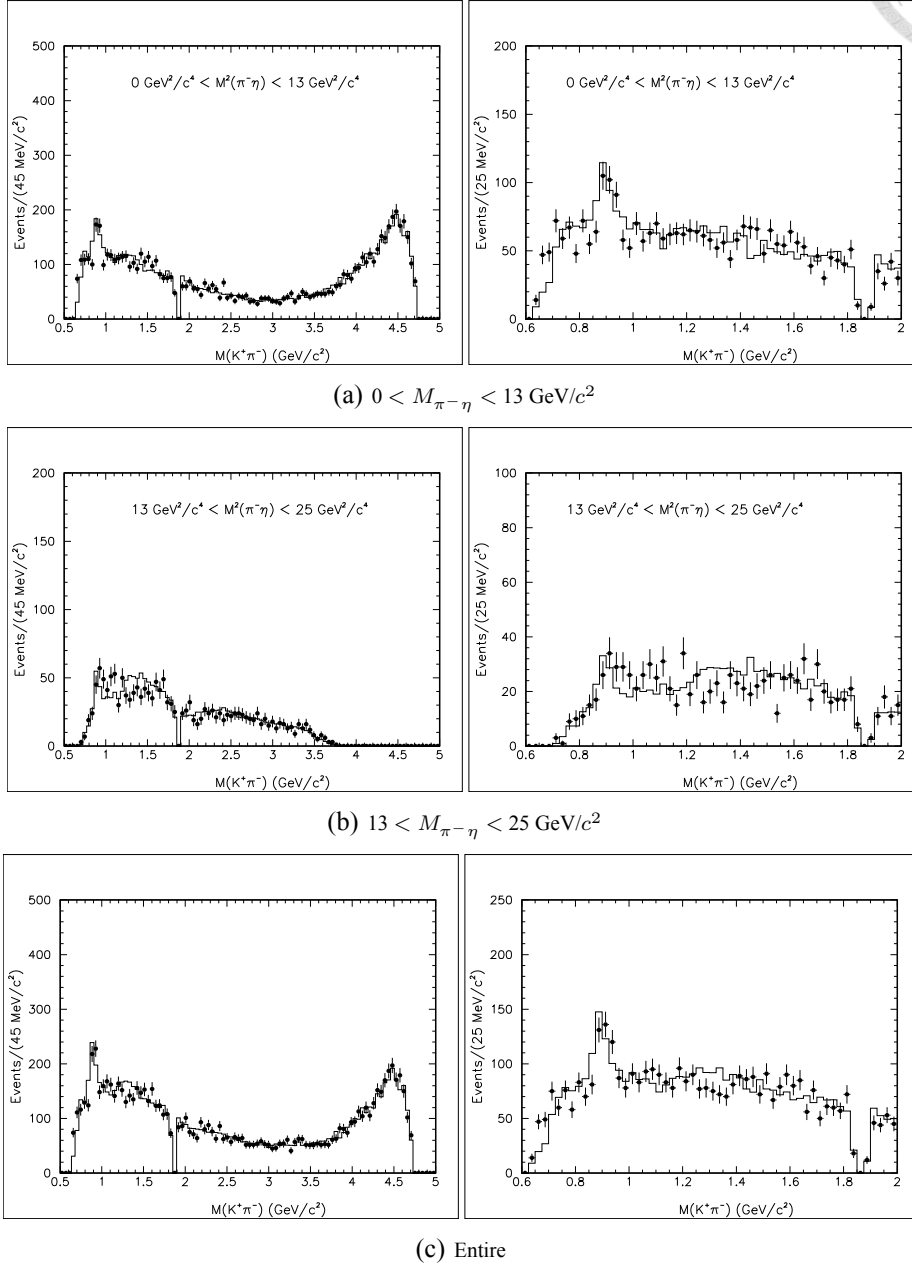


Figure C.2: Result of combined modeling method in data  $\Delta E - M_{bc}$  sideband of  $\eta(\gamma\gamma)K^+\pi^-$ , top four plots show invariant mass of  $K^+\pi^-$  in  $M_{\pi^- \eta}$  regions, the last one is the whole plot. Points with error bars are data, histograms are fit result. Right plots are close view in uniform resonance region.



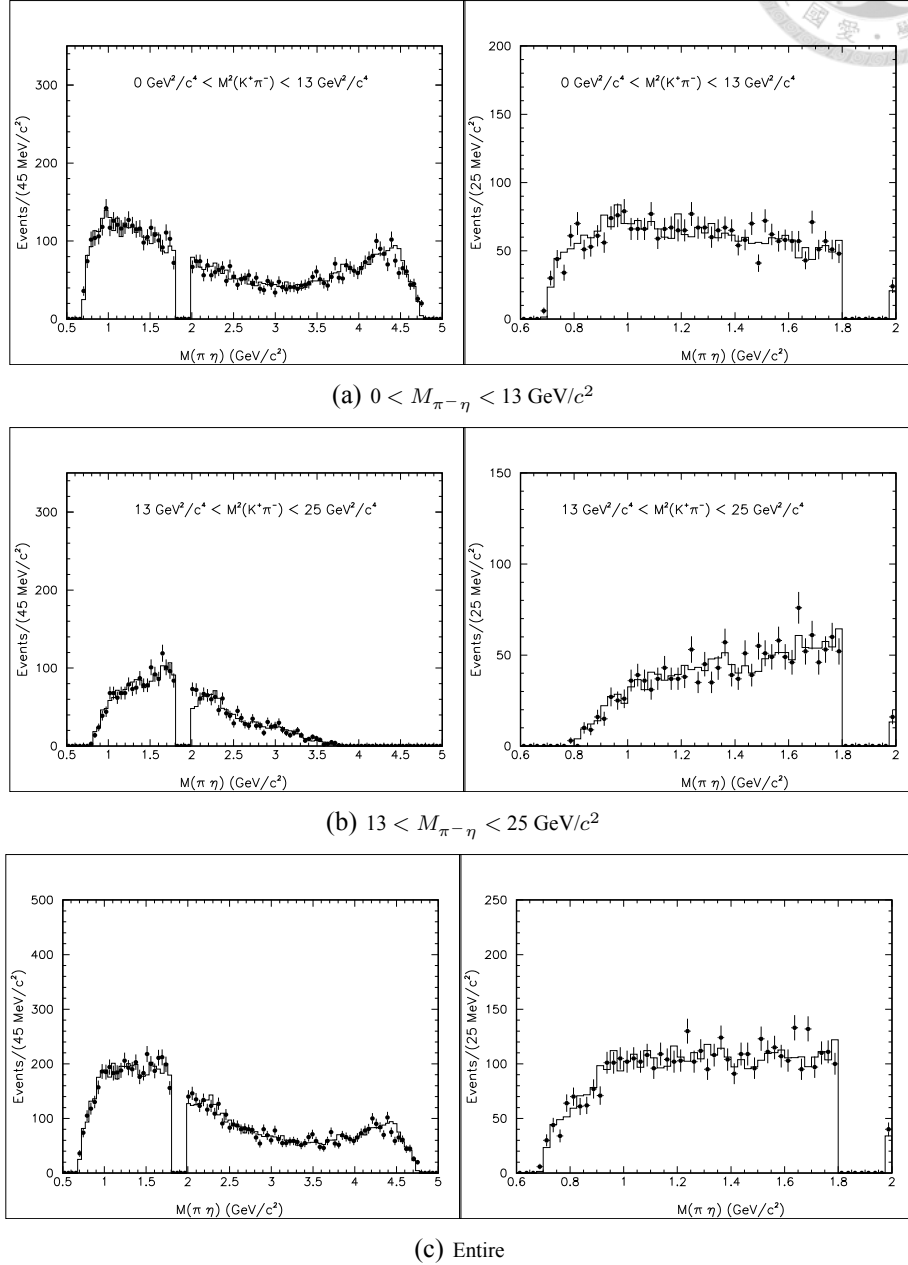
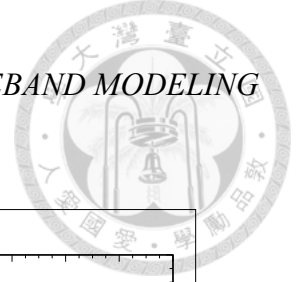


Figure C.3: Result of combined modeling method in data  $\Delta E - M_{bc}$  sideband of  $\eta(\gamma\gamma)K^+\pi^-$ , top four plots show invariant mass of  $\pi^-\eta$  in  $M_{K^+\pi^-}$  regions, the last one is the whole plot. Points with error bars are data, histograms are fit result. Right plots are close view in uniform resonance region.

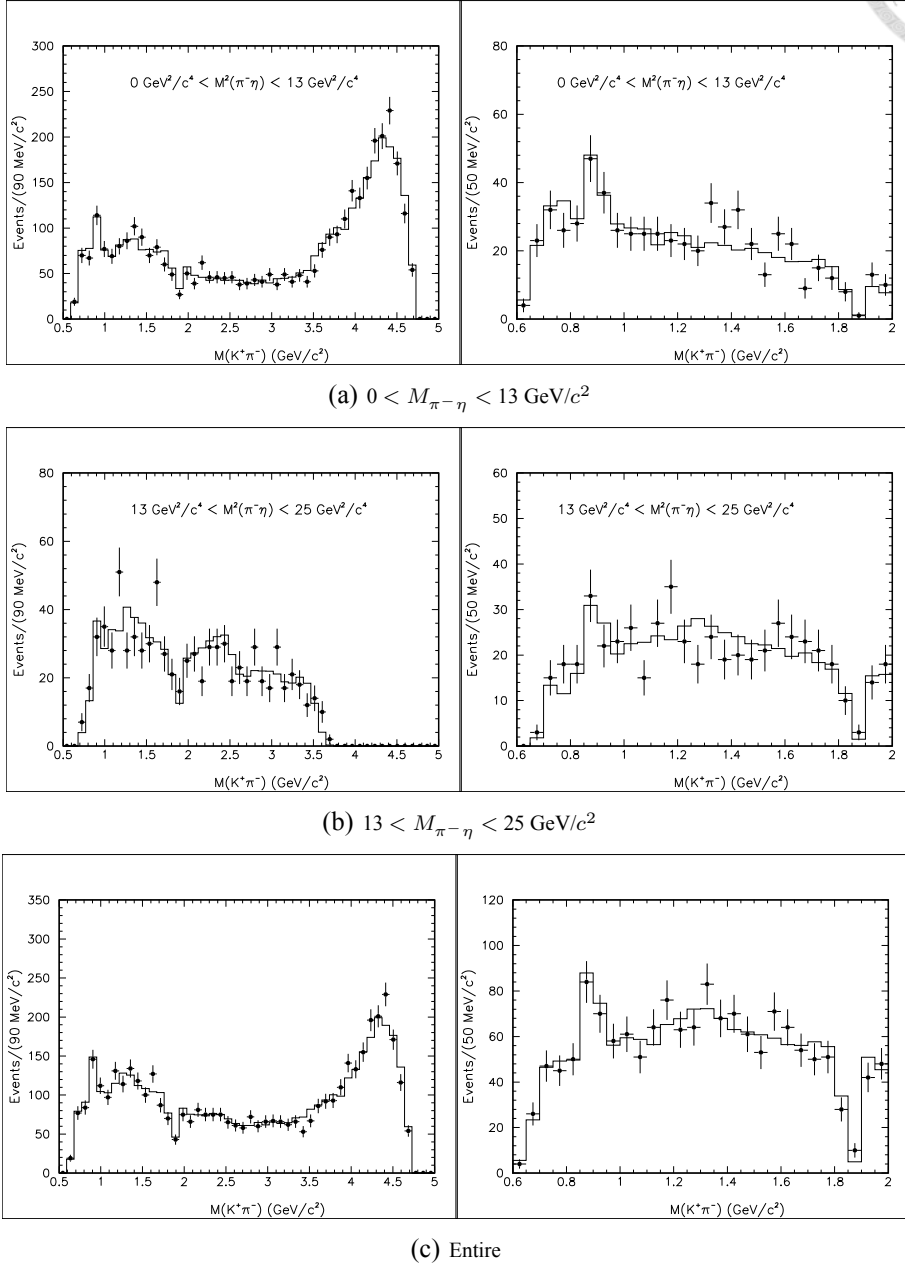


Figure C.4: Result of combined modeling method in data  $\Delta E - M_{bc}$  sideband of  $\eta(\pi^+\pi^-\pi^0)K^+\pi^-$ , top four plots show invariant mass of  $K^+\pi^-$  in  $M_{\pi-\eta}$  regions, the last one is the whole plot. Points with error bars are data, histograms are fit result. Right plots are close view in uniform resonance region.

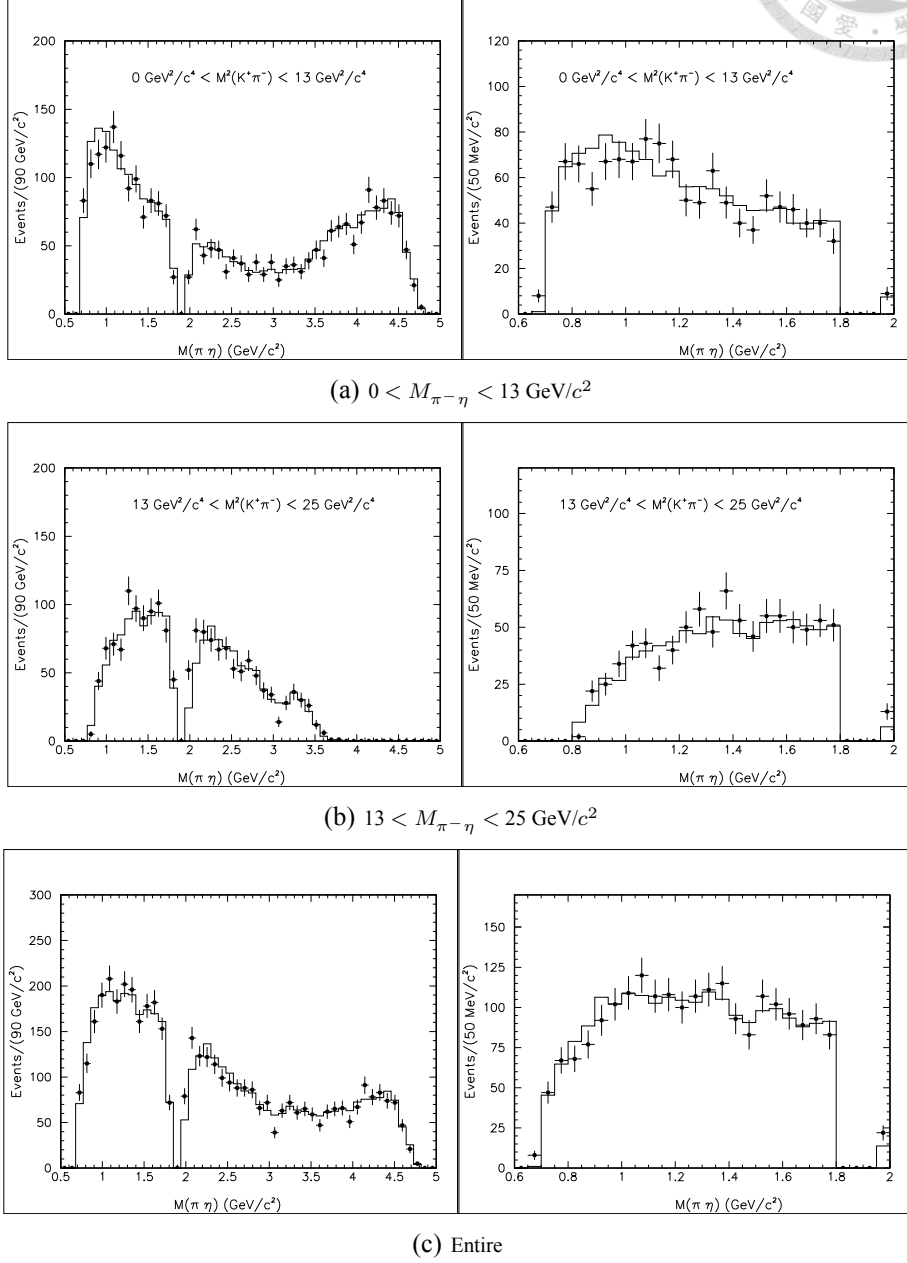
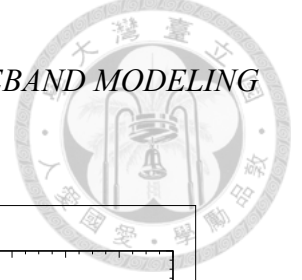


Figure C.5: Result of combined modeling method in data  $\Delta E - M_{bc}$  sideband of  $\eta(\pi^+\pi^-\pi^0)K^+\pi^-$ , top four plots show invariant mass of  $\pi^-\eta$  in  $M_{K^+\pi^-}$  regions, the last one is the whole plot. Points with error bars are data, histograms are fit result. Right plots are close view in uniform resonance region.



## Appendix D

### Dalitz analysis Backup

Table D.1: Fixed parameters of Dalitz analysis in  $B^0 \rightarrow \eta K^+ \pi^-$ .

Intermediate Mode	Parameter	Parameter value
$K^*(892)^0 \eta$	Mass, MeV/c <sup>2</sup>	897
	natural width( $\Gamma$ ), MeV	46.2
$K_0^*(1430)^0 \eta$	Mass, MeV/c <sup>2</sup>	1425
	natural width( $\Gamma$ ), MeV	270
$K_2^*(1430)^0 \eta$	Mass, MeV/c <sup>2</sup>	1432
	natural width( $\Gamma$ ), MeV	109
$a_0(980)^- K^+$	Mass, MeV/c <sup>2</sup>	980
	natural width( $\Gamma$ ), MeV	57
$a_2(1320)^- K^+$	Mass, MeV/c <sup>2</sup>	1318
	natural width( $\Gamma$ ), MeV	107
Threshold (LASS)	MeV/c <sup>2</sup>	1700

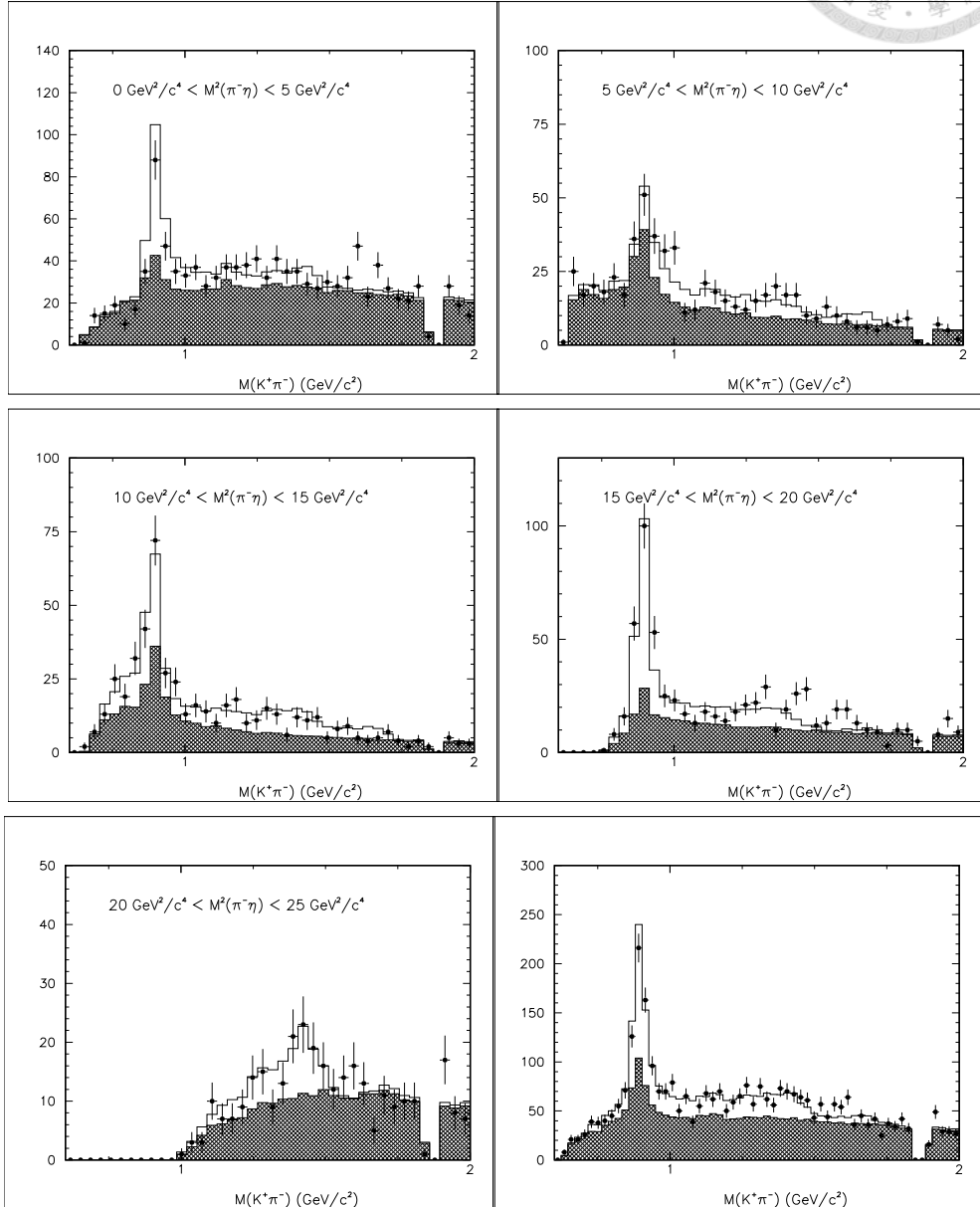


Figure D.1: Close look of Dalitz analysis result in data  $\Delta E - M_{bc}$  signal box of  $\eta(\gamma\gamma)K^+\pi^-$ , first five plots show invariant mass of  $K^+\pi^-$  in  $M_{\eta\pi^-}$  slices, the bottom right one is the whole plot. Points with error bars are data, histograms are fit result, hatched histograms are background.

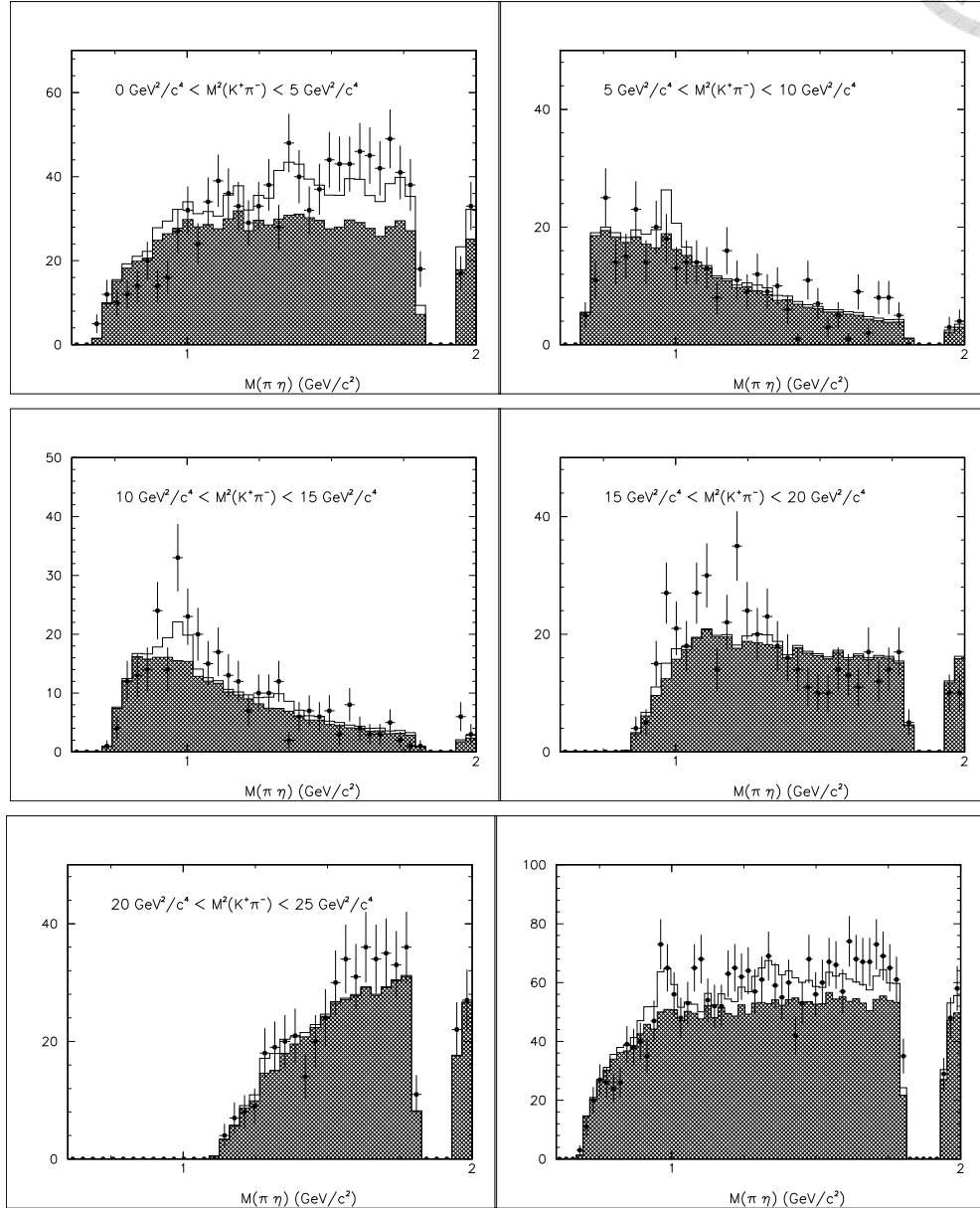


Figure D.2: Close look of Dalitz analysis result in data  $\Delta E - M_{bc}$  signal box of  $\eta(\gamma\gamma)K^+\pi^-$ , first five plots show invariant mass of  $\eta\pi^-$  in  $M_{K^+\pi^-}$  slices, the bottom right one is the whole plot. Points with error bars are data, histograms are fit result, hatched histograms are background.

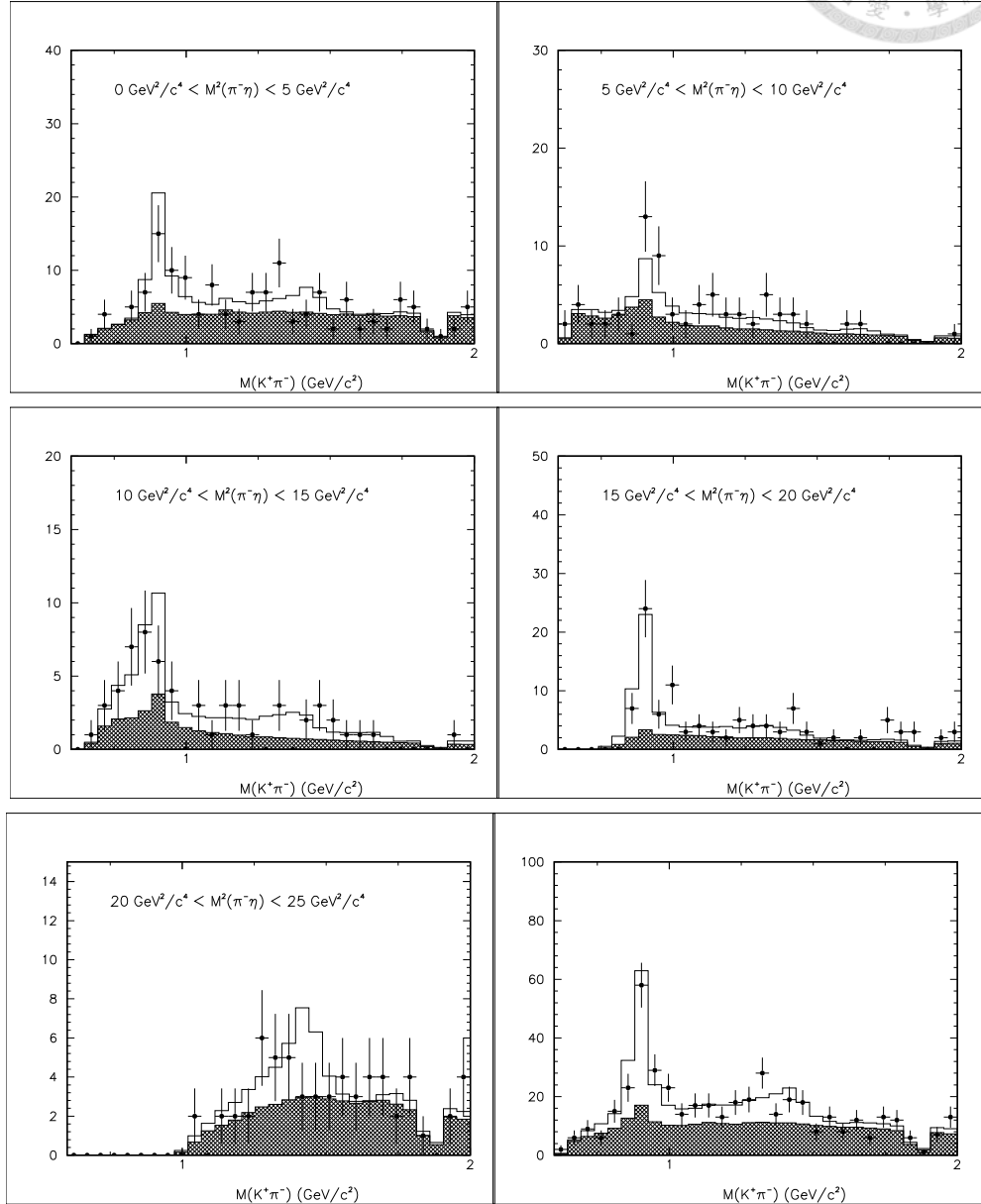
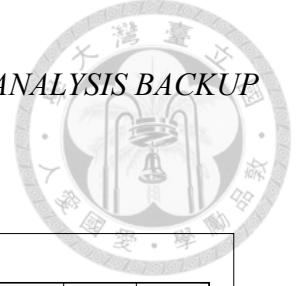


Figure D.3: Close look of Dalitz analysis result in data  $\Delta E - M_{bc}$  signal box of  $\eta(\pi^+\pi^-\pi^0)K^+\pi^-$ , first five plots show invariant mass of  $K^+\pi^-$  in  $M_{\eta\pi^-}$  slices, the bottom right one is the whole plot. Points with error bars are data, histograms are fit result, hatched histograms are background.

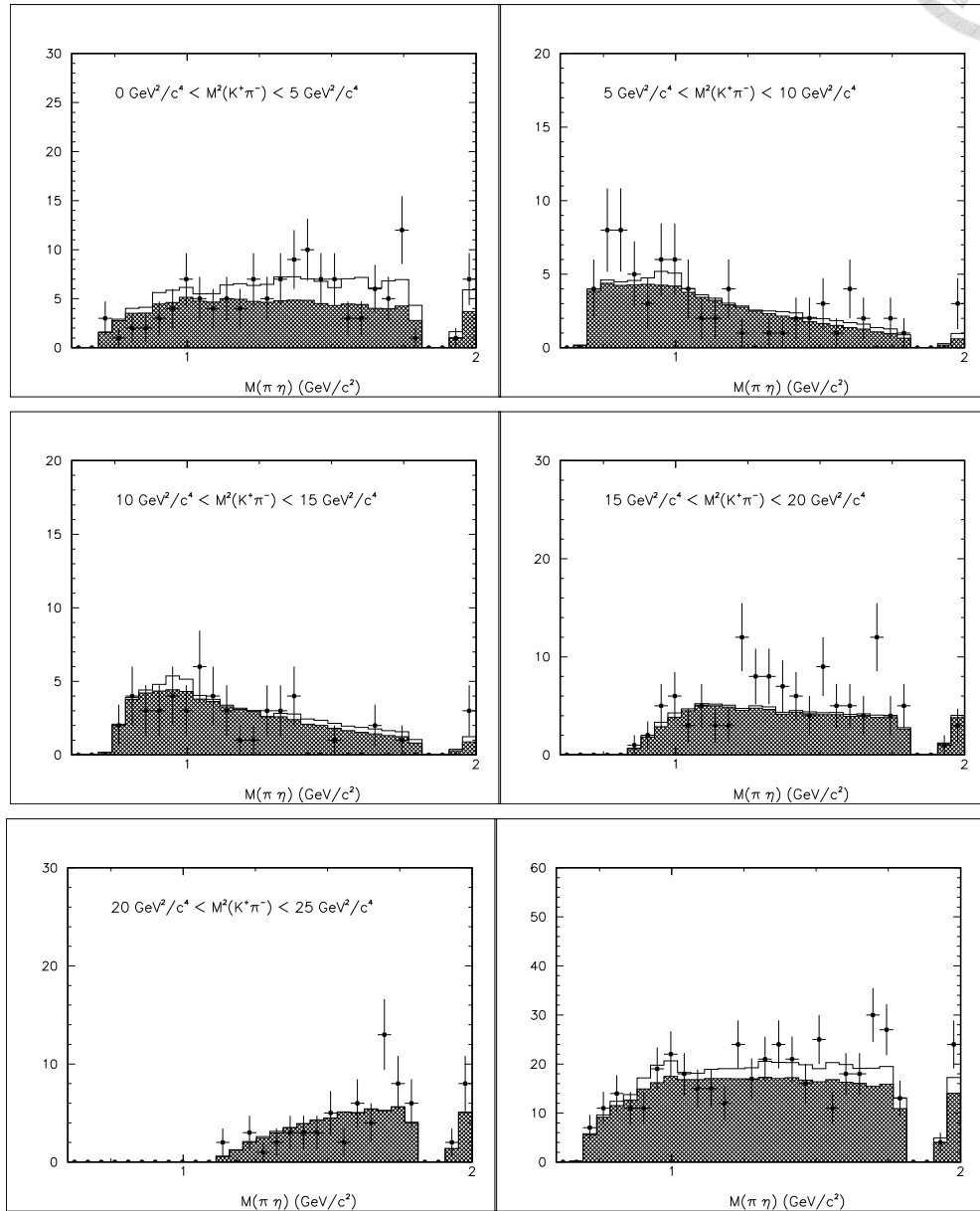


Figure D.4: Close look of Dalitz analysis result in data  $\Delta E - M_{bc}$  signal box of  $\eta(\pi^+\pi^-\pi^0)K^+\pi^-$ , first five plots show invariant mass of  $\eta\pi^-$  in  $M_{K^+\pi^-}$  slices, the bottom right one is the whole plot. Points with error bars are data, histograms are fit result, hatched histograms are background.







## Appendix E

### Results of Inclusive Decay

Table E.1: Signal yields( $N_s$ ), reconstruction efficiencies( $\varepsilon_{recon}$ ), branching fraction( $\mathcal{B}$ ) from 2D Maximum likelihood unbinned  $\Delta E - M_{bc}$  fits for inclusive decays.

Mode	$N_s$	$\varepsilon_{recon}(\%)$	$\mathcal{B}(10^{-6})$
$B^0 \rightarrow \eta(\gamma\gamma)K^+\pi^-$	$616.9^{+44.3}_{-43.6}$	12.04	$33.81^{+2.43}_{-2.39} \pm 2.20$
$B^0 \rightarrow \eta(\gamma\gamma)K^-\pi^+$	$562.9^{+43.3}_{-42.6}$	12.12	$30.64^{+2.36}_{-2.32} \pm 2.00$
			$\mathcal{A}_{CP} = -0.049^{+0.053}_{-0.052} \pm 0.046$
$B^0 \rightarrow \eta(\pi^+\pi^-\pi^0)K^+\pi^-$	$110.5^{+16.3}_{-15.5}$	4.54	$27.76^{+4.09}_{-3.89} \pm 1.49$
$B^0 \rightarrow \eta(\pi^+\pi^-\pi^0)K^-\pi^+$	$174.5^{+18.2}_{-17.5}$	4.58	$43.46^{+4.53}_{-4.36} \pm 2.34$
			$\mathcal{A}_{CP} = 0.220^{+0.088}_{-0.084} \pm 0.040$

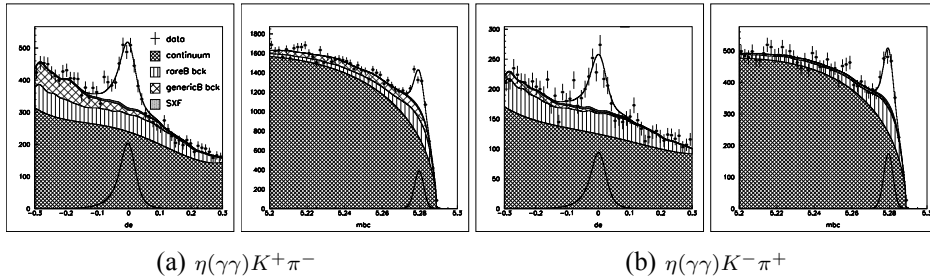


Figure E.1: The  $\Delta E$ (left) and  $M_{bc}$ (right) projection plot of data fitting for  $\eta(\gamma\gamma)K^+\pi^-$  and  $\eta(\gamma\gamma)K^-\pi^+$ , every component is the same as Fig.6.4.

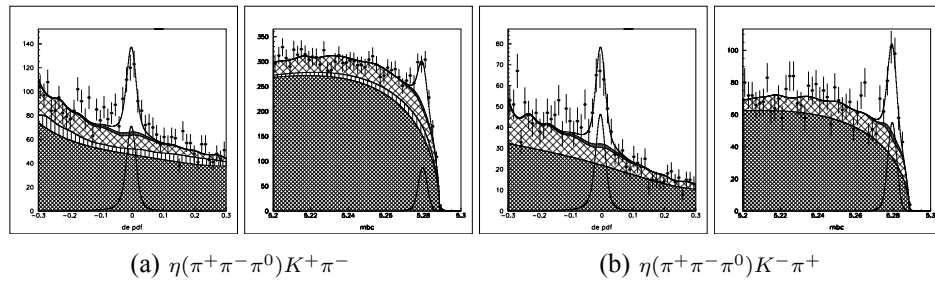
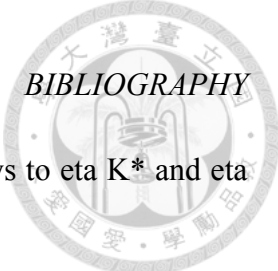


Figure E.2: The  $\Delta E$ (left) and  $M_{bc}$ (right) projection plot of data fitting for  $\eta(\pi^+\pi^-\pi^0)K^+\pi^-$  and  $\eta(\pi^+\pi^-\pi^0)K^-\pi^+$ , every component is the same as Fig. 6.4.



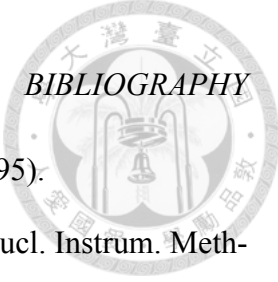
## Bibliography

- [1] "Standard Model of Elementary Particles" (Wikipedia), [http://en.wikipedia.org/wiki/File:Standard\\_Model\\_of\\_Elementary\\_Particles.svg/](http://en.wikipedia.org/wiki/File:Standard_Model_of_Elementary_Particles.svg/).
- [2] "Elementary Particle Interactions." (Wikipedia), [http://en.wikipedia.org/wiki/File:Elementary\\_particle\\_interactions.svg](http://en.wikipedia.org/wiki/File:Elementary_particle_interactions.svg).
- [3] "The Upsilon System", <http://www.lns.cornell.edu/public/lab-info/upsilon.html>.
- [4] "CP violation" (Wikipedia), [http://en.wikipedia.org/wiki/CP\\_violation](http://en.wikipedia.org/wiki/CP_violation).
- [5] A. Abashian *et al.*, "The Belle Detector", Nucl. Instrum Methods Phys. Res. Sect. A **479**, **1**, 117--232 (2002).
- [6] "Belle SVD 2 Upgrade Technical Design Report Version 3.1" (2001).
- [7] J. Beringer *et al.*, "Review of Particle Physics", Phys. Rev. D **86**, 010001 (2012).
- [8] S. Kurokawa and E. Kikutani, "Overview of the KEKB Accelerators", Nucl. Instrum. Methods Phys. Res. Sect A **499**, **1**, 1--7 (2003).
- [9] A. Garmash *et al.*, "Dalitz analysis of the three-body charmless decays  $B^+ \rightarrow K^+ \pi^+ \pi^-$  and  $B^+ \rightarrow K^+ K^+ K^-$ ", Phys. Rev. D **69**, 012001 (2004).
- [10] Bernard Aubert *et al.*, "Measurement of branching fractions and charge asymmetries in B decays to an eta meson and a  $K^*$  meson", Phys.Rev.Lett. **97**, 201802 (2006).

- 
- [11] C.H. Wang *et al.*, "Measurement of charmless B Decays to eta K\* and eta rho", Phys.Rev. D **75**, 092005 (2007).
- [12] B. Martin and G. Shaw, Particle Physics, Manchester Physics Series. Wiley (2008), ISBN 9780470721537.
- [13] "Standard Model" (Wikipedia), [http://en.wikipedia.org/wiki/Standard\\_Model](http://en.wikipedia.org/wiki/Standard_Model).
- [14] Nobel Prize Organization, <http://www.nobelprize.org/>.
- [15] R. L. Jaffe, , Phys. Rev. D **15**, 267, 281 (1997).
- [16] S. W. Herb *et al.*, "Observation of a Dimuon Resonance at 9.5 GeV in 400-GeV Proton-Nucleus Collisions", Phys. Rev. Lett. **39**, 252--255 (1977).
- [17] T. E. Browder and K. Honscheid, "B Mesons", Prog. Part. Nucl. Phys. **35**, **0**, 81--219 (1995).
- [18] N. Cabibbo, "Unitary Symmetry and Leptonic Decays", Phys. Rev. Lett. **10**, 531 (1963).
- [19] M. Kobayashi and T. Maskawa, "CP-Violation in the Renormalizable Theory of Weak Interaction", Prog. Theor. Phys. **49**, **2**, 652--657 (1973).
- [20] L. L. Chau and W. Y. Keung, "Comments on the Parametrization of the Kobayashi-Maskawa Matrix", Phys. Rev. Lett. **53**, 1802 (1984).
- [21] L. Wolfenstein, "Parametrization of the Kobayashi-Maskawa Matrix", Phys. Rev. Lett. **51**, 1945--1947 (1983).
- [22] V. L. Fitch J. H. Christenson, J. W. Cronin and R. Turlay, "Evidence for the  $2\pi$  Decay of the  $K_2^0$  Meson", Pisma Zh. Eksp. Teor. Fiz. **5**, 32--35 (1967).
- [23] A. B. Carter and A. I. Sanda., "CP Nonconservation in Cascade Decays of B Mesons", Phys. Rev. Lett. **45**, 952--954 (1980).
- [24] K. Abe *et al.*, "Observation of Large CP Violation in the Neutral B Meson System", Phys. Rev. Lett. **87**, 091802 (2001).

## BIBLIOGRAPHY

- [25] M. Kobayashi and T. Maskawa, "CP-violation in the Renormalizable Theory of Weak Interaction", *Progress of Theoretical Physics* **49, 2**, 652--657 (1973).
- [26] "KEKB B-Factory Design Report", **95-7** (1995).
- [27] "Belle Progress Report" (March, 1997).
- [28] K. Ueno *et al.*, "Proceedings of the Calorimetry Conference" (1999).
- [29] M. Z. Wang *et al.*, "Review of EFC options", Belle Note 164 (1996).
- [30] K. Ueno *et al.*, "Detection of minimum-ionizing particles and nuclear counter effect with pure BGO and BSO crystals with photodiode readout", *Nucl. Instr. and Meth.* **A396**, 103 (1997).
- [31] M. Z. Wang *et al.*, "Beam test of the BELLE extreme forward calorimeter at KEK", *Nucl. Instr. and Meth.* **A455**, 319 (2000).
- [32] Y. Ushiroda *et al.*, "Belle silicon vertex detectors", *Nucl. Instr. and Meth.* **A511**, 6--10 (2003).
- [33] Z. Natkaniec *et al.*, "Belle SVD2 Vertex Detector", *Nucl. Instrum. Methods Phys. Res. Sect.* **A568**, 269--273 (2006).
- [34] S. Uno, "The BELLE central drift chamber", *Nucl. Instr. and Meth.* **A379**, 421--423 (1996).
- [35] H. Hirano *et al.*, "A high-resolution cylindrical drift chamber for the KEK B-factory", *Nucl. Instr. and Meth.* **A455**, 294--304 (2000).
- [36] S. Uno *et al.*, "Study of a drift chamber filled with a helium-ethane mixture", *Nucl. Instr. and Meth.* **A330**, 55--63 (1993).
- [37] O. Nitoh *et al.*, "Drift Velocity of Electrons in Helium-Based Gas Mixtures Measured with a UV Laser", *Jan. J. Appl. Phys.* **33**, 5929 (1994).
- [38] I. Adachi *et al.*, "Study of a threshold Cherenkov counter based on silica aerogels with low refractive indices", *Nucl. Instr. and Meth.* **A355**, 390--398 (1995).

- 
- [39] "Belle Technical Design Report", KEK Report **95-1** (1995).
- [40] K. Hanagaki *et al.*, "Electron Identification in Belle", Nucl. Instrum. Methods Phys. Res. Sect. **A485, 3**, 490--503 (2002).
- [41] S.J. Richichi *et al.*, "Two-body B meson decays to eta and eta-prime: Observation of B to eta K\*", Phys.Rev.Lett. **85**, 520--524 (2000).
- [42] M. Wirbel *et al.*, "Exclusive Semileptonic Decays of Heavy Mesons, Zeit. Phys. **C29**, 637 (1985).
- [43] Particle Data Group, <http://pdglive.lbl.gov/>.
- [44] A.Wuethrich, "Dalitz Plots and Hadron Spectroscopy", hep-ph/0207058v1 page 28 (2005).
- [45] B. Bhuyan, "High  $P_T$  Tracking Efficiency Using Partially Reconstructed  $D^*$  Decays (Belle internal)", Belle Note **1165** (2010).
- [46] "Number of  $B$  in HadronB(J)" (Belle internal), <http://belle.kek.jp/secured/nbb/nbb.html>.